TOWARDS TUNABLE AND MULTIFUNCTIONAL INTERFACES:

MULTICOMPONENT AMORPHOUS ALLOYS

AND BILAYER STACKS

by

MATTHEW G. KAST

A DISSERTATION

Presented to the Department of Chemistry and Biochemistry
and the Graduate School of the University of Oregon
in partial fulfillment of the requirements
for the degree of
Doctor of Philosophy

December 2016

DISSERTATION APPROVAL PAGE

Student: Matthew G. Kast

Title: Towards Tunable and Multifunctional Interfaces: Multicomponent Amorphous Alloys and Bilayer Stacks

This dissertation has been accepted and approved in partial fulfillment of the requirements for the Doctor of Philosophy degree in the Department of Chemistry and Biochemistry by:

Dr. George V. Nazin	Chairperson
Dr. Shannon W. Boettcher	Advisor
Dr. Mark C. Lonergan	Core Member
Dr. Richard P. Taylor	Institutional Representative

and

Scott L. Pratt	Dean of the Graduate School

Original approval signatures are on file with the University of Oregon Graduate School.

Degree awarded December 2016

DISSERTATION ABSTRACT

Matthew G. Kast

Doctor of Philosophy

Department of Chemistry and Biochemistry

December 2016

Title: Towards Tunable and Multifunctional Interfaces: Multicomponent Amorphous Alloys and Bilayer Stacks

Controlling the electronic structure and requisite charge transfer at and across interfaces is a grand challenge of materials science. Despite decades of research and numerous successes in the fields microelectronics and photovoltaics much work remains to be done. In many applications, whether they be in microelectronics, photovoltaics or display technology there is a demand for multiple functions at a single interface. Historically, existent materials were either discarded as an option due to known properties or tested with some application based figure of merit in mind. Following this, the quality of the material and/or the preparation of the surface/interface to which the material would be deposited was optimized. As the microelectronics and photovoltaics industries have matured, continued progress (faster, lower power transistors and more efficient, cheaper, abundant solar cells) will require new materials (possibly not previously existent) that are fundamentally better for their application than their highly optimized existent counter parts. The manifestation of this has been seen in the microelectronics field with introduction of hafnium silicates to replace silica (which had previously been monumentally successful) as the gate dielectrics for the most advanced transistors. Continued progress in efficient, cheap, abundant photovoltaics will require

similar advances. Advances will be needed in the area of new abundant absorbers that can be deposited cheaply which result in materials with high efficiencies. In addition, selective contacts capable of extracting charge from efficient absorbers with low ohmic losses and low recombination rates will be needed. Presented here are two approaches to the multifunctional interface problem, first the use of amorphous alloys that open up the accessible composition space of thin films significantly and second the use of bilayers that loosen the requirements of a single film at an interface.

This dissertation includes previously published and unpublished coauthored material.

CURRICULUM VITAE

NAME OF AUTHOR: Matthew G. Kast

GRADUATE AND UNDERGRADUATE SCHOOLS ATTENDED:

University of Oregon, Eugene
Arizona State University, Tempe

DEGREES AWARDED:

Doctor of Philosophy, Chemistry, 2016, University of Oregon
Master of Science, Chemistry, 2011, University of Oregon
Bachelor of Science, Chemistry, 2010, Arizona State University

AREAS OF SPECIAL INTEREST:

Materials Chemistry

PROFESSIONAL EXPERIENCE:

Research Assistant, Boettcher Research Group, University of Oregon, 2012-2016

Process Engineer Intern, Intel, Dec 2010 to Sept 2011

Cellar Production Chemist and Tasting Room Host, Middle Mountain Mead, May 2006 to Aug 2009 (summers only)

GRANTS, AWARDS, AND HONORS:

Merck Index Award, Arizona State University, 2010

ACS Analytical Chemistry Award, Arizona State University, 2009

Bateman Scholarship, Arizona State University, 2007

Presidents Scholarship, Arizona State University, 2006-2010

PUBLICATIONS:

Woods, K.N.; Chiang, T-H; Plassmeyer, P.N.; Kast, M.G.; Lygo, A.C.; Grealish, A.K.; Boettcher, S.W.; Page, C.J. (submitted to Chemistry of Materials)

Kast, M.G.; Cochran, E.A.; Enman, L.J.; Mitchson, G.; Ditto, J.; Siefe, C.; Plassmeyer, P.N. Greenaway, A.L.; Johnson, D.C.; Page, C.J.; Boettcher, S.W. *J. Am. Chem. Soc.* (in revision)

Murari, N. M.; Mansergh, R. H.; Huang, Y.; Kast, M. G.; Keszler, D. A.; Conley, J. F. *J. Mater. Res.* **2016**, 1–10.

Greenaway, A. L.; Sharps, M. C.; Boucher, J. W.; Strange, L. E.; Kast, M. G.; Torrigino, B. B.; Aloni, S.; Boettcher, S. W. *Prep.* **2016**, *1*, 402–408.

Zou, S.; Burke, M. S.; Kast, M. G.; Fan, J.; Danilovic, N.; Boettcher, S. W. *Chem. Mater.* **2015**, *27* (23), 8011–8020.

Nadarajah, A.; Wu, M. Z. B.; Archila, K.; Kast, M. G.; Smith, A. M.; Chiang, T. H.; Keszler, D. a.; Wager, J. F.; Boettcher, S. W. *Chem. Mater.* **2015**, *27* (16), 5587–5596.

Burke, M. S.; Kast, M. G.; Trotochaud, L.; Smith, A. M.; Boettcher, S. W. *J. Am. Chem. Soc.* **2015**, 150220163913001.

Kast, M. G.; Enman, L. J.; Gurnon, N. J.; Nadarajah, A.; Boettcher, S. W. *ACS Appl. Mater. Interfaces* **2014**, *6* (24), 22830–22837.

Smith, A. M.; Kast, M. G.; Nail, B. a.; Aloni, S.; Boettcher, S. W. *J. Mater. Chem. A* **2014**, *2* (17), 6121.

Nadarajah, A.; Carnes, M. E.; Kast, M. G.; Johnson, D. W.; Boettcher, S. W. *Chem. Mater.* **2013**, *25* (20), 4080–4087

ACKNOWLEDGMENTS

I thank the previous members of the lab for their patience and mentoring, the current members for their support and those I had the honor to mentor for their *patience* with me and enthusiasm for science. In particular, I thank: Dr. Lena Trotochaud, Dr. Adam Smith, Dr. Fuding Lin, Dr. T.J. Mills, Nick Gurnon, Dr. Andy Ritenour, Dr. Athavan Nadarajah, Dr. Sangeun Chun, Major Dr. Adam Batchellor, Dr. Jason Boucher, Michaela Stevens, Annie Greenaway, Lisa Enman, Lizzie Cochran, Forrest Laskowski, Mike Nellist, Chris Funch, Dr. Jingjing Qiu, Brittany Gordon, Julija Vinckeviciute, Chris Siefe and Erica Pledger. Additionally, I would like to thank Dr. Paul Plassmeyer for his friendship, mentorship, inspiration, fundamental and experimental insight.

I would like to thank my co-authors, especially: Lisa Enman, Lizzie Cochran, Blake Hammann, Athavan Nadarajah, Adam Smith, Michaela Stevens, Shihui Zou, Annie Greenaway, Nishit Murai and Keenan Woods among many others.

I would like to thank my boss Prof. Shannon Boettcher for giving me the opportunity to do research, accepting me from the masters program, his insight and perspective. I thank my doctoral committee Prof. George Nazin, Prof. Mark Lonergan and Prof. Richard Taylor for their insight, perspective, energy, demeanor, many thoughtful questions and the time I've taken from their already busy schedules.

Lastly, I would like to thank my sister Emma Kast and parents John Kast and Terry Peterman as well as my partner Andrea Loes for their constant support during the last 5 years.

In memory of
T.J. Mills
your laugh, your thoughtfulness and your music are missed

TABLE OF CONTENTS

Chapter Page

LIST OF FIGURES

Figure Page

Figure Page

Figure Page

LIST OF TABLES

Table Page

CHAPTER I

TOWARDS MULTIFUNCTIONAL INTERFACES: MULTICOMPONENT AMORPHOUS ALLOYS AND BILAYER STACKS

Portions of this chapter were previously submitted to publish as Kast, M.G.; Cochran, E.A.; Enman, L.J.; Mitchson, G.; Ditto, J.; Siefe, C.; Plassmeyer, P.N. Greenaway, A.L.; Johnson, D.C.; Page, C.J.; Boettcher, S.W. Amorphous Mixed-Metal Oxide Thin Films from Aqueous Solution Precursors with Near Atomic Smoothness. The excerpt to be included was written entirely by me. D. C. Johnson, C. J. Page and S. W. Boettcher provided editorial assistance. E. A. Cochran, L. J. Enman, G. Mitchson, J. Ditto, C. Siefe and P. N. Plassmeyer provided experimental assistance.

Portions of this chapter were previously published as Kast, M. G.; Enman, L. J.; Gurnon, N. J.; Nadarajah, A.; Boettcher, S. W. Solution-Deposited F:SnO_2/TiO_2 as a Base-Stable Protective Layer and Antireflective Coating for Microtextured Buried-Junction H_2-evolving Si Photocathodes. *ACS Applied Materials and Interfaces* 2014, 6, 22830-22837. The experimental work was performed either by me or by L. J. Enman, N. J. Gurnon and A. Nadarajah under my and S. W. Boettcher's direction. S. W. Boettcher provided editorial assistance.

Multifunctional Tunable Materials for Fundamental Studies

Tunable materials with properties that rival those of naturally occuring simple or binary compounds are becoming increasingly important for fundamental studies and a range of applications. High tunability of a material makes it inherently useful for fundamental studies as it can enable avenues of research including composition and property space which can not be accessed when only existing materials are utalized. As materials for applications become increasingly optimized increasing tunability and material-family knowledge is required to support rapid development of existing and future applications. In recent history, materials in the thin film form have become increasingly important due to their usage in microelectronic (MOSFETs, memory), macro-opto-electronic (PV, display), optoelectronic (LED, Laser) and a host of coating applications (corrision resistant, scratch resistant, self cleaning…). In addition to their applications, the way in which thin films are made are often very different than their bulk counterparts. These depostion methods often incorporate high energy chemical or physical reactions which in turn enable compositional and/or structual motifs which may not be accessible in bulk materials.

Investigated here are three families (depicted in Figure 1.1) of materials in thin film moprhology which allow for a high degree of tunability. The first, is a physical mixture of transition metal oxide particulates and amorphous alumina. The second, is an amorphous solid solution of two components, which may manifest properties different from the two components. Third, thin bilayers of two components can be utalized when an interface or film need to have two properties that are difficult to integrate into a single composite material.

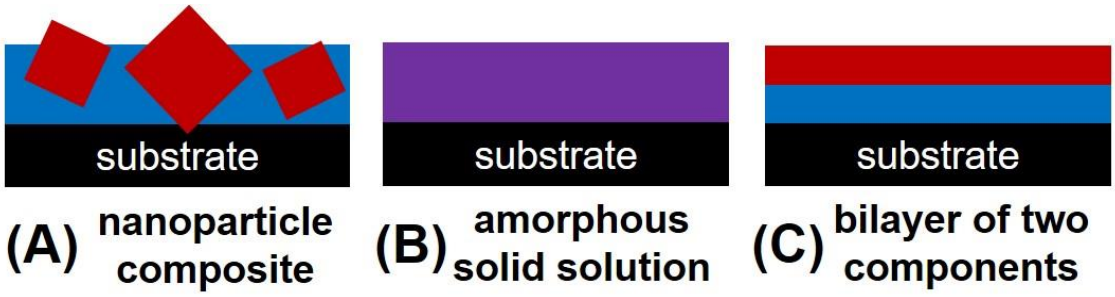

Figure 1.1. Pictorial representations of (A) a nanoparticle composite, (B) an amorphous solid solution and (C) a bilayer of two components.

Amorphous Alumina, Versatile, Intriguing and Solution Processable

Chapter II will discuss the long range order, local structure, chemistry, morphology and dielectric constant of Al_2O_3 thin films deposited from aqueous solution as a function of annealing temperature from 200 to 1100 °C. A precondensed highly soluble molecular $Al(OH)_x(NO_3)_{3-x}$ cluster is used to facilitate film formation. Long range order in the form of γ-Al_2O_3 and α-Al_2O_3 (the thermodynamically stable phase) does not appear in GIXRD scans until annealing temperatures of 950 and 1100 °C respectively. The crystallization of the films at these temperatures is consistent with literature, FTIR data and ^{27}Al-ssNMR data. FTIR is used to track the progress of the decomposition reaction of $Al(OH)_x(NO_3)_{3-x}$ to Al_2O_3, via the O-H and N-O vibrational modes. In conjunction with FTIR and GIXRD the local structure of Al is tracked with ssNMR.

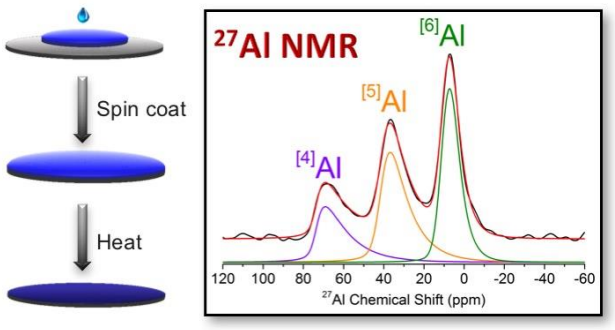

Figure 1.2. Pictorial repersentation of spin processing of Al_2O_3 and example ^{27}Al ssNMR data showing the local coordination environments of Al after annealing at 200 °C.

This combined data allows for a few mechanisms of the change in Al coordination at low temperature to be evaluated. The ssNMR data allows for the direct comparison of the *amorphous* structure of solution deposited Al_2O_3 with a-Al_2O_3 films deposited by sputtering, PEALD and MOCVD. Intriguingly, despite vary different deposition routes and processes the structure of amorphous films, deposited by different labs via different methods is near identical implying the presence of a deep local minimum in energy at the structure that has been seen. Furthermore, differences in bulk diffusion and surface diffusion appear to manifest in the crystallization temperatures observed in the different deposition processes. The solution processability and amorphous nature of Al_2O_3 over a long range of annealing temperatures makes it very suitable as an inert, insulating, passivating glass forming component in nanoparticulate composite and amorphous solid solution multicomponent films as will be discussed in chapters III and IV.

Portions of this work was coauthored. Co-authored material (with B. A. Hammann, P. N. Plassmeyer, Z. L. Ma, K. N. Woods, D. A. Keszler, C. J. Page, S. W. Boettcher and S. E. Hayes). The excerpt to be included was written by B. A. Hammann and myself. D. A. Keszler, C. J. Page, S. W. Boettcher and S. E. Hayes provided editorial assistance. B. A. Hamman, P. N. Plassmeyer, Z. L. Ma, and K. N. Woods provided experimental assistance

Transition Metal Oxide Alloys

In chapter III we report the synthesis and characterization of a new class of compositionally homogenous thin films that are amorphous solid solutions of Al_2O_3 and

transition metal oxides (TMO_x) including VO_x, CrO_x, MnO_x, Fe_2O_3, CoO_x, NiO, CuO_x and ZnO. The synthesis is enabled by the rapid decomposition of molecular transition-metal nitrates $TM(NO_3)_x$ at low temperature along with pre-condensed oligomeric $Al(OH)_x(NO_3)_{3-x}$ cluster species; both of which can be processed from aq. solution. The films are dense, ultra-smooth (R_{rms} < 1 nm, near 0.1 nm in many cases), and are atomically mixed amorphous metal oxide alloys over a large composition range.

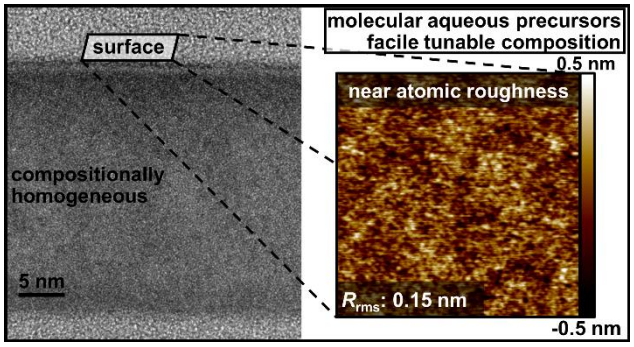

Figure 1.3. TEM and AFM of the amorphous solid solution $Fe_{0.5}Al_{0.5}O_x$ exhibiting compositional homogeneity and near atomic roughness.

We assess the chemical principles that favor the formation of amorphous homogenous films over rougher phase-segregated nanocrystalline films. The synthesis is easily extended to other compositions of transition and main-group metal oxides. To demonstrate versatility, we synthesized amorphous $V_{0.1}Cr_{0.1}Mn_{0.1}Fe_{0.1}Zn_{0.1}Al_{0.5}O_x$ and $V_{0.2}Cr_{0.2}Fe_{0.2}Al_{0.4}O_x$ with R_{rms} ~0.1 nm and uniform composition. The combination of ideal physical properties (dense, smooth, uniform) and broad composition tunability provides a platform for film synthesis that can be used to study fundamental phenomena when the effects of transition metal cation identity, solid-state concentration of d-electrons or d-states and/or crystallinity need to be controlled. The new platform has broad potential use in controlling interfacial phenomena such as electron transfer in solar-cell contacts or surface reactivity in heterogeneous catalysis.

Portions of this work were previously submitted to publish as Kast, M.G.; Cochran, E.A.; Enman, L.J.; Mitchson, G.; Ditto, J.; Siefe, C.; Plassmeyer, P.N. Greenaway, A.L.; Johnson, D.C.; Page, C.J.; Boettcher, S.W. Amorphous Mixed-Metal Oxide Thin Films from Aqueous Solution Precursors with Near Atomic Smoothness. The excerpt to be included was written entirely by me. D. C. Johnson, C. J. Page and S. W. Boettcher provided editorial assistance. E. A. Cochran, L. J. Enman, G. Mitchson, J. Ditto, C. Siefe and P. N. Plassmeyer provided experimental assistance.

The Local Structure of Transition Metal Cations in an Amorphous Alumina Matrix

In chapter IV the local structure of transition metal cations (V^{5+}, $Cr^{3+/6+}$, Fe^{3+}, $Co^{2+/3+}$, Ni^{2+}, Cu^{2+} and Zn^{2+}) in an Al_2O_3 matrix have been investigated by XAS and optical absorbance. Accurate bond lengths, approximate coordination numbers and the presence of inversion centers can be probed by XAS while optical spectroscopy is sensitive to the local bond arrangement (i.e. is a 4 coordinate species tetrahedral or square planar) and can be used to extract band to band transition energies. Metal cations with coordination numbers higher than four in the crystalline oxide state (V, Cr, Fe, Co and Ni) all showed decreases in coordination number when in the a-Al_2O_3 matrix. Metal cations with coordination numbers of four in the crystalline oxide state (Cu and Zn) show no significant change in coordination number. In all cases significant differences in optical absorbance are seen between the crystalline metal oxides and the metal cations in the a-Al_2O_3 matrix. This is generally indicative that the electronic structure of the a-$TM_yAl_{1-y}O_x$ films is not a linear combination of a-Al_2O_3 and c-TMO_x.

Portions of this work include coauthored material. Co-authored material (with L. J. Enman, E. A. Cochran, E. Pledger and S. W. Boettcher). The excerpt to be included

was written entirely by myself and Lisa Enman. The experimental work was performed either by me or by L. J. Enman, E. A. Cochran and E. Pledger under my, L. J. Enman's and S. W. Boettcher's direction. Myself, L. J. Enman and E. A. Cochran made samples for and collected XAS data. L. J. Enman analyzed all XAS data. E. Pledger made samples for, collected and worked up all optical absorbance data under my direction. I analyzed all optical absorbance data.

Multifunctional Metal Oxide Bilayers

Protecting Si photocathodes from corrosion is important for developing tandem water-splitting devices operating in basic media. In chapter V we show that textured commercial Si-pn^+ photovoltaics protected by solution-processed bilayers consisting of a semiconducting/conducting oxides (plausibly suitable for scalable manufacturing) and coupled to thin layers of Ir yield high-performance H_2-evolving photocathodes in base. They also serve as excellent test structures to understand corrosion mechanisms and optimize interfacial electrical contacts between various functional layers. Solution-deposited TiO_2 protects Si-pn^+ junctions from corrosion for ~24 h in base, whereas junctions protected by F:SnO_2 fail after only 1 h of electrochemical cycling. Interface layers consisting of Ti metal and/or the highly doped F:SnO_2 between the Si and TiO_2 reduce Si-emitter/oxide/catalyst contact resistance and thus increase fill factor and efficiency. Controlling the oxide thickness led to record photocurrents near 35 mA cm^{-2} at 0 V vs. RHE and photocathode efficiencies up to 10.9% in the best cells. Degradation, however, was not completely suppressed. We demonstrate that performance degrades by two mechanisms, (1) deposition of impurities onto the thin catalyst layers, even from high-purity base, and (2) catastrophic failure via pinholes in the oxide layers after several

days of operation. The effect on performance and the physical damage are presented in Figure 1.4. These results provide insight into the design of hydrogen-evolving photoelectrodes in basic conditions, and highlight challenges.

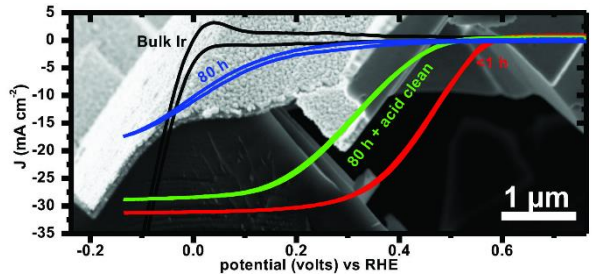

Figure 1.4. SEM of Si etched out (presumably through a pin hole) from underneath a Ir/TiO_2/F:SnO_2/Ti protective layer and catalyst stack. Voltammograms show the degredation in performance due to catalyst poisoning and etch damage.

Portions of this work were previously published as Kast, M. G.; Enman, L. J.; Gurnon, N. J.; Nadarajah, A.; Boettcher, S. W. Solution-Deposited F:SnO_2/TiO_2 as a Base-Stable Protective Layer and Antireflective Coating for Microtextured Buried-Junction H_2-evolving Si Photocathodes. *ACS Applied Materials and Interfaces* 2014, 6, 22830-22837. The experimental work was performed either by me or by L. J. Enman, N. J. Gurnon and A. Nadarajah under my and S. W. Boettcher's direction. S. W. Boettcher provided editorial assistance.

CHAPTER II

AQUEOUS PROCESSED ALUMINUM OXIDE THIN FILMS: INSIGHTS INTO LOCAL STRUCTURE AND DIELECTRIC RESPONSE

Portions of this chapter was coauthored. Co-authored material (with B. A. Hammann, P. N. Plassmeyer, Z. L. Ma, K. N. Woods, D. A. Keszler, C. J. Page, S. W. Boettcher and S. E. Hayes). The excerpt to be included was written by B. A. Hammann and myself. D. A. Keszler, C. J. Page, S. W. Boettcher and S. E. Hayes provided editorial assistance. B. A. Hamman, P. N. Plassmeyer, Z. L. Ma, and K. N. Woods provided experimental assistance.

Introduction

Amorphous Al_2O_3's unique properties result in its use in a myriad of devices and applications in many different forms. Thin films of Al_2O_3 are intriguing due to the host of modern applications high quality thin films. Its large phase dependent band gap (7 eV),[1] related low leakage current (<2 MV/cm),[2,3] moderate dielectric constant (11)[2,3] and decent channel mobility response (8 $cm^2V^{-1}s^{-1}$)[4–7] allow for it to be used as a dielectric layer in thin film transistors (TFTs). Its transparency[1] and ability to trap negative charge at the Al_2O_3-to-native SiO_2 interface allows passivation of p-Si emitters in crystalline silicon solar cells.[8,9] It's transparency and hardness (7.8 GPa)[10,11] make it excellent for abrasion resistant coatings on screens and optics.

SiO_2 readily forms a glassy amorphous solid when cooled from a melt unlike Al_2O_3 which does not[12,13]. This is likely due to Al_2O_3's lower melting-point-viscosity

than SiO_2 which gives liquid Al_2O_3 time to reorganize into a crystalline state before total solidification occurs. We note that viscosity is a macroscopic manifestation of a higher ion mobility which is in turn possibly due to the decreased formal charge on Al (+3) in an oxide network relative to Si (+4)[14,15].

Despite the fact that amorphous Al_2O_3 cannot be readily synthesized from the cooling of bulk melts,[12,13] it can be easily formed by many forms of chemical or physical thin film deposition including solution deposition, sputtering, atomic layer deposition or chemical vapor deposition.[11,13,16,17] As previously mentioned in the literature, this is likely due to the occurrence of a rapid chemical "quench" from a monomer or few-atom cluster precursor in the solution or gas phase to a fully networked amorphous phase.[13] These process appear to entirely bypass the molten Al_2O_3 phase from which crystalline Al_2O_3 forms.

The tendency of Al_2O_3 to form amorphous structures immediately rules out traditional diffraction techniques for the study of its structure. Aluminum's relatively low X-ray absorption edge make synchrotron based XAS measurements experimentally non-trivial, coupled with the overlap of 4-, 5- and 6- coordinate Al "fingerprints"[18] (hereafter, denoted $^{[n]}$Al). Furthermore, current XAS modeling approaches would only give an average coordination number in contrast to quantified ratios of coordination environments. Fourier transform infrared spectroscopy (FTIR) can be used to discern $^{[4]}$Al-O and $^{[6]}$Al-O vibrational modes in some crystalline oxides and solutions, but with $^{[4]}$Al, $^{[5]}$Al, and $^{[6]}$Al species present with a high degree of disorder in metal oxygen bond distances and bond angles quantifying ratios of $^{[4]}$Al:$^{[5]}$Al:$^{[6]}$Al does not appear feasible. Thus, as shown by a few groups Lee et al.[19] and Sarou-Kanian et al.[11] ^{27}Al solid-state

nuclear magnetic resonance (^{27}Al-ssNMR) is used to probe the local structure of the amorphous alumina thin films.

We report the first speciation of Al as a function of annealing temperature determined by ^{27}Al ssNMR in an amorphous Al_2O_3 thin film deposited from aqueous solutions. Here we track the formation of amorphous Al_2O_3 from molecular pre-condensed aqueous $Al(NO_3)_{3-x}(OH)_x$ species and its eventual conversion to crystalline γ- and α- Al_2O_3. By tracking the concentration of nitrates and hydroxide counter ions in the films, the formation of the amorphous oxide network is correlated to the removal of non-oxide ligands. X-ray diffraction is used to verify the presence of crystalline species upon a rapid change in Al coordination distribution at high temperature (>800 °C). In addition, we track the dielectric constant of the deposited films as a function of annealing temperature which is affected by both the decomposition of polarizable and ionic ligands and the crystallization of Al_2O_3. The distribution of aluminum environments that are seen when the films are amorphous are similar to those found when amorphous Al_2O_3 films are deposited by other methods including metal-organic chemical vapor deposition (MOCVD),[11] atomic layer deposition (ALD),[19] and physical vapor deposition (PVD),[19] extending the hypothesis that the structure of amorphous Al_2O_3 may sit at a local minimum in the energy landscape which is accessible by multiple thin film deposition techniques.[13] The methods, and conclusions drawn from the resulting data analysis, are thus likely broadly applicable to the study of solution processed amorphous thin films.

Methods

Preparation of Films

Al_2O_3 thin films were prepared by aqueous spin-coating onto silicon substrates. Water-soluble "Al_{13}" (nominally $Al_{13}(OH)_{24}(H_2O)_{24}(NO_3)$) molecular precursors were prepared via literature procedure.[20] In summary, nitrates were pulled out of a solution of $Al(NO_3)_3$ (Alfa Aesar, 98.0-102.0 %) into a fritted counter electrode compartment by passing 60 kC of reductive charge per mole $Al(NO_3)_3$. The reducing current is due to the hydrogen evolutions reaction (HER), nitrates cross the frit into the counter electrode (at which oxygen evolution occurs, OER) compartment to maintain charge balance. The final precursor consists of 1M $Al(OH)_x(NO_3)_{3-x}$ in H_2O with a pH of 3. Silicon substrates were cleaned in 1 M nitric acid (EMD, ACS grade) to remove any trace adventitious Al containing species), rinsed with 18.2 M nanopure water, and treated in an O_2/N_2 plasma using a PE-50 Bench Plasma Cleaner (Plasma Etch, Inc.) set to maximum power. This surface treatment creates a hydrophilic surface, which is essential for good coverage of the deposited precursor solution. Individual coats were deposited using 1 M (relative to Al^{3+}) Al_{13} solutions filtered through 0.2 μm PTFE syringe filters, spin-processed at 3000 RPM for 30 sec. Films were promptly transferred to a hot plate set to 200 °C (in the case of the 200 °C sample) or 300 °C (for all other samples) and annealed for 15 minutes between coats. This process was repeated 10 times to generate thicker films. A final 1 h anneal was performed at temperatures of 200, 300, 400, 500, 600, 700, 800, 950, and 1100 °C, using a hot plate or a box furnace in ambient atmosphere.

Film Characterization

Films fabricated for X-ray diffraction (XRD) and Fourier Transform Infrared spectroscopy (FTIR) analysis were deposited onto high-resistivity IR-transparent double-sided-polished (100)-cut silicon wafers. X-ray diffraction (XRD) data was collected in grazing incidence XRD (GIXRD) geometry on a Rigaku SmartLab Diffractometer. The Cu source was held at 0.5° above the plane of the sample, and a 0D scintillation detector was swept from 10° to 70° in 0.1° steps with a 12 s integration time per step. A single ten-coat film was annealed at 200 °C (as described above) and measured by GIXRD. The same film was then annealed to higher temperatures increasing by 100 °C or 150 °C increments up to 1100°C with GIXRD measurements at room temperature between each annealing step. FTIR analyses were performed on the same film after annealing at each temperature using a Nicolet 6700 Fourier transform infrared (FTIR) spectrometer. Background corrections were made using a bare silicon substrate subjected to the same heat treatments.

Liquid-state NMR

The liquid-state ^{27}Al NMR spectrum was acquired on a 11.8 T magnet with a ^{27}Al Larmor frequency of 130.25 MHz using a Varian Unity Inova-500 MHz spectrometer. The water-soluble molecular precursor solution was placed into a 5 mm NMR tube, and the ^{27}Al spectrum was acquired using a Bloch decay pulse sequence with a recycle delay of 5 s. The spectrum was referenced to a 1.0 M solution of $Al(NO_3)_3$.

Solid-state NMR

A series of Al_2O_3 films were prepared for solid-state NMR (ssNMR) analysis on 100 μm thick double-side-polished silicon wafers, as described previously. The Al_2O_3 films (and silicon substrates) were crushed into a coarse powder using a mortar and pestle and packed into an NMR rotor. Solid-state ^{27}Al NMR spectra were acquired at 19.96 T corresponding to ^{27}Al Larmor frequencies of 221.41 MHz and were performed on a 3.2 mm HXFY MAS probe. A rotor-synchronized quadrupolar-echo[21,22] pulse sequence ($\pi/2$ - t - π) was used under magic-angle spinning (MAS). All magic angle spinning (MAS) spectra were collected with a spinning frequency (ν_R) of 22.5 kHz. A central transition selective $\pi/2$ pulse length of 2.25 μs was used at 19.96 T. The recycle delay was 1 s at 19.96 T, and 5400 transients were collected for each spectrum. The ^{27}Al background (from rotor and probe) was collected using identical experimental parameters on an empty rotor. The background signal was subtracted from the total film signal in the time domain before Fourier transforming. All spectra were referenced to a 1.0 M solution of $Al(NO_3)_3$, and the NMR spectra were simulated using Dmfit.[23]

The $^{[4]}$Al and $^{[5]}$Al resonances were simulated using the "Czjzek" model[24–26] which accounts for the local structure of the Al sites arising from a statistical disorder of Al environments as observed in Al_2O_3 glasses and thin films.[11] The following parameters were allowed to fit within Dmfit in order to simulate the ^{27}Al NMR lineshape: δ_{ISO}, CQ, amplitude, position, and width (for the Gaussian lineshape). A value for "d" equal to 5 was used for the Czjzek model as any value outside of that is not physical in our system.[27] Note: During fitting of the lineshape measured at 1100 °C, the peak

representing $^{[5]}$Al always converged to zero hence the concentration of the $^{[5]}$Al was found to be zero as seen in Figures 2 and 3.

SEM and Ellipsometry

Al_2O_3 films were prepared for SEM analysis by thermally evaporating ~30 nm of Al onto the film surface. This step is necessary to prevent the accumulation of static electric charges ("charging") during SEM imaging.[9] Samples were then physically cleaved, and the corresponding cross-sections were imaged using a FEI Helios Dual Beam FIB. Al_2O_3 samples annealed > 800 °C were imaged using a 3.0 kV accelerating voltage, while Al_2O_3 samples annealed < 700 °C required a lower accelerating voltage of 2.0 kV to prevent beam damage to the films.

Film thicknesses were measured using a J. A. Woollam Co., Inc. EC-270 spectroscopic ellipsometer equipped with a LPS-400 75 W xenon light source and a M44 detector. In order to extract thickness values from raw ellipsometry data, a model using a single Cauchy layer plus a 1 mm Si substrate was used. Initial best fits of the Cauchy layer were repeatedly perturbed and allowed to achieve new best fits, in order to assure that the models did not settle on a local minimum.

Results and Discussion

Long Range Structure

GIXRD patterns of aluminum oxide films annealed in the temperature range of 200 - 1100 °C are shown in Figure 2.1. No Bragg diffraction is observed for the films annealed from 200 to 800 °C, indicating that the films are amorphous. Films annealed at higher temperatures show Bragg diffraction peaks attributable to γ-Al_2O_3 at 950 °C, , and

to a mixture of α-Al_2O_3[28] and γ-Al_2O_3[29] at 1100 °C. The conversion of γ-Al_2O_3 (and other low temperature Al_2O_3) to α-Al_2O_3 from 950 at 1100 °C has been observed previously.[29,30]

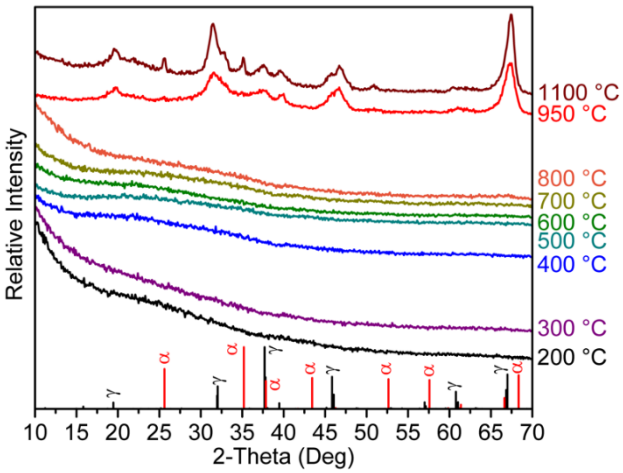

Figure 2.2. Grazing incidence X-ray diffraction (GIXRD) patterns of the films from 200 °C to 1100 °C. Peak positions for γ-Al_2O_3 (black, ICSD: 40200[29]) and α-Al_2O_3 (red, ICSD: 10425[28]) are shown for reference.

Local Structure

Solid-state ^{27}Al NMR spectra were obtained for a separate set of alumina films annealed at 200 - 1100 °C, prepared in parallel with those examined by GIXRD. As a quadrupolar species, ^{27}Al has a nuclear spin quantum number, $I = 5/2$. The solid-state NMR spectra were collected at high magnetic field (19.96 T) and are shown in Figure 2.2. The spectra are that of the central transition, and NMR resonances are similar to lineshapes observed previously in crystalline-Al_2O_3,[31] amorphous glasses,[23] metal-organic-chemical-vapor-deposited (MOCVD) Al_2O_3 thin films,[11] and atomic layer deposited (ALD) Al_2O_3 thin films.[19] At this high field, the $^{[4]}$Al, $^{[5]}$Al, and $^{[6]}$Al ^{27}Al sites are capable of being resolved (Figure 2.2). Consistent with the GIXRD data, the spectra for the two highest temperature films are composed of only $^{[4]}$Al and $^{[6]}$Al sites, and this

observation is in agreement with ^{27}Al NMR of γ-Al_2O_3[32] (noting that α-Al_2O_3 only displays $^{[6]}$Al sites).[33] At lower temperature annealing, where GIXRD indicates that the films are amorphous, the NMR spectra show all three ($^{[4]}$Al, $^{[5]}$Al, and $^{[6]}$Al) coordination environments.

The spectra were deconvoluted and fit to three ^{27}Al resonances using the Dmfit program.[3] Similar to prior studies of Al_2O_3 films by NMR,[7] the "Czjzek" model--which accounts for the statistical disorder of Al environments that may be observed--was implemented within the Dmfit program.[24,25,34] The Czjzek model creates a joint probability distribution of the principal value V_{ZZ} of the diagonalized electric field gradient (EFG) tensor and of the quadrupolar asymmetry parameter η_Q, which impact the estimate of the diagonalized EFG tensor elements. The parameters used to simulate the NMR lineshape include the averaged isotropic chemical shift (δ_{ISO}), chemical shift distribution (δ_{CS}), the averaged quadrupolar coupling constant (CQ) and amplitude. These latter four parameters were allowed to optimize for each ^{27}Al resonance. The percentage of each $^{[n]}$Al was then calculated from the Czjzek-optimized simulated fits and are summarized in Table 2.1. A full table of parameters used in the Dmfit simulations are provided in the Supporting Information Table AA1.

Table 2.1: Relative areas of deconvoluted ^{27}Al NMR spectra (normalized to 100%), and average coordination number (CN) for Al_2O_3 films.

Ta (°C)	$^{[4]}$Al	$^{[5]}$Al	$^{[6]}$Al	CN
200	22.1	39.0	38.9	5.17
300	33.7	45.4	20.9	4.87
400	40.6	50.6	8.8	4.68
500	48.0	41.7	10.3	4.62
600	47.9	42.8	9.3	4.61

700	49.6	42.1	8.3	4.59
800	49.4	38.8	11.8	4.62
950	33.8	5.9	60.3	5.26
1100	31.0	0.00	69.0	5.38

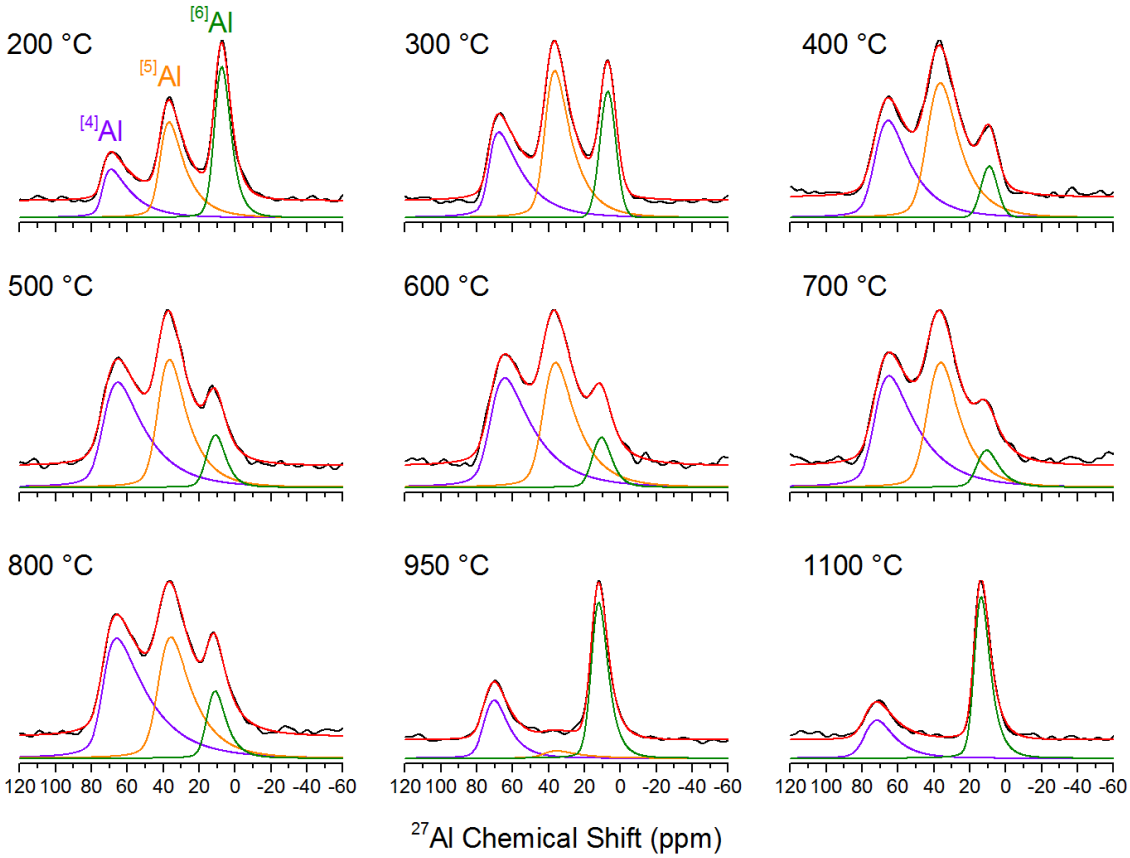

Figure 2.3. One-dimensional ^{27}Al MAS NMR spectra of the central transitions of Al_2O_3 thin films annealed at temperatures indicated (200 ˚C to 1100 ˚C). The NMR lineshapes have been deconvoluted into the individual Al coordination ($^{[n]}$Al) environments shown in purple ($^{[4]}$Al), orange ($^{[5]}$Al) and green ($^{[6]}$Al) lineshapes, the summation of the NMR resonances shown in red. The data have been normalized to the highest intensity peak.

Annealing temperature is plotted, along with the relative ^{27}Al peak areas for $^{[4]}$Al, $^{[5]}$Al, and $^{[6]}$Al. In keeping with prior studies of ^{27}Al ssNMR, the average coordination number, $\overline{CN}$, (graphed in Fig. 6) was calculated using these peak areas, as shown in Equation 2.1.[11]

$$\overline{CN} = \frac{\%^{[4]}Al \cdot 4 + \%^{[5]}Al \cdot 5 + \%^{[6]}Al \cdot 6}{100} \qquad \text{Eq. 2.1}$$

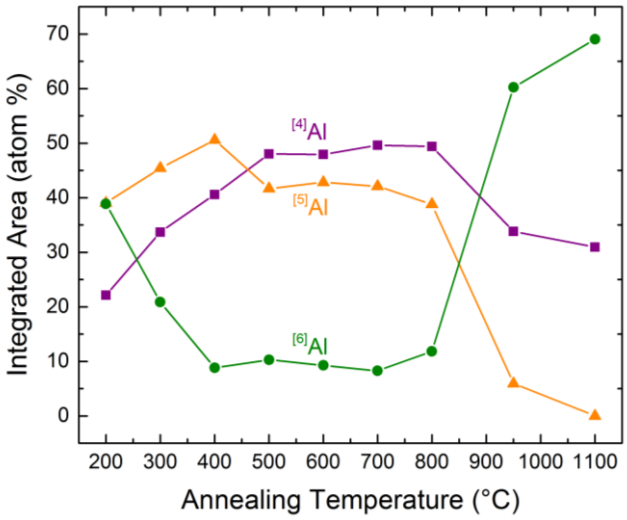

Figure 2.4. Plot of Al coordination number versus annealing temperature from ^{27}Al SSNMR data. (a)The integrated area of the deconvoluted ^{27}Al NMR resonances are $^{[4]}$Al (purple squares), $^{[5]}$Al (orange triangles), $^{[6]}$Al (green circles). (Color online.)

Morphology

Cross-sectional SEM images are displayed in Figure 2.4 for films annealed at 300 °C, 800 °C, 950 °C, and 1100 °C. The silicon substrate is also evident, including a thin layer of native SiO_2. The morphology of the Al_2O_3 films changes with annealing temperature, as evidenced by texturing in films annealed at 950 °C and 1100 °C, which implies the growth of crystalline phases of Al_2O_3, consistent with GIXRD and NMR data. Smooth textureless films are observed at lower temperatures (300 °C, 800 °C), consistent with an amorphous film. Additionally, the SiO_2 layers grows to approximately 20 nm at 950 °C and further to 90 nm at 1100 °C, which is consistent with reports of thermally grown SiO_2.[35,36] A full series of SEM images of the films annealed between 300 °C and 1100 °C can be found in Figure AA2.

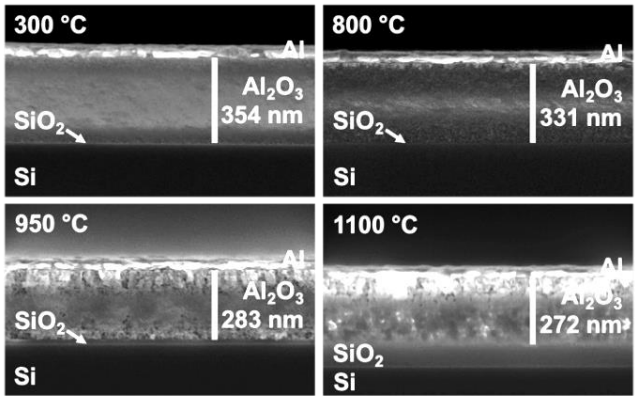

Figure 2.5. Cross sectional SEM images of four films prepared by PIC at annealing temperatures: 300 ˚C, 800 ˚C, 950 ˚C, and 1100 ˚C. A full series of SEM images may be found in Figure S10.

Chemical Processes with Heating

Figure 2.5 shows the FTIR spectra of the thin films annealed from 200 to 1100 °C (as labeled). The most discernible difference in the spectra is the loss of the hydroxyl (O-H) stretching vibration at 3500 cm^{-1}.[37] The water (O-H) stretching mode decreases substantially by 400 °C revealing that most residual water and hydroxides are removed from the film at this temperature. The nitrate (N-O) vibrational modes at 1420 cm^{-1} and 1360 cm^{-1} follow a similar trend, indicating the loss of nitrate counter ions by 400 °C. The modes between 400 to 900 cm^{-1} are commonly attributed to the Al_2O_3 (Al-O) stretching vibrations, and these modes sharpen at the higher temperatures where α- and γ-Al_2O_3 crystallize.[38,39] The modes at 1600 cm^{-1} are H_2O rocking vibrations from bound waters.[38] The peak at 1240 cm^{-1} corresponds to Si-O-Si vibrations; this mode increases in intensity with increasing temperature consistent with SiO_2 growth. Such an interfacial silicon dioxide layer grows between the silicon substrate and the thin film,[35,36] which agrees with the cross sectional SEM images, in Figure 2.4 (and Figure AA2).

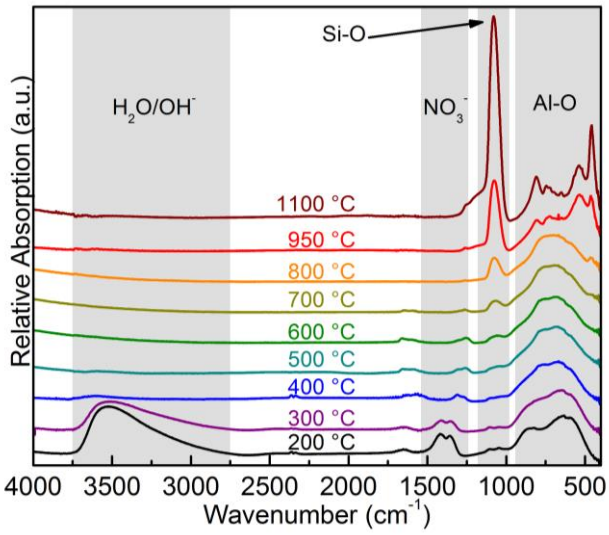

Figure 2.6. FTIR spectra of the thin films annealed from 200 °C to 1100 °C.

Aggregate Analysis of Film Evolution

Considering the local, chemical and structural information together, a picture emerges for which three distinct 'regions' can be discerned as films are heated. The first region is in the annealing temperature range between 200 °C to 400 °C (from Figure 2.3). In this region, the amorphous films are densifying as water and nitrate are expelled. Solid-state ^{27}Al NMR indicates the local structure of the film changes considerably in that there is a decrease in the $^{[6]}$Al sites with concomitant increases in both the $^{[4]}$Al and $^{[5]}$Al sites. These results taken together suggest that the loss of H_2O/OH^- leads to a decrease in the Al coordination such that the $^{[6]}$Al sites with H_2O or hydroxide ligands convert to $^{[4]}$Al and $^{[5]}$Al species. Three likely reactions which result in the loss of water are depicted in Scheme 1. Reactions 1 and 2 are condensation reactions resulting in the loss of two hydroxide ligands and the formation of a bridging oxide species. The difference between the two is the coordination of the initial ligands. When two bridging hydroxides are replaced with a bridging oxide, the coordination of each Al decreases by

one. The third reaction simply shows the release of a ligating H_2O, which also results in a decrease in Al coordination. The effect of the loss of NO_3^- on the local structure of Al is not discussed as this effect is minimal as NO_3^- is rarely a coordinating ion in Al^{3+} species.

Scheme 2.1: Schematic view of the structural change in Al thin films. All "Al" in the scheme are in the 3+ state. Spectator ligands are not shown. In this study, all Al centers are coordinated by 4-, 5- or 6-oxo, hydroxo or aquo species.

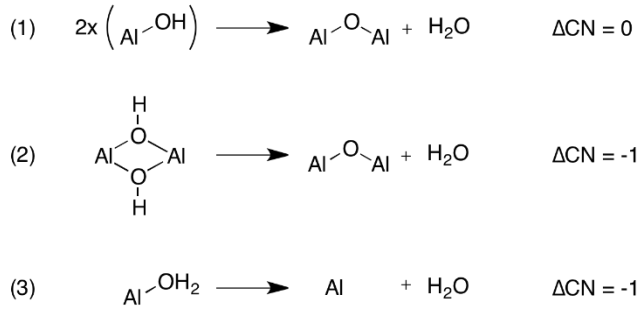

The second region of interest is the annealing temperature range from 400 °C to 800 °C. In this region the films are relatively stable. They remain amorphous, with little change in the FTIR spectra. ssNMR indicates the films are undergoing relatively small structural changes between 400 to 800 °C as the film settles on an amorphous structure with a static local coordination.

Films annealed to temperatures > 800 °C exhibit significant change in film structure and chemical composition. GIXRD patterns indicate that crystalline phases of γ- and α-Al_2O_3 are forming in the films. This is corroborated by the ssNMR spectra where the $^{[5]}$Al site intensity decreases and disappears, and the $^{[6]}$Al becomes the dominant coordination environment. Pure α-Al_2O_3 would be entirely $^{[6]}$Al,[31] while pure γ-Al_2O_3 is a mix of $^{[4]}$Al and $^{[6]}$Al.[40,41] The integrated areas of the $^{[4]}$Al and $^{[6]}$Al site resonances at 1100 °C match the γ-Al_2O_3 structure as described by Ferreira and co-workers (α-Al_2O_3 corundum, is fully $^{[6]}$Al, but not readily distinguished by NMR from the γ polymorph in a mixture).[42] The cross-sectional SEM images corroborate that crystallization occurs in this

region. The presence of sharp Al_2O_3 (Al-O) stretching vibrations (between 400 - 900 cm^{-1}) in the FTIR spectra are also consistent with crystalline structures.[38,39]

Metastability of Amorphous Aluminum Oxide

The coordination environment of Al in amorphous Al_2O_3 thin films deposited by MOCVD has been investigated with ssNMR by Sarou-Kanian et al.[11] In their study, they vary the effect of substrate temperature during deposition. Qualitatively the average coordination number ($\overline{CN}$) of Al in their films is similar to what we report here: an initial high value at low temperatures followed by a decrease in the average coordination of Al followed by an increase in the average coordination of Al at higher temperatures (presumably upon crystallization). Of particular interest is the good quantitative agreement in Al coordination from 400 to 600 °C. This suggests that the average coordination environment of amorphous Al_2O_3 is independent of synthetic route. Between 300 °C and 400 °C the small difference in average coordination numbers between PIC and MOCVD samples is likely due to ligand differences and composition in the films at those low temperatures due to differences in synthetic route. The films studied here contain nitrates, hydroxides and waters at low temperatures the MOCVD fabricated films may contain hydroxides and partially reacted isopropanol ligands. The most notable difference in the plots of the average coordination environment vs. temperature between the two deposition methods is the temperature at which high (> 5.2) average coordination numbers is first witnessed, 700 °C for MOCVD, 950 °C for spin casting shown here. We propose that this is not due to fundamental differences in the films but is due to the difference in the deposition method. Prompt inorganic condensation consists of depositing an aluminum nitrato-hydroxo-aqua "$Al(OH)_x(NO_3)_{3-}$

$_x(H_2O)_y$" gel followed by an anneal that removes ligands at low temperature (200 - 400 °C) and provides thermal energy for diffusion, reorganization and crystallization at high (950 - 1100 °C) temperatures. All of the material is deposited before annealing at high temperatures, thus the activation energy for bulk diffusion in the oxide (all ligands are decomposed by the 800 - 950 °C transition) must be overcome for reorganization and crystallization to occur. In the MOCVD experiments, the deposition is a continuous growth process (decomposition of aluminum tri-isopropoxide) proceeding at the surface of the films at the substrate temperature. In this case the thermal energy required to produce a crystalline film is determined by the activation energy of surface diffusion and not bulk diffusion. The activation energy for surface diffusion on Al_2O_3 (modeled < 1 eV)[43] is less than that of bulk diffusion (measured > 4 eV).[14] It is likely that an Al_2O_3 film deposited by MOCVD at 480 °C followed by a post deposition anneal at 700 °C in air would have a low average coordination number of 4.5-4.6, similar to that observed in this study.

In addition, Lee et. al. has measured the average coordination of Al in a-Al_2O_3 films deposited by PVD at room temperature and by plasma enhanced atomic layer deposition at 200 °C.[19] This suggests again that the kinetically stabilized a-Al_2O_3 phase lies at a local minimum that is accessible by a host of thin film deposition methods.[13] Lee has also measured effect of annealing on the PVD deposited films reporting conversion to possibly to γ-Al_2O_3 (mix of $^{[4]}$Al and $^{[6]}$Al) starts at 800 °C with full conversion to α-Al_2O_3 (only $^{[6]}$Al is present) by 1200 °C.[17]

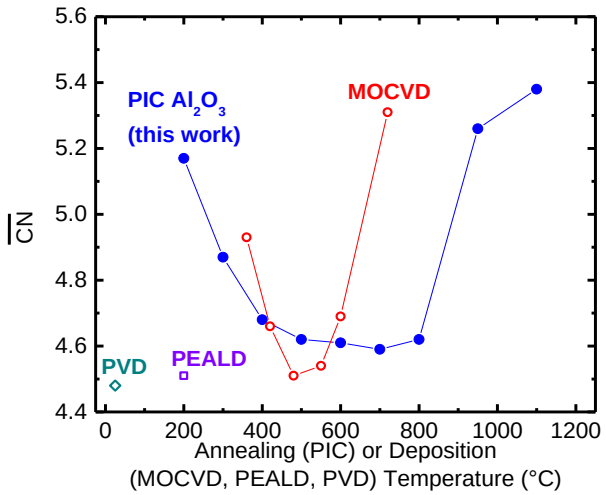

Figure 2.7. Comparison of the average coordination of aluminum in the aluminum oxide thin films deposited at different temperatures by different techniques and annealed at different temperatures.[16,17,44]

Dielectric Response and Structure

Film structure provides a key element to understanding film properties and for tuning future syntheses and preparations for desired functions. One such property is the dielectric constant. The aluminum oxide thin films examined in this study exhibit dielectric constants that range from almost 11 to 6. This large range arises from changes in the chemical, macroscopic, and local structure. Figure 2.7 depicts changes in the films dielectric response concomitant with spectroscopic characterization across the annealing temperatures investigated in this study.

The dielectric constant and concentration of $^{[6]}$Al as a function of annealing temperature is shown in Figure 2.7, and these correlate closely with one another. In principle, $^{[6]}$Al should be more polarizable than $^{[4]}$Al or $^{[5]}$Al, based on an analysis of radius ratios (Al is small for octahedral coordination by O). However, ascribing too much significance to this correlation neglects chemical and long-range structural changes which also must contribute to the dielectric constant.

In the 200 to 400 °C region, the film exhibits a decrease in the dielectric constant from ~11 (200 °C) to ~6 (400 °C). This decrease in the dielectric constant is probably due to elimination of residual water, hydroxides and nitrates in the films (as observed by FTIR), creating a less polarizable film. As the films are annealed from 400 to 800 °C, the dielectric constant is largely unaffected. Similarly, the $^{[6]}$Al content does not change over this temperature range. The ~ 10 - 15% increase in the $^{[4]}$Al (at the expense of the $^{[5]}$Al species) from 400 to 800 °C appears to have no effect on the dielectric constant.

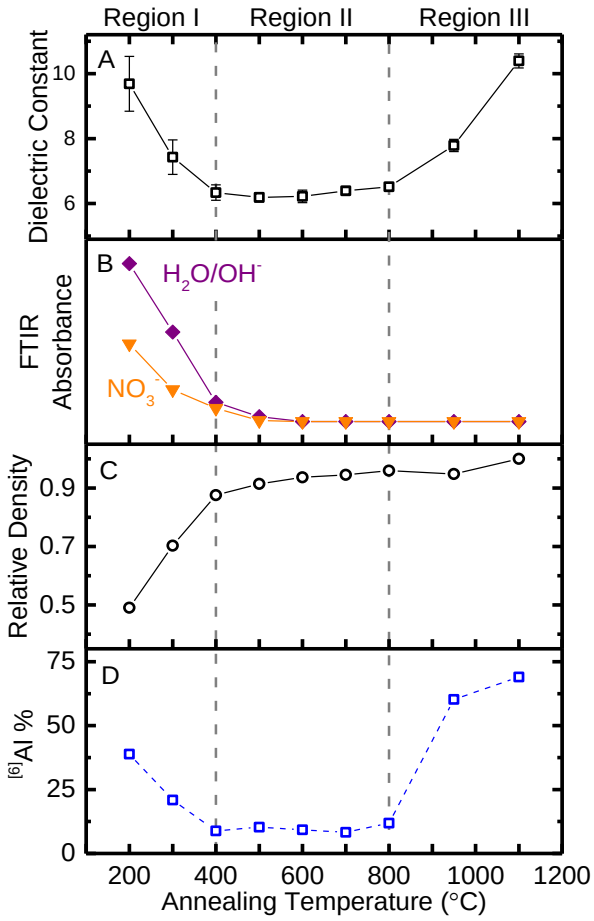

Figure 2.8. (A) dielectric constant at 10 kHz, (B) FTIR absorbance of O-H and O-N stretching modes, (C) relative density and (D) $^{[6]}$Al content of films (from ^{27}Al SSNMR) vs. annealing temperature. The frequency dependence of the dielectric constant at different annealing temperature is presented in Figure S3.

When the films start to crystallize (> 800 °C), the dielectric constant increases from ~6 to ~10. While this increase does correlate with increased $^{[6]}$Al concentration, the films are also densifying and crystallizing in this region which should also increase the dielectric constant. From 800 to 950 °C, the dielectric constant increases by 21% to a value of 7.5, and the relative density increases by a similar fraction (17%). Densification of the film increases the density of polarizable electrons that contribute to the electronic portion (high frequency/visible-optical frequency) of the dielectric constant. Densification of the film is a consequence of the conversion of $^{[4]}$Al and $^{[5]}$Al to $^{[6]}$Al sites.[45] The endpoint of this temperature range is where γ-Al_2O_3 appears, which has a less open network and a higher density than amorphous Al_2O_3.

Once the film has been annealed to 1100 °C, diffraction shows the structure is a mixture of γ-Al_2O_3 and α-Al_2O_3 (Figure 2.1). The dielectric constant increases by 33% at this high temperature to a value of 10 yet the relative density only increases by 4%, not nearly enough to explain the dramatic increase in dielectric constant. In addition, ssNMR shows only a small change in the amount of $^{[6]}$Al for the 1000 and 1100 °C anneals.

Conclusion and Bridge

We have investigated the decomposition of $Al(OH)_X(NO_3)_{3-X}$ in a thin film morphology to the formation of amorphous Al_2O_3 and finally the crystallization of the film at higher temperatures to γ -Al_2O_3 and α-Al_2O_3. By probing the chemical structure with FTIR and the local coordination with ssNMR we have determined that the film does not reach a stable amorphous structure until the majority of H_2O, NO_3^- and OH^- ligands have been decomposed. Interestingly, the ‘stable’ amorphous structure formed by solution processing is very similar to that of amorphous Al_2O_3 thin films deposited by MOCVD,

ALD and PVD. This suggests that the amorphous Al_2O_3 structure may sit in a local minimum in the energy landscape which is, as of yet, inaccessible from a bulk melt-quench approach but readily accessible from thin film reactive-quench deposition techniques.[13] Lastly, we have correlated large changes in the dielectric constant over the range of annealing temperatures with the changing chemical structure, physical properties and physical structure. This comprehensive analysis of the formation of Al_2O_3 films from $Al(OH)_X(NO_3)_{3-X}$ molecular aqueous precursors provides a detailed understanding of the chemical evolution of solution-deposited films.

The techniques employed and insights gleaned from this study are broadly relevant to other aqueous solution-deposited thin films, and amorphous metal oxide thin films. For example, there has recently been substantial work in the area of amorphous oxide semiconductors for TFTs, electrically leaky chemically stable amorphous TiO_2 for protection of photoanodes and a range of amorphous metal oxide large band gap dielectrics for microelectronics.

With an understanding of the formation processes, long range and local structure of Al_2O_3 thin films deposited from an aqueous molecular precursor more complex precursors and films can begin to be studied. In particular, we look at the possibility of fabricating transition metal oxide aluminum oxide amorphous alloys. By utilizing the knowledge gained in this study, ideal annealing temperatures can be targeted. With a kinetically stable amorphous product in mind we desire a low annealing temperature to minimized the thermal energy available for diffusion and crystallization of transition metal oxides, transition metal aluminates or aluminum oxide. Additionally, we know that open networks based on low coordinated metals and oxygen are more stable in the

amorphous state than their closed network counterparts. Lastly, a minimum annealing temperature is required to decompose all precursor components. With these processes in mind we select an annealing temperature of 450 °C at this temperature all precursor components are decomposed at a low temperature and the coordination of Al and consequently O is at a minimum. The two component metal oxides fabricated with this approach are presented in the following chapter.

CHAPTER III

AMORPHOUS MIXED-METAL OXIDE THIN FILMS FROM AQUEOUS SOLUTION PRECURSORS WITH NEAR ATOMIC SMOOTHNESS

Portions of this chapter were previously submitted to publish as Kast, M.G.; Cochran, E.A.; Enman, L.J.; Mitchson, G.; Ditto, J.; Siefe, C.; Plassmeyer, P.N. Greenaway, A.L.; Johnson, D.C.; Page, C.J.; Boettcher, S.W. Amorphous Mixed-Metal Oxide Thin Films from Aqueous Solution Precursors with Near Atomic Smoothness. The excerpt to be included was written entirely by me. D. C. Johnson, C. J. Page and S. W. Boettcher provided editorial assistance. E. A. Cochran, L. J. Enman, G. Mitchson, J. Ditto, C. Siefe and P. N. Plassmeyer provided experimental assistance.

Introduction

Amorphous thin films are critical components of modern technology. Silica[46] and hafnium silicate[47,48] are used as gate dielectrics in advanced field effect transistors (FETs), amorphous silicon (a-Si) and silicon nitride are used as contacts and passivation layers in high-efficiency crystalline silicon (c-Si) photovoltaics,[49–51] and amorphous indium-gallium-zinc oxide (a-IGZO) semiconducting channels are used as the active channel in thin film transistors (TFTs).[52] Amorphous metals provide ultra-smooth electrodes in metal-insulator-metal tunnel diode devices.[53] Such practical utility is due to several factors. Amorphous films often make high quality electronic interfaces due to the local bonding flexibility of the amorphous structure[54] without the material limitations and processing requirements of lattice-matched defect-free heteroepitaxy. They form ultra-

smooth and uniform interfaces, in contrast to polycrystalline thin films.[55] Amorphous silicates thus allow for passivation of c-Si surfaces with a minimal concentration of interface defect states,[56] as does hydrogenated a-Si,[57] while also enabling selective charge extraction with appropriate contact engineering. Similarly, a-IGZO maintains high electron mobility in thin channels where the interface with the amorphous dielectric is a substantial fraction of the channel height. Amorphous materials are also kinetic products, which make their elemental composition unbounded by the compositional constraints of thermodynamic phase space. Silica can be alloyed with hafnium oxide to tune the dielectric response,[58] leakage current, and interface mobility. a-Si can be hydrogenated and heavily doped beyond the crystalline solid-solubility limit.[59] a-IGZO's mobility and carrier concentration can be tuned with the ratio of post-transition metals used.[60] Crystalline binary metal oxide alloys also provide mechanisms to tune bandgaps and band positions for solar energy applications through controlled tuning of cation electronic contribution to each band state.[61] Such principles should be directly applicable to amorphous mixed metal oxides.

Compared to bulk amorphous materials (e.g. oxide glasses) which are classically prepared by melt-quench processing,[62–65] thin films offer a broader range of non-equilibrium synthesis techniques to access kinetically stable amorphous phases (e.g. sputtering, pulsed laser deposition, chemical vapor deposition, spin-casting, spray pyrolysis etc.). These deposition methods collectively make use of rapid "chemical/physical quenching" processes whereby atomic or polyatomic species (molecules, ions or radicals with high mobility) are quickly converted via chemical reaction into a 3D network, with low ion mobility.[13] The range of compositions in which

amorphous materials can be made in thin-film form by rapid chemical quench deposition methods has, however, not been investigated.

We demonstrate, using solution processing and a rapid chemical quench via a low-temperature heat treatment that drives precursor decomposition and oxide network formation, the synthesis of ultra-smooth, dense, composition-controlled, mixed-metal oxide amorphous thin films of Al_2O_3 and the first-row transition-metal oxides (TMO_x, i.e. VO_x, CrO_x, MnO_x, Fe_2O_3, CoO_x, NiO, CuO_x and ZnO). The films have a root mean square surface roughness (R_{rms}) << 1 nm and a tunable thickness. The driving forces that determine the maximum concentration of a given TMO_x that can be alloyed with Al_2O_3 and remain amorphous are discussed in light of the formation process's kinetics and energetics rooted in classical glass network theory. Across all TMO_x, amorphous solid solutions are observed when the concentration of TMO_x to total metal is 10% or, presumably, less. Some TMO_x make amorphous solutions with Al_2O_3 to much higher concentrations of TMO_x (e.g. >50%) even though they readily crystallize when prepared alone. Those that phase-segregate yield thin-film materials consisting of crystalline transition metal oxide "c-TMO_x" nanoparticles that are embedded in an amorphous Al_2O_3 "a-Al_2O_3" matrix.

This work therefore lays the foundation for the facile preparation of amorphous oxides that can be *designed* for specific electronic devices or other applications. For example, we note the need for new carrier-selective contacts to increase the efficiency of photovoltaics and photoelectrodes utilizing a wide variety of light-absorbing materials.[66,67] An ideal selective contact is optically tranparent,[67] makes an interface with the absorbing material that has a minimal concentration of recombination sites, and,

critically, provides a large difference in resistance for electrons and holes so that it selects one over the other.[68] For example, thin-film alloys of Al_2O_3, a physically robust[44] network that passivates c-Si, and a TMO_x could provide access to materials where the electronic structure can be systematically tuned in the region of the valence and conduction bands to create multifunctional carrier-selective interfaces. Conduction-band tunable electron selective contacts have been made with amorphous In-Ga-O and Ga-Zn-Sn-O by Zhou et al and show promise when used with organic photovoltaic absorber layers.[69] The ability to systematically and broadly tune composition has further applications in catalysis, for example in tuning metal-oxide support interactions,[70,71] by providing atomically mixed heterogeneous active sites,[72] or by allowing for systematic control over the oxide electronic structure and hence intermediate binding energies.[73] Amorphous metal oxide and multi-metal perovskites oxides are also of interest in adaptive oxide devices.[74] The compositionally controlled, smooth, amorphous mixed-metal oxides developed here might enable tuning redox reactions and ion diffusion in adaptive oxide devices,[74] such as "memristors".[75] Dilute and dilute-amorphous ferromagnetic thin films have been previously investigated. The amorphous alloy film platform presented here could enable fundamental studies into amorphous dilute-multi-metal ferromagnetic oxide thin films.[76–78]

Methods

Precursor Preparation

Solutions for spin casting were prepared by mixing at different ratios 1 M aq. solutions (prepared in 18.2 MΩ cm water) of transition metal nitrate or chloride salts with 1 M aq. $Al(NO_3)_x(OH)_{3-x}$ clusters, nominally "flat" $[Al_{13}(\mu_3\text{-}OH)_6(\mu\text{-}$

$OH)_{18}(H_2O)_{24}](NO_3)_{15}$ or "f-Al_{13}" (to avoid confusion with the Keggin isomer).[79–81] Such clusters have been demonstrated to be excellent thin film precursors.[2] Fresh solutions were made < 2 h prior to use for $Fe(NO_3)_3$ and $Mn(NO_3)_2$ containing precursors, which precipitate after extended exposure to air and light. Precursors containing V were prepared over ice by combining precooled solutions of 1 M VCl_3 and f-Al_{13} which were allowed to react (as evident from bubble formation) for 5-10 min prior to spin coating. The final solutions were blue and thus presumably contained the vanadyl cation VO^{2+} with a combination of NO_3^- and Cl^- counter ions. Based on the relative reduction potentials,[82] NO_3^- in f-Al_{13} oxidizes V^{3+} to V^{4+}, as evidenced by the color change from dark green (aq. V^{3+}) to blue (aq. VO^{2+}) upon reaction with f-Al_{13}. The reaction is more violent and results in a brown precipitate if carried out at room temperature.

f-Al_{13} cluster solutions were made using literature procedure. Briefly, 60 kC of reductive charge (at 150 mA) was passed per mole of $Al(NO_3)_3$ (1.5 M starting concentration) across an 80 cm^2 Pt mesh (working, reducing potential) and a small Pt coil (counter, oxidizing potential) electrodes in separate fritted compartments with stirring. This drives $Al(NO_3)_3$ oligomerization by consuming H^+ in the working electrode compartment and driving NO_3^- to the counter electrode compartment.[80] After electrolysis, f-Al_{13} cluster solution concentration was standardized by thermogravimetric analysis of 2 ml of Al_{13} heated to 500 °C in a box furnace. At a final concentration of 1 M (relative to Al^{3+}) the f-Al_{13} solution had a pH of 3. TMO_x-P_2O_5 alloys were prepared by mixing transition metal nitrate solutions with 1 M phosphoric acid. Chemical supplier and purity info is provided in Table AB1.

Thin Film Deposition

Single-side polished Si (100) substrates were scored with a diamond scribe on the unpolished side and cleaved into 2 × 2 cm squares. Substrates were loaded into a Teflon boat that held the samples in a vertical configuration. Substrates were washed in a sonicator for 10 min in a solution of 6.25% Contrad 70, rinsed with nanopure water for 30 s, loaded onto a spincoater and spin rinsed for 10 s, spin dried for 20 s at 3000 RPM, and placed on a hot plate at 100 °C for 5 min to finish drying. The substrates were then plasma cleaned in an O_2/N_2 mixture for 10 min, spin rinsed with nanopure water for 5 s, and spin dried for 25 s. Precursor solution was deposited dropwise from a syringe through a 0.2 μm filter onto the substrate until the entire surface was wetted and then spun at 3000 RPM for 30 s. The sample was immediately moved to an Al block at 150 °C on a hot plate (as measured by a thermocouple embedded directly in the Al block). After 5 min at 150 °C the samples were moved to a hotplate at 450 °C for 30 min.[60,79,83–86]

Characterization

X-ray reflectivity (XRR) data was collected on a Bruker D8-Discover using a Cu Kα x-ray source. Data was collected in a θ-2θ geometry after sample alignment.[87] Data was analyzed in Rigaku's GlobalFit software. Fourier transform fits were used to determine the R_{rms}.

X-ray diffraction (XRD) data was collected in a grazing incidence XRD (GIXRD) geometry on a Rigaku SmartLab. The Cu source was held at 0.5º above the sample and the scintillation point detector was swept from 10 to 70º in 0.1º steps with an integration at each step of 30 s. A Ni filter was used to filter out Cu Kβ interference.

Atomic force microscopy (AFM) images were collected in tapping mode on a Bruker Dimension Icon. Si tapping mode probes (42 N m^{-1}, 320 kHz) were used. Images were collected over 500 nm square windows, with 256 measurements per line and 256 lines per image at a scan rate of 1 Hz and scan velocity of 1μm s^{-1}. Three images at different locations were collected. All images had 1st order flatten and 3rd order pane fits applied. The instrument used has a 30 pm background noise level.

Results and Discussion

We synthesized amorphous, atomically smooth thin films of the electronic insulator Al_2O_3 alloyed with eight different transition metal oxides and combinations of these. First, we discuss the design of the aqueous precursor chemistry that enables the solution synthesis of these new materials. We then provide a detailed analysis of the formation processes and solid state chemistry, and discuss how dense amorphous thin films can be designed and synthetically targeted.

Synthesis of mixed metal amorphous oxide films from solution

Deposition via spin coating of a dissolved species generally proceeds through two phases.[88] During the first phase, mass is lost from the film as material is flung from the substrate until a steady-state thickness of precursor solution is established which depends on the rotational speed, substrate diameter, solution surface tension, solution viscosity and substrate surface energy. In the second phase, the solution concentrates as solvent evaporates from the top surface of the liquid phase film,[88,89] driving precipitation of the solid film precursor as either poly-crystalline or amorphous materials (which often incorporate solvent as gels).

With these processes in mind, there are several design parameters for precursors needed to make dense, amorphous, smooth, mixed-metal-oxide films. When multiple metal salts are used they must be co-soluble (at least kinetically on the time frame of spin processing). The solvent vapor pressure of the saturated precursor film (here water) must be sufficiently high. Precursors with low solvent vapor pressures (e.g. $AlCl_3$) form poor films as they do not dry and gel during the spinning stage. The precursors should also have a minimal number of coordinating ligands or counter ions, as removal of these upon heating can lead to porosity.[60] The counter ions should also decompose at low temperature, as do many nitrate salts, to allow for chemical quenching of mixed-metal-oxide films.

We have designed our synthetic approach with these criteria in mind. We utilize oligomeric f-Al_{13}[79–81] as one component of the precursor solution and combine it with nitrate salts of Cr, Mn, Fe, Ni, Co, or Cu, or VCl_3. The f-Al_{13} clusters are synthesized by simple electrolysis of $Al(NO_3)_3$ salt solutions across a glass frit. The electrolysis consumes protons and increases the Al^{3+}:NO_3^- ratio in the precursor solution, driving oligomerization and cluster formation. Cluster/oligomer precursors provide smooth dense amorphous aluminum oxide thin films with physical and electronic properties approaching those of ALD-deposited alumina.[2,79] The clusters are soluble at ~ pH 3 and compatible with a large number of transition-metal nitrate precursors which are also stable under mildly acidic conditions. Because the f-Al_{13} clusters are partially condensed they have relatively few counter-ions that must be decomposed upon heating, leading to high film density. The large f-Al_{13} oligomers mix with the transition-metal nitrate salts homogeneously, and appear to prevent salt crystallization at room temperature due their

large size and low diffusivity. All of the mixed oxides thus remain smooth and amorphous with sufficient Al content, while the single component metal oxide films do not.

After spin-casting, the films are dried on a hot plate at 150 °C and rapid color changes due to reflective interference are observed as the solvent evaporates and the film thickness decreases. Nitrate anions also leave in the form of water/nitric acid azeotropes (boiling point of 120 °C).[38] During a second annealing step, at 450 °C for 30 min, the nitrates fully decompose, presumably leaving as various NO_x gases, and the precursor film is converted into a dense oxide by condensation of hydroxides to form bridging oxide bonds.[60,79,84,85,90,91] We refer to this annealing step as a chemical quenching, because the bridging metal oxide chemical bonds formed at low temperature may kinetically stabilize the initial amorphous film.

Thin film characterization: film quality and amorphous nature

Figure 3.1 shows GIXRD data collected on 30-nm-thick films of $TM_yAl_{1-y}O_x$ and $TM_yP_{1-y}O_x$, where TM is a transition metal cation. $Co^{3+/2+}$, Ni^{2+} and Cu^{2+} phase segregate at $y \geq 30$ % ; diffraction peaks can be indexed to known oxide phases (spinel Co_3O_4[92], rock salt NiO[93] and tenorite CuO[94], respectively). $V^{4+/5+}$, $Cr^{3+/6+}$, Mn^{3+}, Fe^{3+} and Zn^{2+} do not show clear Bragg diffraction until higher concentrations of TM, indicating different crystallization and phase segregation kinetics and energetics, as discussed below. When they do crystallize, they crystallize as Shcherbinaite-V_2O_5,[95] α-Cr_2O_3,[96] α-Mn_2O_3,[97] α-Fe_2O_3,[98] and hexagonal ZnO[99] respectively. No periodic trend in crystallization behavior is evident from our data.

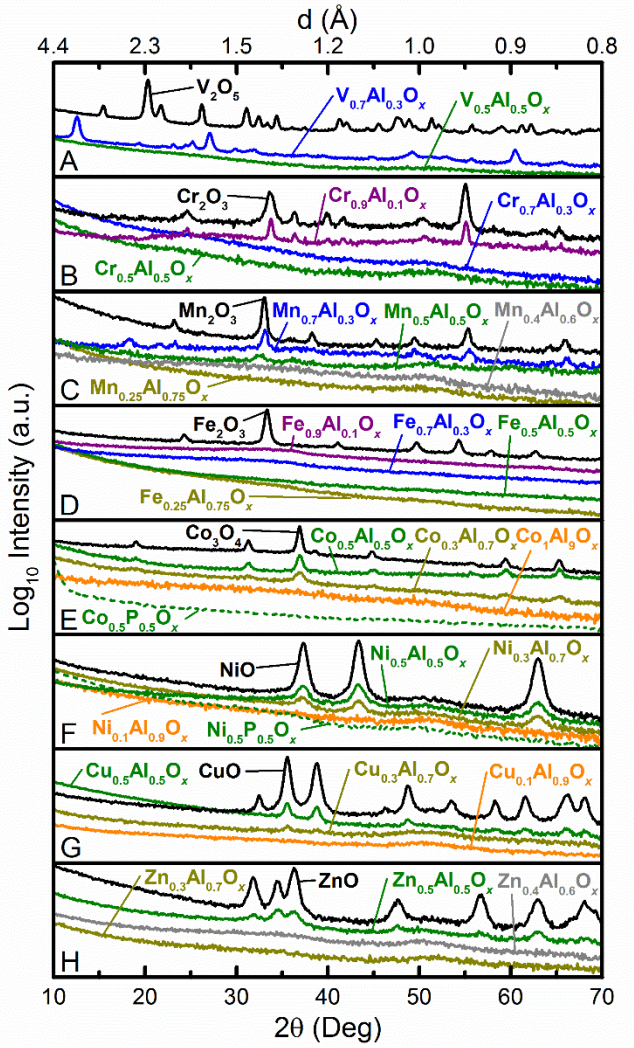

Figure 3.1. GIXRD patterns of (A) $V_yAl_{1-y}O_x$, (B) $Cr_yAl_{1-y}O_x$, (C) $Mn_yAl_{1-y}O_x$, (D) $Fe_yAl_{1-y}O_x$, (E) $Co_yAl_{1-y}O_x$, (F) $Ni_yAl_{1-y}O_x$, (G) $Cu_yAl_{1-y}O_x$ and (H) $Zn_yAl_{1-y}O_x$ with y = 1 (black), 0.9 (purple), 0.7 (blue), 0.5 (green), 0.4 (dark grey), 0.25 or 0.3 (dark yellow), and y = 0.1 (orange). Panels (E) and (F) also show GIXRD patters of $Co_{0.5}P_{0.5}O_x$ and $Ni_{0.5}P_{0.5}O_x$ films, respectively, with dashed green lines. All films were annealed at 450 °C for 30 min. $Mn_7Al_3O_x$ and $V_7Al_3O_x$ stand out as films that show minimal and significant differences respectively in their crystallization behavior compared to the pure TMO_x films. $Mn_7Al_3O_x$ shows one extra diffraction peak at 18.2° and shoulders on some of the larger peaks; these are likely due to the presence of different MnO_x phases with slightly different Mn oxidation states and stoichiometry. The phase(s) present in the $V_7Al_3O_x$ film are illustrated in Figure AB1.

To assess the possibility of small crystallites in the films that appear amorphous by x-ray techniques, we used transmission electron microscopy (TEM). Figure 3.2 shows

high-resolution TEM cross-sections prepared by focused ion beam milling of Al_2O_3 and $Fe_{0.5}Al_{0.5}O_x$. In addition, a powder TEM image of $Co_{0.4}Al_{0.6}O_x$ which was mechanically removed from the substrate is shown. The Al_2O_3 and $Fe_{0.5}Al_{0.5}O_x$ films appear amorphous, nearly featureless and show Å-level roughness at both interfaces. Crystallites with d-spacing that match the Co_3O_4 phase are apparent in the TEM image of $Co_{0.4}Al_{0.6}O_x$. HAADF-STEM was also used to probe the presence of crystallites in the films. These data are shown in Figure AB2 and also indicate a lack of crystalline phase-segregated components.

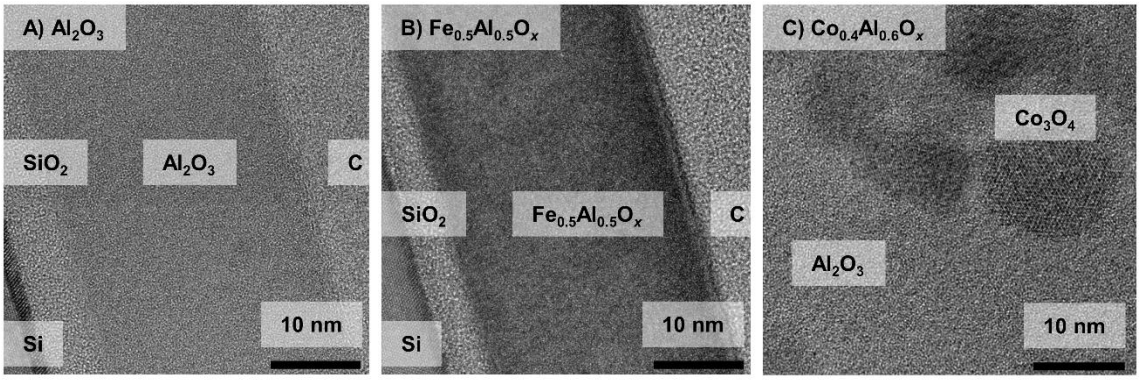

Figure 3.2. TEM images of (A) Al_2O_3, (B) $Fe_{0.5}Al_{0.5}O_x$ and (C) $Co_{0.4}Al_{0.6}O_x$. Note that there are no crystalline regions in the Al_2O_3 and $Fe_{0.5}Al_{0.5}O_x$ films apparent, while the phase segregation is apparent in the $Co_{0.4}Al_{0.6}O_x$.

To understand the effect of phase segregation on film morphology, roughness was measured with XRR (Figure 3.3) and AFM (Figure 3.4). XRR data is used to assess the average correlation of the two interfaces of a film, this can be interpreted as a roughness, though it is dependent on a homogeneous electron density throughout the film.[87] AFM provides a microscopic measure of the surface roughness (convoluted with the tip radius) and an image of the local morphology.[100] For these reasons, roughness measured by XRR is not usually equivalent to that measured by AFM, although the trends are similar (Figure 3.5). Films that lack Bragg diffraction intensity (i.e. that are hypothesized to be

amorphous alloys) show no substantial increase in roughness compared to a pure Al_2O_3 film (i.e. R_{rms} ~ 0.1 nm). Films composed of transition-metal crystallites and alumina show increased R_{rms} of 1 - 2 nm, i.e. approximately an order of magnitude larger than the amorphous films. As is evident from AFM images of $Ni_{0.5}Al_{0.5}O_x$, the increased roughness is correlated with crystalline grain growth and phase segregation (Figure 3.4).

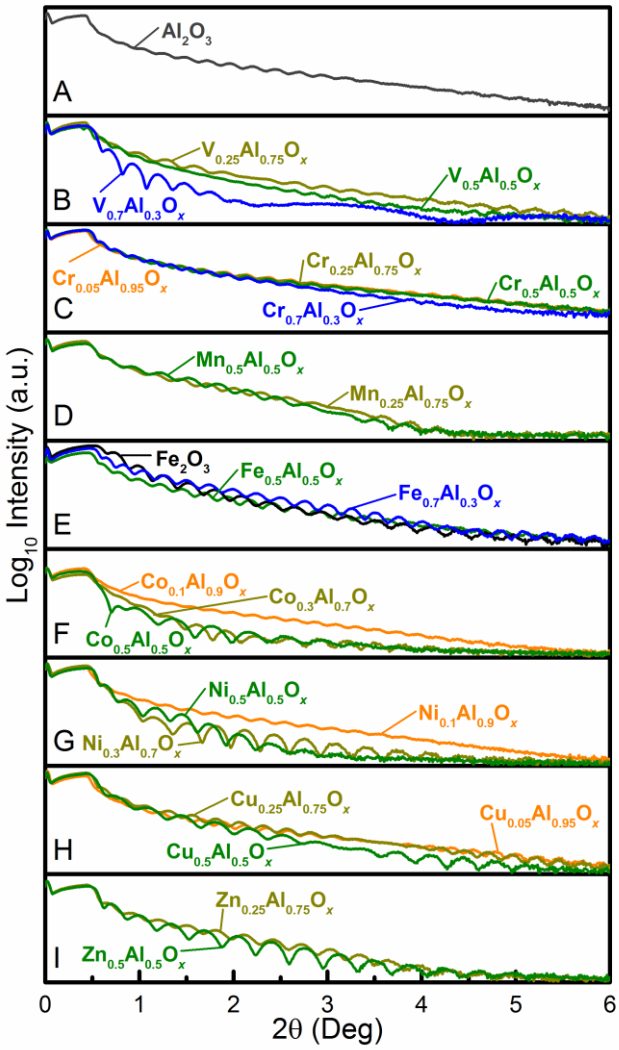

Figure 3.3. XRR of (A) Al_2O_3, (B) $V_yAl_{1-y}O_x$, (C) $Cr_yAl_{1-y}O_x$, (D) $Mn_yAl_{1-y}O_x$, (E) $Fe_yAl_{1-y}O_x$, (F) $Co_yAl_{1-y}O_x$, (G) $Ni_yAl_{1-y}O_x$, (H) $Cu_yAl_{1-y}O_x$ and (I) $Zn_yAl_{1-y}O_x$ with y=1 (black), y=0.9 (purple), y=0.7 (blue), y=0.5 (green), y=0.25 or 0.3 (dark yellow) and y=0.1 or 0.05 (orange). For each TMO_x the roughness is higher when TMO_x crystallites are present. In some cases, the films become sufficiently rough that interference effects needed for Kiessig fringes are lost.

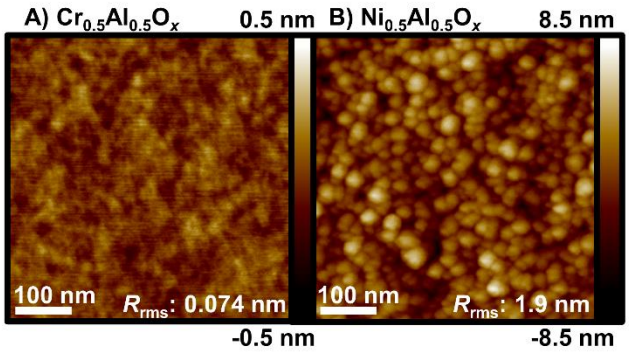

Figure 3.4. Representative AFM images of (A) an amorphous film ($Cr_{0.5}Al_{0.5}O_x$) and (B) a film with transition-metal crystallites ($Ni_{0.5}Al_{0.5}O_x$). Note the near-atomic roughness of the amorphous films and the defined particulate structure present in the $Ni_{0.5}Al_{0.5}O_x$ sample, presumably consisting of NiO crystallites protruding above the surface of the amorphous Al_2O_3.

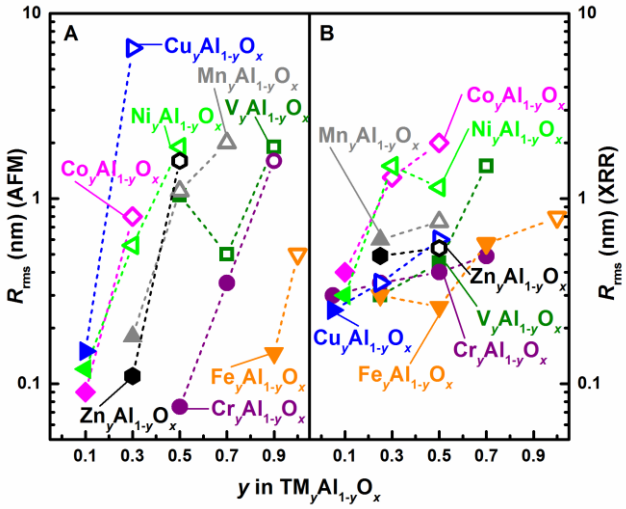

Figure 3.5. (A) R_{rms} measured by AFM and (b) XRR as a function of the alloy identity (label) and the concentration of the TMO_x in the films. Amorphous solid solutions are shown with solid markers, segregated mixtures of transition metal oxide crystallites and amorphous alumina are shown with open markers. Note the near universal dramatic increase in roughness in films that contain segregated crystallites indicated by open markers.

The low R_{rms} of the amorphous compositions (1-2 Å for Fe, Co, Ni, Cu, Zn and 3-10 Å for V, Cr and Mn) compare favorably with state-of-the-art deposition techniques

such as ALD, under *ideal* conditions.[101] This exceptional smoothness corresponds to the distance of two metal-oxygen bonds and makes integration into devices for a variety of applications feasible even for films only a few nm in thickness.[102] Accessing such amorphous mixed metal oxide films, with controlled composition in an ultra-smooth morphology would be difficult by other techniques. Both chemical vapor and atomic layer deposition techniques are highly sensitive to the individual precursor and cross reactivity when ternary, quaternary and higher order compositions are targeted. Significant precursor design work is needed to enable any given composition.[103,104] Physical vapor deposition approaches (sputter, pulsed-laser deposition, evaporation) are dependent on a custom target for each film composition or a deposition system with multiple targets or crucibles and highly controlled power to each.[105]

Although primarily binary metal oxides were investigated here, the approach enables complex films with mixtures of many different cations. Proof-of-principle four- and six-component films are illustrated in the final section below, after we discuss the chemical principles enabling amorphous film synthesis.

Film formation and the driving forces for phase segregation

Electronic applications of mixed-metal-oxide films require smooth surfaces and homogeneous composition. The data above demonstrates that the solution deposition and "chemical quenching" approach enables the synthesis of amorphous films, with near atomic smoothness, over a large compositional space. Some compositions, however, yield amorphous films over larger composition ranges than others. Understanding the fundamental physical and chemical interactions that lead to amorphous or phase-

segregated films is therefore important to guide further synthetic efforts and enable applications.

Film formation proceeds through evaporation of solvent at room temperature, the removal of nitrates and water by evaporation of the nitric acid/water azeotrope at intermediate temperatures and the decomposition of $TM(NO_3)_x$ to TMO_x at elevated temperatures. The formation of $TM_yAl_{1-y}O_x$ is dependent on the precipitation of the f-Al_{13} and $TM(NO_3)_x$ to form a gelled, atomically mixed precursor film and the decomposition of the $TM_yAl_{1-y}(OH)_x(NO_3)_z$ gel to yield $TM_yAl_{1-y}O_x$. Differences in either the solubility of the $TM(NO_3)_x$ relative to that of f-Al_{13} or a large difference in the decomposition temperature of the $TM(NO_3)_x$ relative to f-Al_{13} might thus cause phase segregation.

The aqueous solubilities of the metal nitrates studied span a range of 1-10 M (Figure 3.6C). CoO_x, NiO and CuO_x phase segregate readily in the mixed oxide thin films, but their nitrate salts have moderate solubilities which are higher than $Fe(NO_3)_3$ and lower than $Cr(NO_3)_3$ which both remain amorphous to high concentrations of transition metal. This analysis suggests precursor solubility is not the dominant effect driving phase segregation. It is likely that under the rapid evaporation conditions prevalent during spin coating that precipitation occurs sufficiently fast that the different precursors co-precipitate even though they may have different solubilities. Further, the hydrated metal nitrates used have melting points between 25 and 75 °C, shown in Figure 6B, which are below their decomposition temperature. The metal nitrates may thus melt prior to decomposition during the annealing process allowing for further mixing.

Bulk thermogravimetric analysis of each $TM(NO_3)_x$ was carried out (Figure AB3) to determine the precursor decomposition temperature plotted in Figure 3.6B along with

melting points of the pure $TM(NO_3)_x$ obtained from literature[106] and with corresponding values for $Al(NO_3)_3$ are plotted in Figure 3.6B. $Ni(NO_3)_2$, $Co(NO_3)_2$ and $Zn(NO_3)_2$ have higher decomposition temperatures than the other $TM(NO_3)_x$. Co_3O_4 and NiO readily phase segregate at more than ~10% concentration, suggesting differences in decomposition temperature between the $TM(NO_3)_2$ and f-Al_{13} drive phase segregation. The fact that ZnO does not segregate until higher compositions is likely related to its d^{10} electron count and concurrent higher local flexibility relative to $Co^{2+}(d^7)$, $Ni^{2+}(d^8)$ and $Cu^{2+}(d^9)$, as discussed below.

Because $V(NO_3)_x$ salts are not stable, VCl_3 and f-Al_{13} were used for the $V_yAl_{1-y}O_x$ precursor. When this precursor is mixed on ice, NO_3^- slowly oxidizes V^{3+} to V^{4+}. Due to this, accurate solubilities and decomposition temperatures for the relevant V containing precursor are not available.

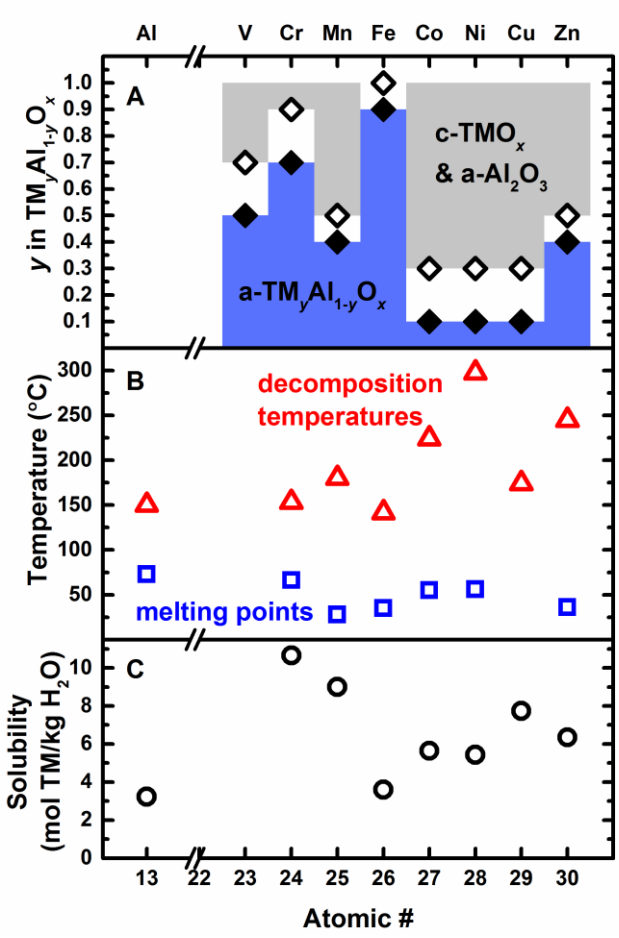

Figure 3.6: (A) Regions of TMO_x identity and concentration where a-$TM_yAl_{1-y}O_x$ and c-TMO_x/a-Al_2O_3 are formed (B), decomposition temperatures (red triangles) and melting points (blue squares) and (C) solubilities of the $TM(NO_3)_x$ and $Al(NO_3)_3$ are shown. Decomposition temperature and solubility is not listed for V as it likely forms a $VO(NO_3)_x(Cl)_y$ species in the precursor solution. Accurate solubility and decomposition data do not exist for this species although there are reports that it decomposes to V_2O_5 upon drying.[107] The decomposition temperature was defined here as the temperature at which the precursor had lost 75% of the total mass lost at high temperature where oxide phases are formed.

Local chemical bonding effects.

The degree to which a particular oxide retains an amorphous structure may be rationalized by the coordinative flexibility of the oxygen anions around the transition metal cations. Table 1 summarizes the composition range over which amorphous mixed metal or phase-segregated nanocrystalline $TM_yAl_{1-y}O_x$ thin films were found and the

proposed reason(s) for the formation of amorphous films which are discussed in this section.

Table 3.1: Overview of amorphous film composition and formation

TMO_x	**range amorphous for $TM_yAl_{1-y}O_x$**	**range phase segregated c-TMO_x a-Al_2O_3**	**rationale for amorphous range***
VO_x	$y \leq 0.5$	$y \geq 0.7$	High Q_M, Low C_O, d^0
CrO_x	$y \leq 0.7$	$y \geq 0.9$	High Q_M, Low C_O, d^0
MnO_x	$y \leq 0.4$	$y \geq 0.5$	Mod. Q_M, Mod. C_O
FeO_x	$y \leq 0.9$	$y = 1$	Mod. Q_M, Low C_O, d^5-HS
CoO_x	$y \leq 0.1$	$y \geq 0.3$	Dilute only
NiO	$y \leq 0.1$	$y \geq 0.3$	Dilute only
CuO_x	$y \leq 0.1$	$y \geq 0.3$	Dilute only
ZnO	$y \leq 0.4$	$y \geq 0.5$	Mod. C_O, d^{10}

* Q_M = oxidation state of the metal cations, C_O = coordination number of oxygen anions, $d^0/d^5/d^{10}$ indicate electron occupancy of the d-states in the transition metal cation.

Based on early glass network theory by Zachariasen, the coordination of the oxygen anions in the metal oxide network affects the energetic stability of amorphous oxide systems.[12,63–65,108] The coordination of oxygen (C_O) can be calculated if the coordination of cations (C_M, based on the coordination geometry), oxidation state of the cations (Q_M) and oxidation state of oxygen (Q_O) are known:[109]

$$C_O = \frac{C_M|Q_O|}{|Q_M|} \quad (1)$$

Lower coordination on oxygen anions results in more-open metal oxide networks (illustrated in Figure AB4). The energetic stability of open networks is less dependent on the crystallinity of the system than would be the case for a closed network due to the fact that short range order can be maintained on the metal centers in a sufficiently open network even when no long-range order is present. If there exists insufficient openness in

the network, strain/distortion must be applied to the local coordination to maintain an amorphous structure; this is energetically unfavorable compared to forming a closed crystalline network. Distortion applied to the local coordination environment is especially unfavorable when the coordinated cations have partially filled d-states due to their ligand field stabilization energy (LFSE).

The occupancy of the valent d-states and the LFSE can be used as a measure of the degree of preference for a particular local structure over another.[110] If the d-states are fully occupied (d^{10}), unoccupied (d^0) or exactly half occupied with no paired electrons "high spin" (d^5-HS) there is no preference for one coordination environment over another due to electronic effects. V^{5+} and Cr^{6+} are d^0, Fe^{3+} is d^5-HS and Zn^{2+} is d^{10}. The energetic penalty for these cations to be in multiple coordination environments is less than that of Mn^{3+}, $Co^{2+/3+}$, Ni^{2+} or Cu^{2+}. d^0, d^{10} and d^5-HS cations can thus adopt low-coordination tetrahedral environments resulting in more open networks (Eq. 1). In particular, this is likely why ZnO forms amorphous alloys in $TM_yAl_{1-y}O_x$ until $y = 0.4$, while CoO_x, NiO and CuO_x phase segregate unless $y \leq 0.1$.

$TM_yAl_{1-y}O_x$ films containing V or Cr cations stay amorphous to high concentrations of TM, $y = 0.5$ and $y = 0.7$ respectfully. Both V and Cr cations in this study likely have average formal charges $>3^+$, larger than the other cations in this study. As seen from the diffraction data (Figure 3.1) VO_x crystallizes with V in the 5+ oxidation state. XPS data of Cr containing films show the presence of Cr^{6+} (Figure AB5). High oxidation states lead to lower coordination numbers of the oxygen anions if the coordination geometry is unchanged (Eq. 1), which stabilize the amorphous state as discussed above. Higher cation oxidation states also result in higher activation energies

for cation hopping and thus slower cation diffusion (as discussed further below).[14,111,112] MnO_x's intermediate oxidation state, +3 when it crystallizes, may allow for amorphous alloys with Al_2O_3 when $y \leq 0.4$, but not at the higher concentrations possible for the Al_2O_3 and VO_x or CrO_x systems.

CoO_x, NiO and CuO_x only alloy with Al_2O_3 in the amorphous state when $y \leq 0.1$. This is likely due to their non-zero LFSE, and low oxidation state. The fact that they remain amorphous at $y = 0.1$ is likely because the TM cations are dilute in the amorphous matrix which allow for kinetic trapping during synthesis. Entropy may also stabilize $Co_yAl_{1-y}O_x$, $Ni_yAl_{1-y}O_x$ and $Cu_yAl_{1-y}O_x$ thin films in the amorphous state at $y = 0.1$, as has been observed in other oxide systems.[113]

If the stability of the mixed metal alloy is indeed dependent on the coordination around network O, then replacing Al^{3+} with a glass-forming cation of higher oxidation state and/or lower coordination number will result in a larger range of compositions that yield amorphous alloys. P_2O_5 is an ideal glass former with a high cation field strength, high oxidation state (5+) and tetrahedral coordination that forms robust open networks.[12] Although also very hygroscopic and thus unlikely practical for electronic applications, P_2O_5 is a useful host to test the fundamental network forming chemistry in comparison to Al_2O_3. Figure 3.1 (dashed lines) demonstrates that amorphous alloys can be synthesized with 50% Co or Ni in P_2O_5 while films of similar composition in the Al_2O_3 phase segregate, consistent with the above hypothesis.

Kinetic barriers to phase segregation: metal diffusion coefficients

Our data (Figure 3.1) show that cations with higher oxidation states (6+, 5+, 3+) are more stable in amorphous alumina films than those of lower oxidation states (2+).

Typical trivalent cations have activation energies of diffusion of over ~4 eV in metal oxides,[14] typical divalent metals in the range of 2 eV in metal oxides [111,112] and typical monovalent metals of 0.15 eV and higher.[114] Because the activation barrier for self-diffusion of a transition metal oxide should be related directly to the metal oxygen bond strength, the trend in activation energy may help explain the experimental observation that high-oxidation state cations are more likely to form amorphous phases.

Complex film stoichiometries.

To demonstrate the compositional flexibility of the solution chemistry platform while maintaining a single-phase dense amorphous film with "atomic" smoothness, we have fabricated four- and six-component metal oxide thin films (Figure 3.7). By selecting transition metal oxides with high oxidation states, keeping the individual TMO_x fraction low (10%) and the Al_2O_3 fraction moderate (50%), amorphous $V_{0.1}Cr_{0.1}Mn_{0.1}Fe_{0.1}Zn_{0.1}Al_{0.5}O_x$ was deposited with a 0.1 nm R_{rms}. Using TMO_x with only high oxidation states and d^0 or d^5-HS electronic configurations enabled the synthesis of the quaternary alloy $V_{0.2}Cr_{0.2}Fe_{0.2}Al_{0.4}O_x$ with a single amorphous phase and sub-angstrom roughness (R_{rms} = 0.09 nm). These were the only two complex compositions attempted. It should therefore be straightforward to synthesize a large number of other compositions for specific applications following the guiding principles outlined in the above section.

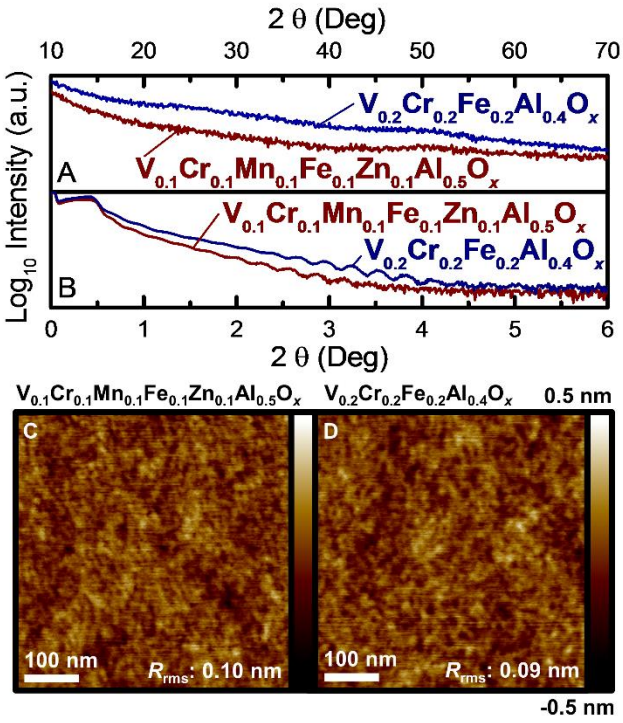

Figure 3.7. (A) GIXRD, (B) XRR and (C & D) AFM of $V_{0.1}Cr_{0.1}Mn_{0.1}Fe_{0.1}Zn_{0.1}Al_{0.5}O_x$ and $V_{0.2}Cr_{0.2}Fe_{0.2}Al_{0.4}O_x$ films deposited by spin coating and annealed at 450 °C. Note the lack of Bragg diffraction from any phase and that R_{rms} is ≤ 0.1 nm.

Conclusion and Bridge

We report the synthesis and characterization of a new family of precise, near-atomically smooth, thin-film amorphous oxide alloys. These materials are inaccessible by traditional bulk melt-quench methods and made possible here by design of aqueous precursor chemistry and chemical quenching of the amorphous state in the spin cast solution precursor film. The synthesis allows for easy composition tuning – including access to complex amorphous compositions with four and six metal oxide components – while delivering dense uniform amorphous films. We discovered significant differences in the highest amount of 3d transition metals that can be alloyed with alumina in the amorphous state. We explain the trends in amorphous-alloy stability using concepts from

glass theory, inorganic and solid state chemistry: (1) low oxygen coordination yields open networks that stabilize amorphous structure by minimizing local strains, (2) d^0, d^5-HS and d^{10} metals yield high bonding/coordination flexibility, and (3) high metal oxidation states increase activation energy for cation hopping, suggesting kinetic stabilization of the chemically quenched amorphous state. The dramatic tunability of the amorphous film composition suggests a route to systematically affect film electronic structure while maintaining exceptional film smoothness. This broad and flexible synthetic platform allows targeted design of new materials systems for a range of applications including "selective" electronic contacts and multicomponent heterogeneous catalysts.

With a thorough understanding of which films are amorphous alloys and nanoparticulate composites a further investigation into the local structure of the TM cations can be carried out. This done with x-ray absorption and optical spectroscopies in the following chapter which are both sensitive to the local coordination of TM cations (bond length, coordination number, coordination geometry).

CHAPTER IV

THE LOCAL STRUCTURE AND OPTICAL ATTENUATION OF METAL CATIONS IN AMORPHOUS THIN FILMS

Portions of this chapter include coauthored material. Co-authored material (with L. J. Enman, E. A. Cochran, E. Pledger and S. W. Boettcher). The excerpt to be included was written entirely by myself and Lisa Enman. The experimental work was performed either by me or by L. J. Enman, E. A. Cochran and E. Pledger under my, L. J. Enman's and S. W. Boettcher's direction. Myself, L. J. Enman and E. A. Cochran made samples for and collected XAS data. L. J. Enman analyzed all XAS data. E. Pledger made samples for, collected and worked up all optical absorbance data under my direction. I analyzed all optical absorbance data.

Introduction

Amorphous mixed metal oxides are of fundamental interest and in thin film form have a large application value. The amorphous phase is unique it that it has a high level of disorder (like a liquid) but can have high densities (like a solid) allowing for overlap of orbitals of appropriate energies. Additionally, the lack of thermodynamic constraints on composition (amorphous materials are generally considered to be kinetic products) allow range of compositions can be probed. The flexible structure of amorphous materials and their ability to be fabricated wth atomic smoothness makes them ideal for integration in to a range of optical and electronic devices. The ability to control the density of states in a solid is a grand challenge of chemistry and is pursued in many different ways ranging from computational approaches such as materials genome project to continued work in

tunable organic electronics. Applications in the control of the density of state of metal oxide thin films include everything from colored glasses to advanced micro and macro electronics.

We present here preliminary information on the density of states in transition metal oxide aluminum oxide alloys "$TM_yAl_{1-y}O_x$". Although transition metal colored silica glass has been extensively studied, the effect of transition metals on the density of states and "color" (i.e. optical transitions) in amorphous alumina has been minimally studied in compositional range. This is predominantly due to the inability to form bulk amorphous Al_2O_3 by standard melt quench techniques used for normal glasses.[12,13] Modern thin film deposition techniques are capable of accessing extremely fast effective quench times and can thus make amorphous Al_2O_3 quite readily. Additionally, it has recently been shown (in chapter III) that amorphous TMO_x-Al_2O_3 alloys can be readily made by the "chemical quench" of metal nitrates to metal oxides in thin film form.

Methods

Precursor Preparation

Aqueous precursors were prepared as previously described in chapter III. Briefly oligomeric Al-hydroxide clusters "f-Al_{13}" was mixed with a transition metal nitrate or chloride at the metal ratio desired in the film. All solutions were 1 molar in total metal concentration.

Thin Film Deposition

Metal oxide thin films were deposited on "quartz" fused silica slides from Technical Glass Products for optical measurements and X-ray reflectivity (XRR)

measurements. Films were deposited on (100) Si for ellipsometry measurements and XAS experiments. In all cases 1” square substrates were used. Substrates were sonicated for 5 min in a solution of 6.25% Contrad 70 (dilute basic detergent solution) to remove particulates. Spin rinsed for 10 s and spin dried for 50 s at 3000 RPM. Substrates were dried at 150 °C for 5 min. Substrates were plasma cleaned in an O2/N2 mixture for 10 min. Substrates were spin rinsed for 10 s and spin dried for 20 s. Precursor solution was deposited dropwise through a 0.2 um PTFE filter (to remove solution particulates) with one drop deposited on each quadrant of the substrate, extra drops were added as needed to completely wet the substrate. The sample was spun at 3000 RPM for 30 s the quickly moved to a hot plate at 150 °C. After 5 min at 150 °C, the sample was moved to a hotplate at 450 °C for 10 min. Samples for XAS were made extra thick to increase the X-ray fluorescent single. This was achieved by depositing 10 layers by repeating the final rinse, deposition and annealing steps 10 times.

XAS Characterization

X-ray absorption spectroscopy measurements were performed on Beamline 12-BM,B (bending magnet) of the Advanced Photon Source at Argonne National Lab. Data were collected at V, Cr, Fe, Co, Ni, Cu, and Zn K-edges. A Si(111) monochromator was used and the incoming beam was detuned 60-80% for harmonic rejection with a 1.5 mm x 0.5 mm spot size. Samples were approximately 300 nm films deposited on Si(100) substrates and were measured in air at room temperature in total fluorescence mode using a 13-element Ge detector (Canberra). The energy was calibrated by measuring the absorption at the K-edge of metallic foils of the same element in transmission mode

directly before and after each set of samples (2-5 samples). There was no change in metal edge energies after sample measurements.

Spectra were merged (between 2 and 6 scans) and normalized to edge step of 1.0 using the Athena software. Spectra were fit using Artemis software, in which theoretical standards were computed by FEFF6 of crystalline oxides (V_2O_5, Cr_2O_3, CrO_3, α-Fe_2O_3, Co_3O_4, NiO, CuO and ZnO) with crystal structures obtained from the Inorganic Crystal Structure Database (ICSD). Fits were performed over an R-space of 0.9 – 2 Å in the Fourier transform using k-ranges of 2.5 to 11 Å (V, Fe, Co, Ni, Cu, Zn) or 2.5 to 12 Å (Cr, Mn, Ga) with a Hanning window and k^2-weighting. S_0^2 values for each metal edge were calculated from fits to spectra of polycrystalline films (V_2O_5, Cr_2O_3, CrO_3, α-Fe_2O_3, Co_3O_4, NiO, CuO and ZnO) and was constrained between 0.7 and 1.0. The S_0^2 value was then used in the fits to sample spectra in order to calculate oxygen coordination around each transition metal. The number of independent points ranged from 5.3 to 6, determined by the Nyquist criterion, and the parameters E_0, ΔR, and σ^2 were also evaluated by the fits.

Thickness Characterization

The thickness of the films used for optical measurements were either measured directly with XRR of the films on quartz substrates. If the films were too rough (frequently found for compositions know to phase segregate) to yield Kiessig fringes that could be fit an identical film was deposited onto a Si substrate and the thickness was measured with ellipsometry. XRR was carried out on a Bruker D8-Discover with a Cu Kα source. Spectra were collected from 0 – 6° after sample alignment. The thickness of the sample was determined with Fourier transform fits in Rigaku's GlobalFit software.

Ellipsometry measurements were carried out on a Woollam M44 Spectroscopic Ellipsometer. Data was fit with a single Cauchy Layer to determine the thickness.

Optical Attenuation Characterization

Transmittance and reflectance measurements were collected on a Perkin Elmer Lambda-1050 UV/Vis/NIR spectrophotometer utilizing a 150 mm integrating sphere. For the wavelengths investigated deuterium and tungsten halogen light sources were used with a Si PMT. The transmittance and reflectance measurements were taken at the transmittance and reflectance ports on the integrating sphere respectively. This allowed for collection of all transmitted (or reflected) light both specular and diffuse. A Speclatron® reflectance standard was used. The optical attenuation coefficient was calculated using equation 4.1.

$$\alpha = -\frac{1}{l}\left(ln\left(\frac{T_s}{1-R_s \cdot C_r}\right) - ln\left(\frac{T_q}{1-R_q \cdot C_r}\right)\right) \qquad \text{Eq. 1.}$$

Where a (cm^{-1}) is the attenuation coefficient, l is the film thickness (cm), T_s is the transmittance of a sample, R_s is the reflectance of a sample, C_r is the reflectance correction factor, T_q is the transmittance of the quartz substrate and R_q is the reflectance of the quartz substrate.

C_r accounts for the difference in the collection efficiency of the integrating sphere as a function of the amount of reflected light that is specularly or diffusely reflected. As reported previously a C_r of 0.8 is needed when a Speclatron® reflectance standard is used with samples that are very smooth and whose reflectance is mostly specular.[115] Due to the thickness of our films ~30 nm, a calibration of the collection efficiency by tuning C_r until interference effects were eliminated in the a was not possible due to the lack of

interference fringes in our spectrum. Instead we use the C_r of 0.8 reported previously. We verified this as a reasonable factor by calculating the absorbance of our quartz substrate with and without using the correction factor. If the correction factor is not used negative non-physical absorbance values are found. This is due to the higher collection efficiency of an integrating sphere with regards to specular reflected light over diffusely reflected light. Thus the "1-*R*" term is too small resulting in absorbance that is to low (negative if in a region of the spectrum where no absorption is observed). With the correction factor applied no non-physical negative absorbances are observed.

Results and Discussion

$V_yAl_{1-y}O_x$

The $V_yAl_{1-y}O_x$ precursors used in this study consist of a V in the 4+ oxidation state. Upon drying and heating the V^{4+} oxidizes to V^{5+}, likely by nitrates internal to the gel thin film or from atmospheric O_2. The pure VO_x films show strong diffraction from the V_2O_5 phase of Shcherbinaite. XAS fitting also shows the presence of V^{5+} in all samples investigated. The presence of V^{4+} cannot be ruled out, but its concentration in the films is probably minimal.

V_2O_5 thin films show the characteristic XA spectra (figure 4.1) expected for the local environment of V in Shcherbinaite. This consists of four O ligands singly bonded to V in a near planar configuration and a fifth O ligand doubly bonded out of the "plane" of the singly bonded oxygen. The double bonded O species manifests itself with a very short bond distances of < 1.6 Å. V is not considered to make a formal bond with the sixth O that would complete the octahedra due to its extremely long bond distance of 2.8 Å. Due to puckering in the plane of the four singly bonded oxygens and the shorter V=O bond

length this local structure falls into non of the common coordination geometries despite the fact that it resembles a square pryamid geometry.

Optical absorption (Figure 4.2) due to charge transfer from the filled O2p orbitals to the various V3d orbitals results in absorption peaks at 480, 420, 375 and 275 nm. In lieu of modeling the exact d-splitting of the highly distorted square pyramid structure, the strongest absorption peaks at 420 and 275 nm can be attributed approximately to the t2 and e of a highly distorted octahedra. This gives a Δ_{oct} of 1.6 eV.

The XA and optical spectra of $V_yAl_{1-y}O_x$ films (Figure 4.1) is distinctly different than those of V_2O_5 and very similar to each other. This implies that despite the fact that $V_{0.7}Al_{0.3}O_x$ shows bragg diffraction (chapter III) the local environment of V in the crystalline $V_{0.7}Al_{0.3}O_x$ is very similar to that in the amorphous films with lower V content. It is noted that the $V_{0.7}Al_{0.3}O_x$ crystalline phase seen by diffraction does not match that of the Shcherbinaite and appears to have a layered structure. The local structure of V^{5+} in mixed metal films has a bond length intermediate to that of the double and single bonds present in V_2O_5. Furthermore, a likely decrease in coordination from the highly distorted 5 coordinate octahedra to something 4 coordinate possibly tetrahedra appears to occur. The local structure of V observed is very similar to that seen for V in crystalline $AlVO_4$. This manifests in the optical absorption data (Figure 4.2) with an increase in optical band gap. This d-splitting manifests itself between two broad peaks at 280 nm (4.4 eV) and 225 nm (5.5 eV) due to O2p → e and O2p → t_2 respectively. The contraction of the d-splitting (as expected in going from a distorted-octahedra to a tetrahedra) results in a greater distance between the O2p orbitals and the lowest V3d orbitals (t_2 in distorted-octahedra and e in tetrahedra). This pair of strong absorption

peaks has been seen for tetrahedral V^{5+} in other systems, notably tetrahedral V on $Al_2O_3/Al(OH)_3$ surfaces.[116] The broadness of the absorption peaks is likely due to the range of tetrahedral d-splitting and O2p to V3d due to variation in V-O bond distances and O-V-O bond angles in the disordered amorphous film.

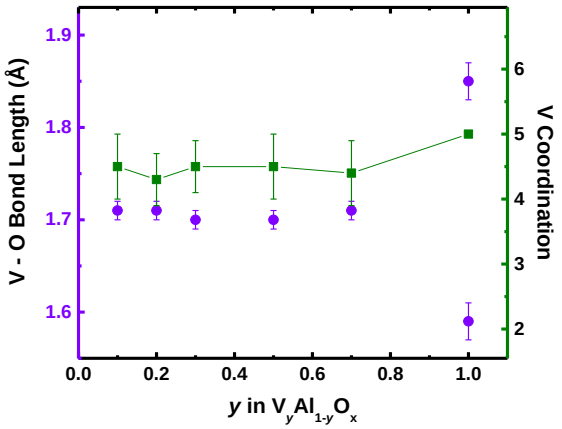

Figure 4.1. V-O bond length and V coordination fit from V XA spectra of $V_yAl_{1-y}O_x$ thin films.

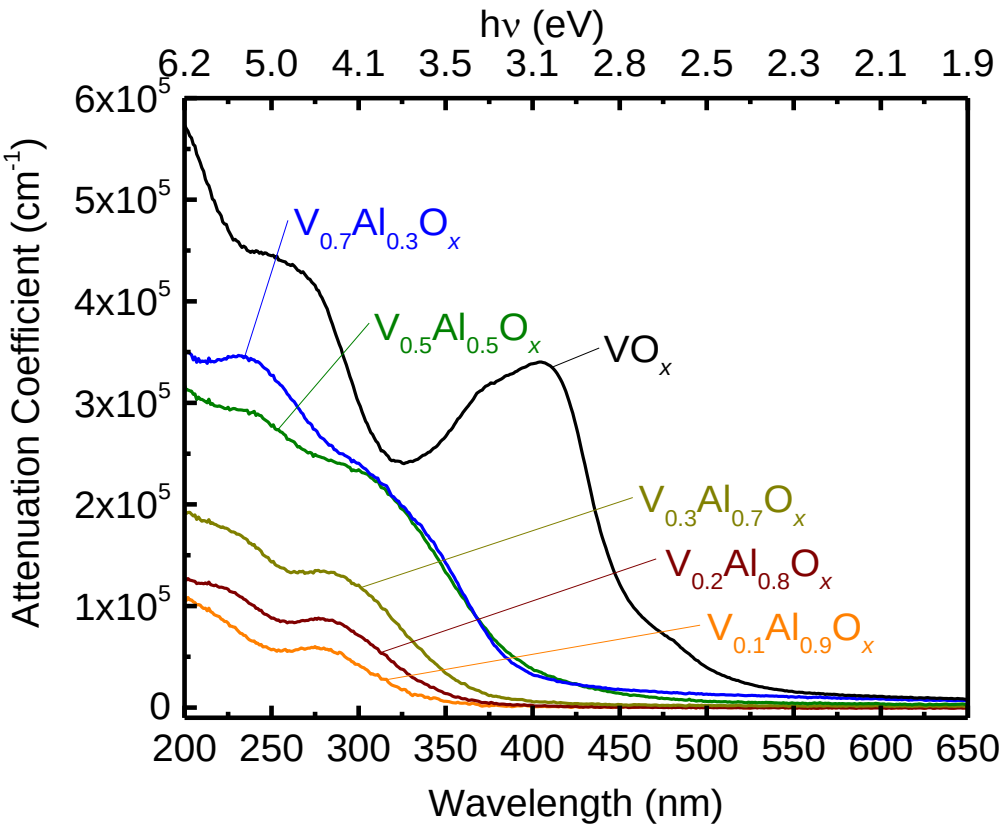

Figure 4.2. Attenuation coefficients of $V_yAl_{1-y}O_x$ thin films as a function of wavelength. Films are amorphous when $y \leq 0.5$, $V_{0.7}Al_{0.3}O_x$ and VO_x crystallize into different phases.

$Cr_yAl_{1-y}O_x$

The $Cr_yAl_{1-y}O_x$ precursor used in this study consists of Cr^{3+} and Cr crystallizes into Cr_2O_3 when $y \geq 0.7$. In this form Cr is d^3, resulting in a half full t_{2g} band and an empty e_g band. Two week absorbances in the visible in Cr_2O_3, at 610 nm and 460 nm are due to spin allowed d → d transitions, these transitions are Laporte forbidden, but only weakly so do to a lack of centrosymmetry in the distorted octahedra. Stronger absorbances are seen from 3.3-5.3 eV due to O2p → Cr3d charge transfer.

$Cr_yAl_{1-y}O_x$ films are amorphous when $y \leq 0.5$. In this compositional space a distinct change in the local environment of Cr is seen in the XA spectra. The XA spectra

can be only fit with a mixture of octahedral Cr^{3+} (approximately the same species as seen in Cr_2O_3) and tetrahedral Cr^{6+}. Cr^{6+} had been previously seen in the films by XPS and the XAS pre-edge features clearly show the presence of species lacking an inversion center (in contrast to pure Cr_2O_3 films). Figure 4.3 shows the average coordination number of Cr due to the mixture of 4 and 6 coordinate species for compositions of y = 0.2, 0.3 and 0.5. Two bond lengths are also listed for y = 0.3, 0.3, 0.5, the shorter bond length ~1.6 Å corresponds to the tetrahedral Cr^{6+} species, the longer bond ~ 1.9 Å corresponds to the octahedral Cr^{3+} environment. Notably the concentration of Cr^{3+} in the films at y = 0.1 is too small to be reliably fit.

Once Cr is oxidized to Cr^{6+}, the d^0 environment removes all d → d electron transfer. This is manifest in the reduction of the absorption intensity at 460 and 610 nm as Cr content in the films decrease. Notably shoulders from the higher energy charge transfer peaks still tail out encompassing the 460 and 610 nm transitions for y = 0.5 and y = 0.7 which both have significant concentrations of Cr^{3+}. In the amorphous $Cr_{0.5}Al_{0.5}O_x$, the d → d transition may also be broadened due to a higher degree of bond length and angle variation of the octahedral environment in the disordered amorphous structure. The absorption that is seen in the films containing a large concentration of Cr^{6+} is expectedly reminiscent of that of V^{5+} discussed previously. Two peaks at 370 and 260 nm are due to O2p to e and t_2 transitions respectively. Unfortunate for the purpose of Cr^{3+}:Cr^{6+} determination, these peaks overlap significantly with the O2p to t_{2g} and e_g transitions seen in Cr^{3+}. It is noted that the similarity in d-splitting between octahedral Cr^{3+} and tetrahedral Cr^{6+} (manifest in their respective O2p → d transitions) is not due to a fundamental relationship between the two, but rather due to similar amounts of O2p –

Cr3d orbital overlap due to the competing effects of coordination number (6 and 4) and bond length (1.9 and 1.6 Å) respectively. Higher coordination and shorter bond lengths should both lead to greater orbital overlap, hence a similar amount of orbital overlap is achieved in both cases.

It is possible that thicker films could be used to increase the sensitivity to the d → d transitions between 800 and 400 nm (with possible saturation of signal for the charge transfer optical transitions). Increased sensitivity might shed light on whether the degree of broadening of the d → d bands.

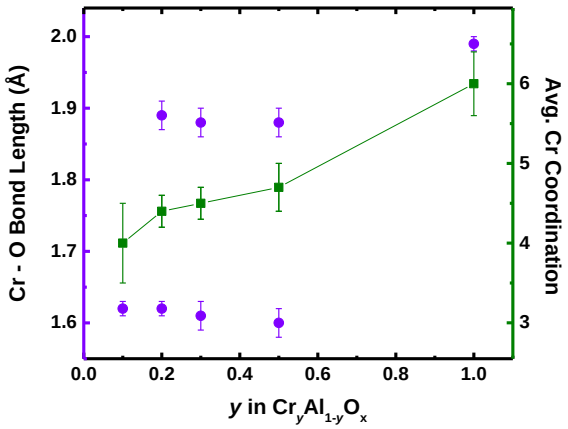

Figure 4.3. Cr-O bond length and Cr coordination fit from Cr XA spectra of $Cr_yAl_{1-y}O_x$ thin films.

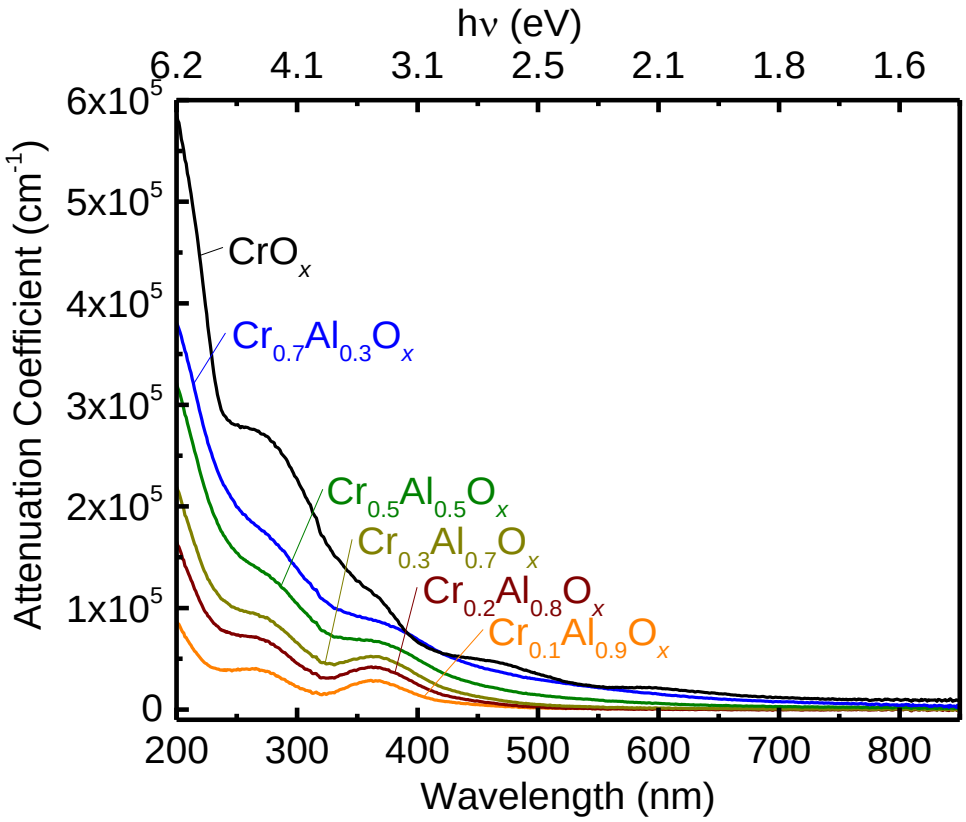

Figure 4.4. Attenuation coefficients of $Cr_yAl_{1-y}O_x$ thin films as a function of wavelength. Films are amorphous when $y \leq 0.7$.

$Fe_yAl_{1-y}O_x$

The optical absorption spectrum of α-Fe_2O_3 (hematite) is complex and dominated weakly forbidden d→d transitions by the Laporte selection rule and strongly forbidden spin selection rule (due to its d^5 highspin occupation) resulting in "spin-flip transitions" at energies higher than a strict d→d transition. Interestingly the XAS derived local structure of Fe^{3+} in a-Al_2O_3 is substantially different than the distorted octahedra found in α-Fe_2O_3. It appears to mimic the local structure of Al^{3+} in amorphous Al_2O_3 (as seen in Figure 2.3) with an average coordination of 4.5 and an Fe-O bond distance reminiscent of the shortest bond distance in α-Fe_2O_3.

In the optical absorbance (Figure 4.6) data this results in a shift of the absorption processes to higher energies in what is probably described by the turn on of a high energy charge transfer peak at 275 nm with a preceding shoulder at 368 nm.[117] The significant absorption tail in the $Fe_{0.7}Al_{0.3}O_x$ sample may be due to presence of some 5 or 6 coordinate Fe^{3+} as seen in the XA spectra.

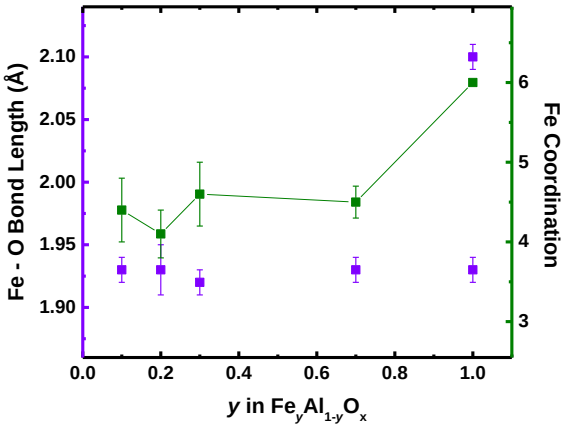

Figure 4.5. Fe-O bond length and Fe coordination fit from Fe XA spectra of $Fe_yAl_{1-y}O_x$ thin films.

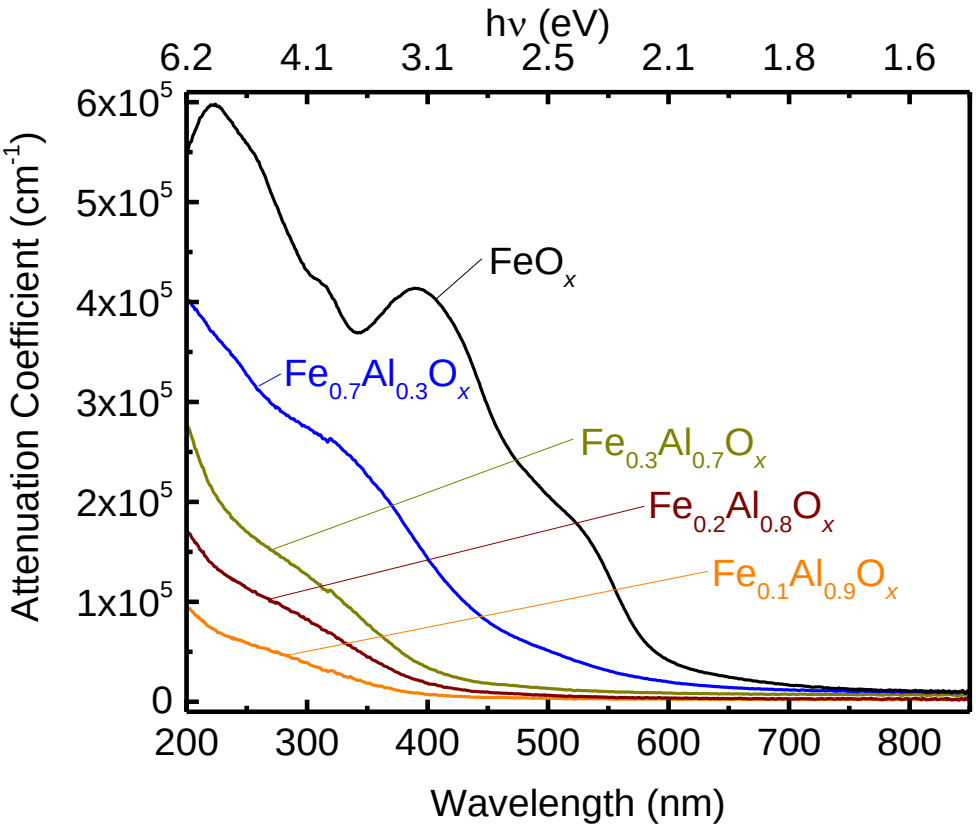

Figure 4.6. Attenuation coefficients of $Fe_yAl_{1-y}O_x$ thin films as a function of wavelength. Films are amorphous when $y \leq 0.9$.

$Zn_yAl_{1-y}O_x$

ZnO absorbs UV light via the excitation of an electron from the valence band to the conduction band. The edge of the valence band is dominated by contributions from full O2p orbitals. The edge of the conduction band is dominated by contributions from empty Zn4s orbitals. The Zn4s orbitals are large enough to overlap, resulting in true band formation and consequent stabilization and lowering of the Zn4s energy level. This overlap also results in the delocalization of electrons in the ZnO conduction band. This manifests in the high mobility achieved in crystalline and amorphous ZnO compared to other first row metal oxides. The bandgap of ZnO is optically present (Figure 4.13) in

samples shown to be composites of c-ZnO & a-Al_2O_3 (chapter III) including ZnO, $Zn_{0.7}Al_{0.3}O_x$ and $Zn_{0.5}Al_{0.5}O_x$. This optical transition is lost and replaced with a higher energy transition despite the lack of any statistical difference in Zn^{2+} coordination environment as measured by XAS (Figure 4.14). Although the fact that Zn^{2+} remains tetrahedrally coordinated by O with a bond distance of 1.97 Å while in an a-Al_2O_3 matrix is interesting in its own right it is not surprising that change in optical properties is not correlated with a change in the local coordination of Zn^{2+}. It appears that at the maximum concentration at which ZnO maintains an amorphous alloy with Al_2O_3 (40%) the concentration of Zn4s orbitals is not high enough to maintain delocalization and energetic stabilization of the low energy conduction band. It is presumed that due to ZnO being dilute in Al_2O_3 the concentration of O2p orbitals is essentially constant with regard to composition and that all changes in the optical transition are due to changes in the location of the Zn4s orbitals. The optical transition that initiates at ~250 nm is thus likely representative of the energy of charge transfer from an O2p orbital to an isolated Zn^{2+} cation or a cluster of a few Zn^{2+} cations in orbital contact with each other. The trend in increasing energy of the charge transfer process with decreasing Zn concentration makes since fi one considers a decreasing liklihood of few atom ZnO clusters with decreasing Zn concentration. It is also possible that in the armophous system Zn 4s orbitals are delocalizing with the higher energy Al 3s orbitals and lowering the (now) mixed 3s-4s band. This also correlates with the shift in apparent band gap of the a-$Zn_yAl_{1-y}O_x$ films. Ongoing work is looking at the O2p to Zn 4s transition in $Zn_yP_{1-y}O_x$. This system is of interest as ZnO should remain amorphous with P_2O_5 to much higher concentrations as seen for Co_3O_4 and NiO in (chapter III) which may allow for the concentration of Zn

which is necessary to delocalize the Zn4s orbitals to be determined in a solid state system lacking any other orbitals which can delocalize with those of Zn.

Additionally, we note that the strong optical transition at 250 nm which is present in the amorphous materials weakens with decreasing ZnO concentration. This implies that this is not an accidental measurement of the pure a-Al_2O_3 band gap (O2p to Al3s transition), see Figure 4.15. Furthermore, the strong increase in attenuation coefficient that turns on at 250 nm is not present in the pure c-ZnO film, but is present in films known to contain ZnO crystallites, $Zn_{0.7}Al_{0.3}O_x$ and $Zn_{0.5}Al_{0.5}O_x$. This implies that even though these two compositions, and likely any compositions spanned by these two, show the presence of ZnO crystallites the amorphous Al_2O_3 phase present in the films still has a substantial concentration of Zn present, perhaps even "saturated" near the concentration of Zn required to nucleate crystallites. This implies that when $0.5 \leq y < 1$ the film might actually be a composite of c-ZnO and a-$Zn_{0.4}AlO_{0.6}O_x$ (the highest concentration of Zn known to remain amorphous in alumina).

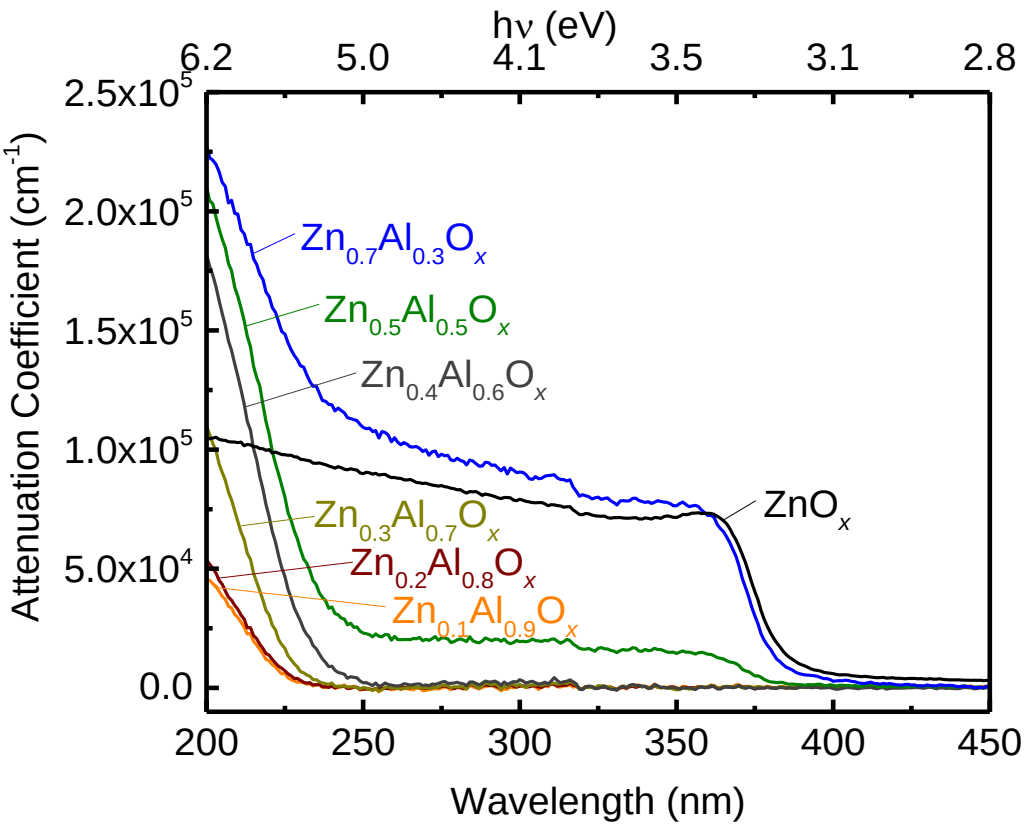

Figure 4.13. Attenuation coefficients of $Zn_yAl_{1-y}O_x$ thin films as a function of wavelength. Films are amorphous when $y \leq 0.4$.

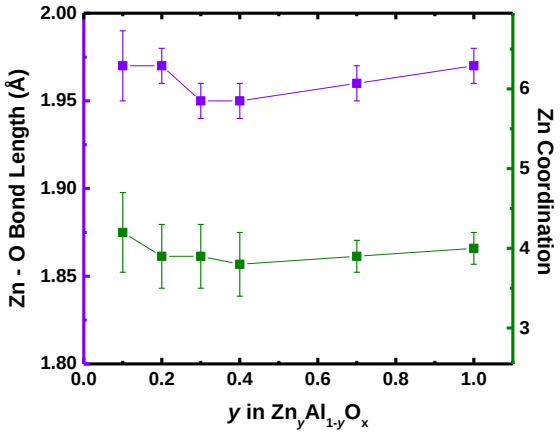

Figure 4.14. Zn-O bond length and Zn coordination fit from Zn XA spectra of $Zn_yAl_{1-y}O_x$ thin films.

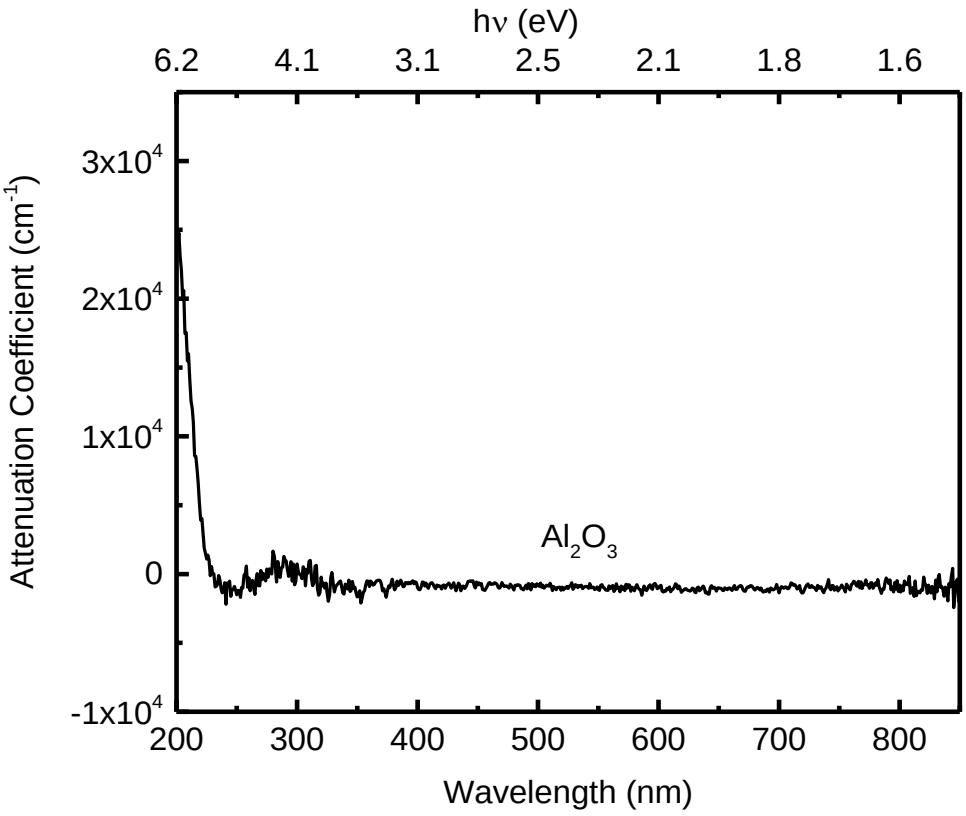

Figure 4.15. Attentuation coefficient of a-Al_2O_3 film.

Conclusion and Bridge

In sum, the local structure of TM cations has been investigated in amorphous alloy of a transition metal oxide and aluminum oxide in thin film form. TM cations that are four coordinate in their crystalline state (ZnO) stay four coordinate in the amorphous state. TM cations that are 5 (V_2O_5) or 6 coordinate (Cr_2O_3, Fe_2O_3) show a decrease in average coordination number to a value of about four in the amorphous state. The thin nature of the films ~30 nm, allows for direct measurement of the strong charge transfer bands which are often difficult to see (due to very high attenuation coefficients) in bulk glasses (~1 mm thick). Unfortunately, the thinness of the films makes it difficult to resolve the weaker d → d transitions in all but the high concentrations of TM.

The optical transitions identified confirm coordination numbers measured with XAS and in some cases give further coordination geometry information. The optical absorbance data also shows the localization of the Zn4s orbital in the amorphous state, presumably due to the Zn4s concentration being below the percolation threshold preventing delocalization. The optical data additionally gives some information regarding the position of the transition metal 3d based conduction band positions if the O2p based valence bands are considered to be fairly fixed in position. Future work will determine the location of the O2p bands with valence X-ray photoelectron spectroscopy.

We have shown that amorphous alloys can be prepared which show optical absorption and local coordination geometries substantially different than their individual constituents. However, in some cases, it is desirable to maintain the properties of two individual constituents. When this is the case a bilayer approach, composing of two independent layers is more effective as each layer maintains its bulk properties but the interfaces between two materials can be broken into three interfaces allowing for each interface to be engineered separately. This does require that the interface internal to the bilayer is does not yield unwanted effects. We investigate this approach while making optimized protective coating (which must be chemically stable, optically transparent and have a low resistance to electron transport) for a photocathode in the following chapter.

CHAPTER V

SOLUTION-DEPOSITED F:SnO_2/TiO_2 AS A BASE-STABLE PROTECTIVE LAYER AND ANTIREFLECTIVE COATING FOR MICROTEXTURED BURIED-JUNCTION H_2-EVOLVING Si PHOTOCATHODES

Portions of this chapter were previously published as Kast, M. G.; Enman, L. J.; Gurnon, N. J.; Nadarajah, A.; Boettcher, S. W. Solution-Deposited F:SnO_2/TiO_2 as a Base-Stable Protective Layer and Antireflective Coating for Microtextured Buried-Junction H_2-evolving Si Photocathodes. *ACS Applied Materials and Interfaces* 2014, 6, 22830-22837. The experimental work was performed either by me or by L. J. Enman, N. J. Gurnon and A. Nadarajah under my and S. W. Boettcher's direction. S. W. Boettcher provided editorial assistance.

Introduction

Proposed tandem water-splitting devices utilize photocathodes and photoanodes in direct contact with the electrolyte, which offer higher efficiency than single-junction devices because the individual junctions can each have smaller band-gaps and thus higher photocurrents in sunlight while still providing, in combination, the voltage needed to drive the thermodynamics and kinetics of water splitting (~1.6-1.8 V).[119] Chemically protecting semiconductor absorbers with good optoelectronic properties is important to enable high efficiency and

long-term stability. Basic media is promising for scalable tandem photoelectrochemical water splitting because the oxygen evolution reaction (OER) catalysts with the highest activity, which are also earth abundant, are only stable under basic conditions (e.g. $Ni_xFe_{1-x}OOH$ and variants).[120–124] No known earth-abundant OER catalysts are stable in acid.[121] Use of neutral pH is challenging due to slow buffer-ion transport.[125] This suggests that the hydrogen evolution reaction also be carried out in base.

Si is a promising small-band-gap material for a tandem device.[119,126] Unfortunately Si and most other small (~1 eV) band gap absorbers are unstable and soluble in base, thus protective layers are needed.[127] Significant work has focused on the photoelectrochemical properties of unprotected and protected Si photoelectrodes in acid with Pt catalysts.[128–140] The protective layers have consisted of TiO_2[141–143], $F:SnO_2$[144] and thin SiO_2[145]. Recent work has also shown the use of MnO_x[146], NiO_x[147], CoO_x[148], Ir[149] and C- or N-doped TiO_2[150] as a protective coating on Si under OER conditions. Due to the range of oxidation states of Mn, Ni and Co it is unclear if these films would be stable to reduction at the cathodic hydrogen evolution reaction (HER) potentials, thus these oxides are unlikely to be useful for the protection of photocathodes. Metallic protective coatings are not ideal due to parasitic light absorption. Oxide protective layers are usually deposited by sputtering[142,149] or atomic layer deposition (ALD)[134,135,141,146,150] and may be difficult and/or costly to scale. In summary, the ideal protective coating would be deposited inexpensively, transparent, thermodynamically stable and of earth-abundant composition.

Here we use commercial Si solar cells as a test platform for studying solution-deposited protective coatings. By using a single commercial cell there is good consistency between the solid-state junction of all of the devices fabricated, which allows for a better understanding of the effect of the protective coating on the operation of the device. This also enabled the solid-state characteristics to be compared to the photoelectrochemical characteristics of different devices in acid and base. By controlling the thickness of the oxide protection layer we demonstrate near-optimal anti-reflection properties on the textured Si surface and thus very high one-sun photocurrents near 35 mA cm^{-2} in some devices. We show that solution-deposited TiO_2 on solution-deposited F:SnO_2 makes ohmic contact to Si while preventing its corrosion in base for 24 h. Ir, being the highest activity HER catalyst in base, is used to demonstrate cells with photocathode efficiencies of up to 10.9%, which appears to be a new record.[151]

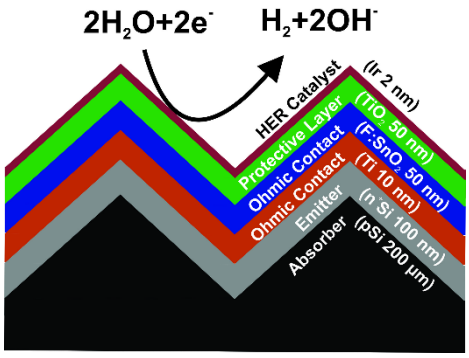

Figure 5.1. Schematic of protected textured cells with catalyst and interface layers. The role of each layer in electrode function and surface protection is discussed in the text and compared with control electrodes with different surface layers.

Methods

Electrode fabrication

Modified solar cells lacking top contacts, and in some cases lacking anti-reflective (AR) coatings, with phosphorous-rich glass or thermally grown SiO_2 in place of the AR coating) were a gift from Solar World. The solar cells had a p-type base (absorber) with a thin n^+ phosphorous-doped emitter (~100 nm in thickness) and had pyramidal surface texture 0.5-2 μm in depth. SiN_x AR coatings, if present, were removed by a 3 h etch in 48% HF. Phosphorous-rich glass was removed with 10-15 min etch in 48% HF. SiO_2 was removed with a 2-10 min etch in 20:1 BOE. Control electrodes on n^+ or p^+-Si were fabricated by making ohmic contact to the back of the Si with InGa eutectic and silver paint. Buried junction electrodes were fabricated by using silver paint to connect Sn-Cu wire to the Al back contact of the cell. Epoxy and glass tubing was used to isolate all but the Pt or Ir surface from the solution. All electrodes were ~ 0.5 cm x 0.5 cm.

Protective layer fabrication

F:SnO_2 was deposited via spray pyrolysis of 0.45 M dibutyl tin dichloride and 0.05 M ammonium fluoride in 95% ethanol 5% water.[152] A sample was placed on a hotplate with a surface temperature of 400 ºC and allowed 1 min to come to temperature. A ring stand was used to hold an airbrush (Aztec A220 Broad Stroke) at a constant angle and distance from the sample. Two 1 s bursts were sprayed every 15 s, samples were rotated $^1/_4$ of a turn every minute, with a second set of rotations starting $^1/_8$ of a turn off the first set. Deposition for 8 min yielded 50-70 nm of F:SnO_2 on a planar substrate as measured by ellipsometry. TiO_2 was deposited via spray pyrolysis of 0.05 M titanium n-butoxide and 0.1 M

acetylacetonate in ethanol using the same procedure.[153] Deposition for 12 min yielded 50-70 nm of TiO_2 on a planar substrate as measured by ellipsometry.

Metallic interface layer and catalyst deposition

Ti, Ir and Pt were evaporated via e-beam in an Angstrom Engineering Amod physical vapor deposition system. Catalyst control films of Pt and Ir were fabricated by depositing 50 nm of Pt or Ir onto 25 nm of Ti previously deposited onto a piranha (3:1 conc. aq. H_2SO_4 : 30% aq. H_2O_2) and O_2 plasma (150 W for 5 min) treated glass microscope slides. Thin catalyst controls were made by depositing 2 nm of Ir onto clean Au/Ti coated glass slides. Silver paint was used to connect a Sn-Cu wire to the top surface and encased in epoxy. All photocathodes utilize 2 nm thick Ir/IrOx catalyst layers. A cross section of the photoelectrodes is depicted in Fig. 5.1, after deposition of the protective coatings and the catalyst layer.

Electrochemical measurements

(Photo)electrochemical experiments were carried out with the fabricated working (photo)electrode, a Pt counter electrode (in a separate compartment behind a high porosity plastic frit) and a Hg/HgO reference electrode. The electrolyte was 0.1 M UltraPure (Fluke Analytical TraceSelect,"UP") KOH, 1 M UP KOH or 1 M SemiGrade (Sigma Aldrich Semiconductor Grade 99.99%) KOH. High-purity H_2 gas was bubbled through the solution to maintain a constant dissolved H_2 concentration, and thus solution potential, during the measurements. $Ni(OH)_2$ deposition on Ir and Pt was from a 2 mM $NiCl_2$ solution with a carbon

mesh counter electrode and a standard calomel reference electrode. Cleaning of the electrodes by cycling in acid was carried out in 1 M $HClO_4$ (Fluka TraceSelect).

Reflectivity measurements

Reflectivity measurements were performed on a Perkin-Elmer Lambda-1050 UV/Vis/NIR spectrophotometer utilizing deuterium (short wavelengths) and tungsten halogen (long wavelengths) light sources. An integrating sphere was used to collect the specular and diffuse reflectance at 1 nm intervals utilizing Si PMT (shorter wavelengths) and InGaAs (longer wavelengths) detectors. A 1.8 mm thick sheet of soft glass was mounted on the UV/Vis/NIR instrument, samples were covered in water and quickly placed against the glass where they were held by surface tension and tape during the measurement, as is illustrated in Fig. 5.8.

Physical characterization

Scanning electron microscopy images were taken on a Zeiss Ultra-55 at 5 keV with an in-lens detector. X-ray photoelectron spectra were collected on a Thermo Scientific ESCALAB 250 using a monochromated Al kα source. Ellipsometry measurements were taken on a Woollam M44 spectroscopic ellipsometer using 400 to 700 nm wavelength light. X-ray diffraction measurements were taken on a Rigaku SmartLab with parallel beam optics, in a θ-2θ geometry with a Cu kα source.

Results and Discussion

An ideal H_2-evolving photocathode could consist of a stable, high-efficiency buried junction electrically coupled to a high-activity catalyst. The

protective coating should be thermodynamically stable in base, completely lack pinholes or other defects, have a low resistance to electron transport, be optically transparent and have its thickness and index of refraction tuned for anti-reflection properties. Furthermore, for scalability, low-cost high-throughput methods are needed for deposition of the protective coating. The use of ALD for example, which is known to deposit at 100-300 nm hr^{-1}, for thick film deposition could be difficult to scale.[134,150,154]

Semiconducting absorber characterization

A commercial n^+-emitter/p-base Si solar cell with a pyramidal textured surface was used to provide a consistent and efficient buried junction. Figure 5.2 shows the current density - potential (JV) characteristics of a full cell (15.5 cm × 15.5 cm), a 0.5 cm × 0.5 cm diced cell and a photocathode consisting of a 0.5 cm × 0.5 cm diced cell with all contacts and AR coating etched off and a 2 nm layer of Pt in acid (0.5 M H_2SO_4) evolving H_2. The V_{oc} (580 mV) is reduced in the diced cell compared to the full cell (618 mV), which we attribute to increased recombination at the cleaved edges. The fill factor of the full cell is reduced due to the contact resistance of the measurement leads. The V_{oc} of the Pt-containing photocathode (574 mV vs. the reversible hydrogen electrode, RHE) is identical to that of the diced solid-state cell within sample-to-sample variability. The fill factor of the photocathode (58%) is reduced slightly compared to the diced solid-state cell (68%) due to the kinetic and mass-transport overpotentials of hydrogen evolution in acid on Pt. We note the photocathode efficiency of this cell for H_2-evolution is ~10.6%, higher than the previously reported 9.6% average for planar

Pt-n^+p-Si.[128] This is only 1% less efficient than the solid-state diced cell (11.6%) due to a smaller fill factor caused by driving the electrochemical reaction. Improvements in edge passivation of the small devices used would be expected to significantly improve performance.

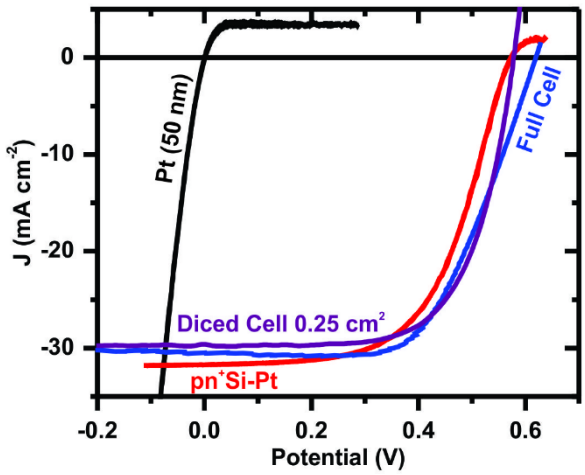

Figure 5.2. Comparison of JV curves from the full solid-state cell (15.5 cm × 15.5 cm), diced solid-state cell and diced cell with Pt catalyst added evolving hydrogen in the 0.5 M H_2SO_4 electrochemical cell (voltage referenced to RHE for electrochemical measurements). At Pt control electrode (black) is shown to indicate the origin of the loss in fill factor between the electrochemical (red) and solid state (purple) measurements.

Solution-deposition of protective coatings

Protective coatings were deposited from solution by spin casting from an aqueous Sn(II) nitrate precursor[155] and by spray pyrolysis of tin butyl chloride and titanium isobutoxide precursors.[152,153] Spin casting proved to be inappropriate due to the surface wetting properties of textured substrates resulting in deposition primarily in the valleys and not on the peaks of the textured surface (Fig. 5.3A). Spray pyrolysis of F:SnO_2 and TiO_2 precursors yielded dense conformal coatings (Fig. 5.3B) and was used for all other oxide depositions**.** This is likely because the

precursor decomposes immediately to form dense crystalline oxide on the heated substrate surface during spray pyrolysis.

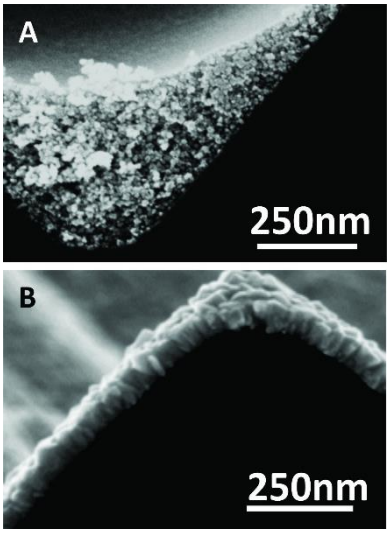

Figure 5.3. SEMs of F:SnO_2 deposited via spin casting (A) and spray pyrolysis.

Catalyst selection and thin film properties

To maximize the efficiency of a photoelectrode the overpotential of the reaction at the catalyst must be minimized at the same time as the optical absorption of the catalyst is minimized.[156] We measured the activity of Pt films in acid (0.5 M TraceSelect H_2SO_4) and base (0.1 M ultrapure KOH) and compared it to the activity of Ir, IrO_x, and $Ni(OH)_2$-modified Pt and IrO_x films. We prepared IrO_x by cycling an Ir film at anodic potentials (0 to 0.7 V vs. Hg/HgO) at 20 mV s^{-1} for 3 cycles. Subarraman et. al. showed that $Ni(OH)_2$ islands on Pt and Ir bulk metal electrodes increase the HER activity in base by affecting the rate-determining step of water adsorption to the catalyst surface.[157,38] We found that Ir with $Ni(OH)_2$ islands or IrO_x had the best activity for HER in base. This agrees with the work of Subarraman et. al. on bulk metal electrodes with the caveat that the Ir likely oxidized during that anodic $Ni(OH)_2$ deposition. The high activity of

$Ni(OH)_2$-Ir is thus perhaps due to IrO_x and not due to the effect of the $Ni(OH)_2$ islands as previously assumed.[158] Although IrO_x is not thermodynamically stable to reduction under HER conditions in base, previous work has shown IrO_x to have significant kinetic stability.[159] Electrodes were also tested in a solution of 0.1 M KOH containing 0.01 M LiOH. Although 0.01 M LiOH had a significant effect on the activity of Pt (and its $Ni(OH)_2$ analogue) its effect on the activity of IrO_x was small (Fig. 5.4).

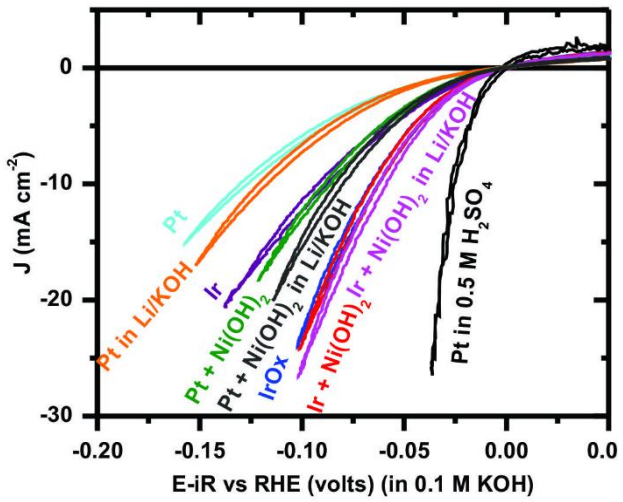

Figure 5.4. Voltammograms of HER catalysts (Pt, Pt-$Ni(OH)_2$, Pt-Li^+, Pt-$Ni(OH)_2$-Li^+, Ir, Ir-$Ni(OH)_2$, IrO_x, Ir-$Ni(OH)_2$-Li^+) in 0.1 M KOH contrasted to Pt in 0.5 M H_2SO_4. Electrodes consist of 50 nm of Pt or Ir on 25 nm of Ti on glass. $Ni(OH)_2$ islands range from 1-25 monolayer-equivalents in thickness. Scans were taken at 20 mV s^{-1}. The overpotentials of the different catalysts at 15 mA cm^{-2} are tabulated in Fig. AD11.

Interfacial Si-oxide-catalyst charge transport

To achieve high efficiencies in the full H_2-evolving photocathode, low-resistance charge transport is needed from the n^+-Si emitter in the photovoltaic junction to the catalyst through the protective layer.[135] Due to the reactivity of Si, we found that the surface oxidizes during either spin casting (and annealing) or spray pyrolysis. The interfacial SiO_2 led to higher series resistance, which lowered

the fill factor for photocathodes operating in base (e.g. see red curve Si-TiO_2-Ir in Fig. 5.5).

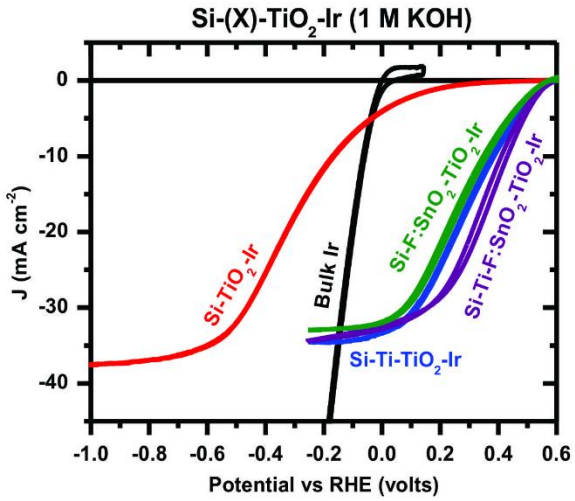

Figure 5.5. Voltammograms of different protective layer stacks showing the need for a Ti interface layer between TiO2 and Si to maintain reasonably high fill factor.

The series resistance can be lowered by using F:SnO_2 to make the initial contact to the n^+-Si (e.g. see green curve Si-F:SnO_2-TiO_2-Ir in Fig. 5.5) which is then further coated with TiO_2, needed for stability (see below). This is likely due to the higher carrier concentration in F:SnO_2 which increases tunnelling currents across the SiO_2 interfacial layer and allows the current to spread laterally and flow through locally thin SiO_2 regions. To further lower series resistance we deposited a thin layer of Ti (~10 nm thick) onto H-terminated Si prior to oxide deposition, as has been previously done by Seger et. al.[133–135,142] The Ti is partially oxidized in air and further oxidized during spray pyrolysis or spin casting. This results in a Si(pn^+)-Ti-TiO_2 interface between the n^+-Si emitter and the protective layer(s). Due to the work function alignment of Ti and n^+-Si, and small band offset between the conduction band of TiO_2 and the conduction band of Si, this interface results in low resistance of electron transport to the protective layer.[134,142] Further solution-

deposition of F:SnO_2 and TiO_2 protection layers maintains a reasonably good fill factor and provides good chemical protection, as discussed below.

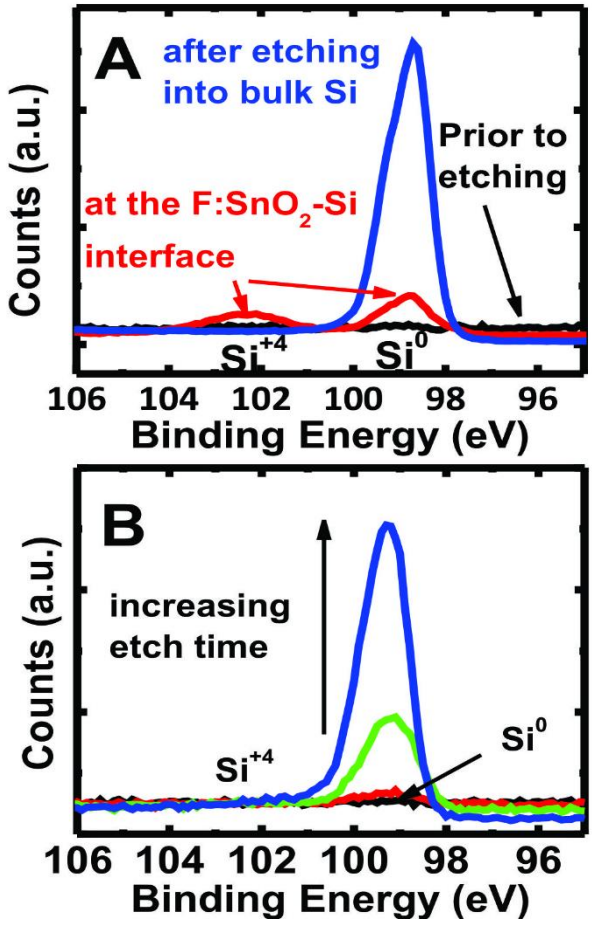

Figure 5.6. Depth profiled XPS of F:SnO2−Ti−Si stacks. (A) Oxidized Si underneath a 5 nm thick layer of Ti. (B) No oxidized Si under 10 nm of Ti. XPS data showing the presence of metallic Ti at the Si surface is shown in Figure AD9 in the Supporting Information.

were performed on F:SnO_2-coated planar Si control samples with 5 nm and 10 nm of Ti at the interface. Samples with only 5 nm (Fig. 5.6A) of Ti show the formation of interfacial SiO_2 while samples with 10 nm (Fig. 5.6B) of Ti show no interfacial SiO_2. XPS measurements also show metallic Ti^0 at the Ti-Si interface in the case of the 10 nm Ti film (Fig AD9). Direct electrical measurements were taken on planar n^+-Si samples with F:SnO_2 deposited on top of no Ti, 5 nm of Ti and 10 nm of Ti, using an Al top

contact. Significant contact resistance is seen when no or only 5 nm of Ti is present (Fig. 5.7). Upon comparing the photocathodes with identical solid-state junctions and identical catalyst layers it is also apparent that the Si(pn^+)-TiO_2-Ir sample (no Ti interlayer) had significant resistive losses (Fig. 5.5).

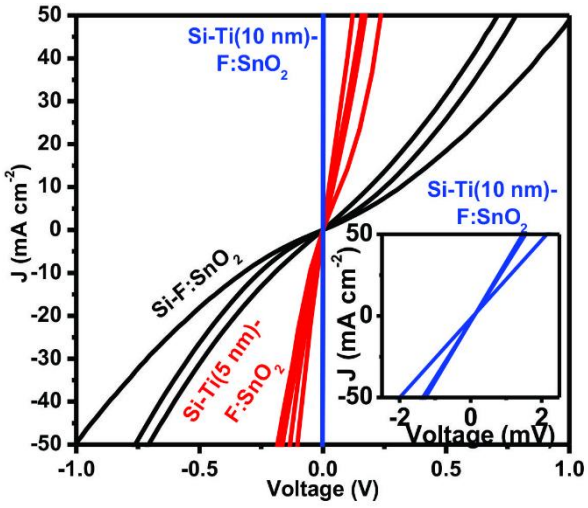

Figure 5.7. Comparison of solid state JV behavior of n^+Si-F:SnO_2-Al stacks with and without 5 and 10 nm of Ti in between the F:SnO_2 and Si. Curves of the same color represent different devices with nominally identical layer thicknesses.

Optical anti-reflection properties of protective layer coatings

To maximize the J_{sc} and thus efficiency of a photocathode the optical losses must be minimized. This includes not only the reflectivity and optical absorption of the catalyst as mentioned before but also the reflectivity of the device as a whole. To minimize the total device reflectivity a commercial textured (100) Si cell was used, resulting in increased light trapping due to an increased number of photon-substrate interactions. Furthermore, the effect of the TiO_2 protective layer thickness on the reflectivity of the device in water was probed (Fig. 5.8) as well as the effect of the presence of the different layers (Ti, F:SnO_2, TiO_2 and Ir). We note

that the index of refraction of water is different than air (1.33 vs. 1) and that the absorption of water slightly alters the AM1.5 spectrum.[160]

All thicknesses of TiO_2 studied reduced the reflectivity of the sample across the majority of wavelengths. We find that for a textured Si-TiO_2 test architecture, 40 nm of TiO_2 provides near optimal anti-reflection properties when measured under a glass plate in water to mimic the cell architecture (Fig 5.8), consistent with simulations (see Fig. AD1). We note that the measured reflectivity of the AR-coated textured samples in the visible region from 400-1000 nm (4.4-5.2%) is near that of the glass-air interface of the cell (~4%). The protective Ti/F:SnO_2/TiO_2 multilayers are more complicated to model as variation of the Ti, F:SnO_2, TiO_2 and Ir layers all effect the reflectivity of the sample due to the slight differences in the index of refraction in the F:SnO_2 and TiO_2 and the reflectivity and absorption of remaining metallic Ti. We note that the 2 nm Ir layer has almost no effect on the reflectivity of the samples (Fig. 5.8) and that the Ti interface layer in the Ti-F:SnO_2-TiO_2 samples increase the reflectivity at 500 nm from 10% to 15%. Some of the Ti oxidizes in air upon placement on the hotplate during spray deposition of the oxide layers. The fabricated photoelectrodes with the Ti/F:SnO_2/TiO_2 protective coatings typically had larger total thickness (~110 nm) in order to improve durability. The 110 nm thick TiO_2 control films, however, only show an average reflectivity of only ~1% larger than the 40 nm thick films.

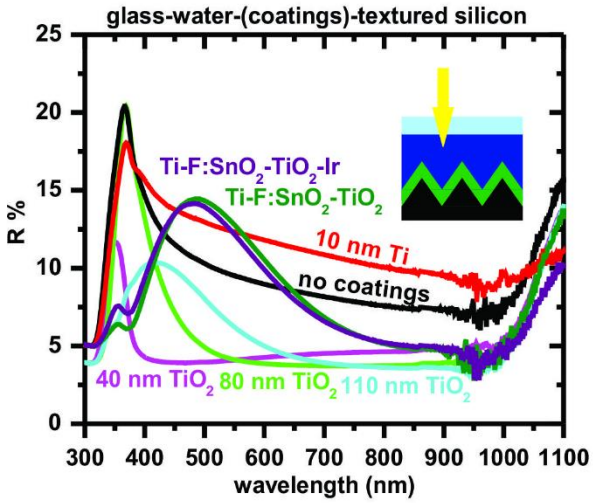

Figure 5.8. Reflectivity (percent) of textured silicon with 40, 80 and 110 nm of spray-deposited TiO_2 under water behind a glass slide. The minimum reflectivity is limited by the glass-air interface of the measurement cell (inset). Also, reflectivity of textured cells with Ti, F:SnO_2-TiO_2, Ti-F:SnO_2-TiO_2 and Ti-F:SnO_2-TiO_2-Ir also taken under water behind glass as depicted. Ti layers are 10 nm thick, F:SnO_2 layers are 70 nm thick, TiO_2 layers are 50 nm thick (in multilayer stacks) and Ir layer is 2 nm thick. The minimum reflectivity is set by the outermost glass−air interface of ~4%.

Champion device design

The champion device architecture achieved high photocurrents by utilizing a combined thickness of TiO_2 and F:SnO_2 (~100 nm) which provided good antireflection properties, and the minimum amount of Ti needed to prevent oxidation at the Si/metal-oxide interface. To minimize interfacial resistance, 10 nm of Ti, 40 nm of F:SnO_2, and 60 nm TiO_2 were sequentially deposited. IrO_x, which had the highest HER activity among the thin-films tested, was used as a catalyst to minimize losses due to kinetic overpotentials. The minimization of interfacial resistance and kinetic overpotential provides for good fill factors in the final device. The champion photocathode, operating in base, had an efficiency of 10.9% (Fig. 5.9). Other devices of similar design made in a separate batch had efficiencies of 8.9 ± 0.7% (Fig. AD2). We note the relatively high variation

between samples that are nominally identical. This is due to variation in J_{SC} and fill factor. J_{SC} depends on the reflectivity and absorption and thus on the thickness of the Ti, F:SnO_2, TiO_2 and Ir/IrO_x layers as well as the degree of oxidation of the Ti layer. The fill factor is particularly sensitive to oxidation of the Si to form a resistive SiO_2 interlayer (see Fig. 5.7).

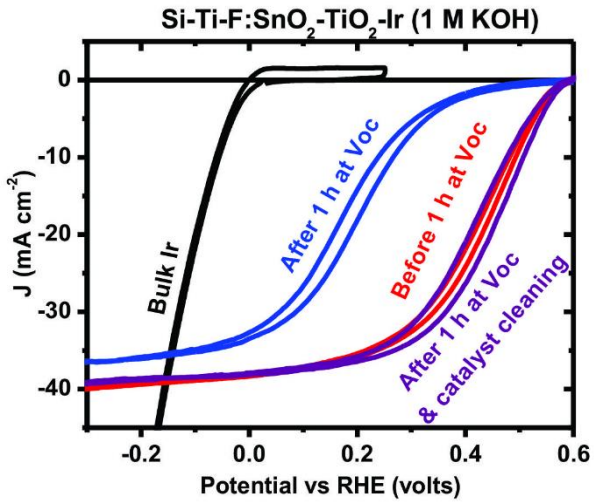

Figure 5.9. Voltamograms of Ti-F:SnO_2-TiO_2 protected silicon photocathodes under AM1.5 illumination.

Failure mode analysis

For a photocathode to maintain high efficiency for long periods of time the catalyst and absorber must both stay operational and in electrical contact. Possible failure modes include: dissolution of the catalyst, contamination/poisoning of the catalyst, dissolution of the protective layer (loss of contact between absorber and catalyst and eventual dissolution of buried junction), dissolution of the buried junction through pin holes in the protective layer, and oxidation of the buried junction resulting in high resistive losses. Here we analyse the various failure modes observed for the photoelectrode architecture developed.

After holding the champion protected Si device, Si(pn^+)-Ti-F:SnO_2-TiO_2-Ir, at open circuit for 1 hr in base the fill factor was reduced significantly. Upon cleaning the catalyst by cycling to oxidizing potentials in 1 M $HClO_4$ the voltammogram was nearly identical to the first voltammogram (Fig. 5.9). Thus it is likely that the catalyst was poisoned by the reduction of transition metal impurities from the electrolyte while sitting at the cathodic V_{oc} and the reduced fill factor is due to an increased catalytic overpotential that is alleviated upon cleaning.[161]

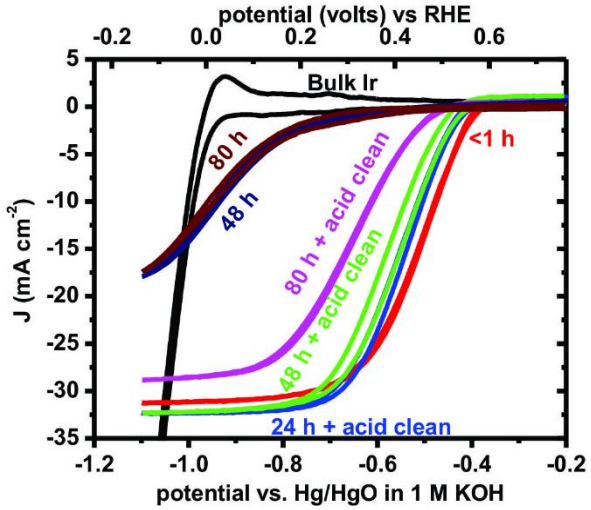

Figure 5.10. Voltammograms of photocathode after various times and treatments of stability testing. Stability testing was carried out at constant potential (300 mV positive of RHE) for various times. The photocathode was then cleaned in acid (1 M $HClO_4$) via cycling from reducing to oxidizing potentials.

Further stability testing of the champion device architecture was performed by holding near the maximum power point under illumination. After the initial 48 h, the V_{oc} decreased slightly and the fill factor decreased significantly. Upon cycling in acid (to remove metal surface contaminants, e.g. Fe, Cu, Pb, which were found via XPS analysis, see Fig. AD12) the fill factor returned to near that of the initial sweep while the V_{oc} remained slightly less than that of the initial sweep,

showing that either catalyst dissolution or damage to the buried junction had occurred (Fig. 5.10). A plot of the current density as a function of time during the duration testing is shown in Fig. AD10. After 80 h substantial degradation had occurred. Visual inspection (after 80 h) showed small regions of discoloration (200-2000 μm^2) in the protective layer. In a representative region discoloured regions represented 5% of the area. Optical microscope images showed that the discolored regions were rectangular in shape, consistent with the known shape of etch pits on (100)-oriented Si. Cross-sectional SEM imaging confirmed that on the new device there was good adhesion between the protective/catalyst layer stack and the buried junction while the device run for 80 h in 1 M KOH showed multiple etch pits into the Si (Fig. 5.11). The buried junction is 100-200 nm deep, thus even relatively shallow etch pits can cause cross-junction shunting reducing the V_{oc}. The TiO_2 is apparently stable in 1 M KOH as the protective layer can be seen still intact and maintaining the pyramidal textured surface (Fig 5.11). At shorter testing times (1 - 24 h) the device efficiency still drops considerably but is easily recovered upon cycling the device in 1 M $HClO_4$. To verify that a reduction in catalytic activity was the mode of short-term failure identical stability testing was carried out on a 2 nm layer of Ir on Au (Fig AD6). The catalytic activity decreased significantly after 24 h but can be recovered with cycling in acid. The degradation of the HER activity of IrO_x has been observed previously.[159] These data provide strong evidence that short term degradation is due to contamination of the catalyst by electroplating of solution impurities blocking the active Ir sites and long-term irreversible degradation is due to failure of the protective layer through pin-holes.

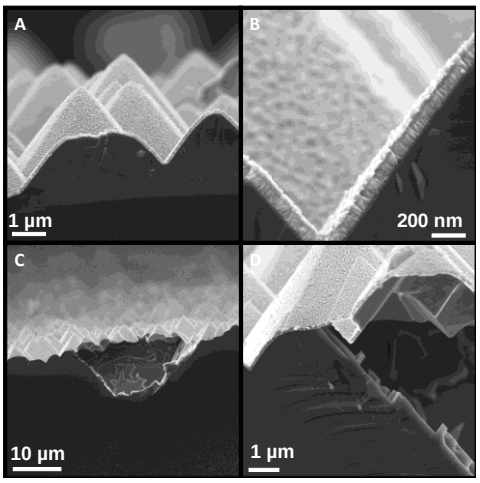

Figure 5.11. SEM images of protective layers before duration testing (a,b), and after 80 h of stability testing (c,d).

To better understand the long-term degradation mechanisms, Si(pn^+)-Ti-Ir and Si(pn^+)-Ti-FTO-Ir control devices were also tested. After holding a Si(pn^+)-Ti-Ir photocathode at open circuit for 1 h (Fig. AD4) the V_{oc} was significantly reduced and catalyst cleaning via anodic polarization did not restore the V_{oc} of the photocathode. The drop in V_{oc} suggests partial etching of the emitter causes shunt formation between the emitter and base layers of the buried junction (decreasing the V_{oc} by 59 mV for every order of magnitude increase in the dark current). Although dense TiO_2 should block base from reaching the Si, oxidation of Ti in base likely forms a porous hydrated oxide that allows electrolyte transport. After repeated cycling the fill factor of a Si(pn^+)-Ti-FTO-Ir protected photoelectrode also degraded with time (Fig. AD5). Anodic cleaning of the electrode did not recover the prior efficiency, thus eliminating catalyst contamination as the degradation mechanism. The V_{oc} and J_{sc} did not decrease indicating that the solid-state buried junction remained intact. Because F:SnO_2 is known to have partial solubility in base,[82] dissolution of the F:SnO_2 resulting in loss of Ir is the likely

cause of the performance degradation. These data thus illustrate the importance of the outermost dense TiO_2 layer for stability in the final devices.

Conclusion

Textured commercial solar cells can be used in conjunction with a thin layer of noble metal catalyst to test the stability and current-voltage characteristics of Si photocathode operating in base at high photocurrents. Solution-processed stacks of F:SnO_2 and TiO_2 provide protection of the Si photocathode in base for ~24 h and through interface control provide low resistance to charge transport. Reflection losses to a protective-layer-coated textured cell can be minimized with thicknesses near 40 nm. Integration of IrO_x catalyst led to photocathodes with >10% efficiency operating in base.

We also investigate the degradation mechanisms. Solution phase impurities in basic media remain a practical challenge when using thin catalyst films with low surface areas that can be easily covered with electrodeposited impurities. Rigorous pre-cleaning of the electrolyte might (partially) alleviate these issues. Such issues are not as severe in acid conditions due to the solubility of transition metals as well as the availability of higher-purity acid electrolytes.

Due to the presence of pinholes or other TiO_2 film defects, Si is slowly etched from under the protective layer forming large etch pits over the course of several days. Grain boundaries between the nanocrystalline TiO_2 may also play a role. Protective schemes used in acid to protect Si do not have to contend with this issue as pinholes are passivated by the formation of insoluble SiO_2 in acid. ALD methods, which are non-line-of-sight and proceed through self-limiting surface

reactions appear inherently better for the protection of non-planar Si. Although it is unclear if classic ALD is scalable, other related methods such as liquid-phase ALD might allow for pinhole free large scale films to be deposited.[162] Solution-processing of thicker more-conductive stable materials (Nb-doped TiO_2 is one possibility) might be able to provide long-term stability. In sum, these outline the optical/electrical design principles behind efficient photocathode fabrication as well as remaining challenges.

APPENDIX A: CHAPTER II SUPPLEMENTARY INFORMATION

Portions of this appendix was coauthored. Co-authored material (with B. A. Hammann, P. N. Plassmeyer, Z. L. Ma, K. N. Woods, D. A. Keszler, C. J. Page, S. W. Boettcher and S. E. Hayes). The excerpt to be included was written by B. A. Hammann and myself. D. A. Keszler, C. J. Page, S. W. Boettcher and S. E. Hayes provided editorial assistance. B. A. Hamman, P. N. Plassmeyer, Z. L. Ma, and K. N. Woods provided experimental assistance.

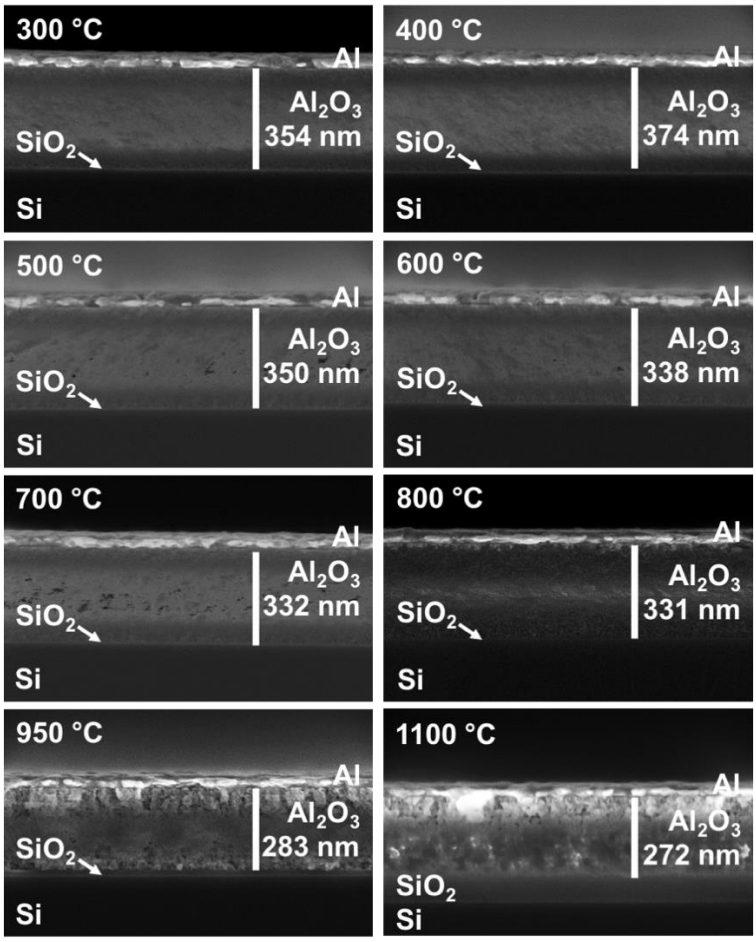

Figure AA1: Scanning electron microscopy of films prepared by PIC at various annealing temperatures ranging from 300 to 1100 °C.

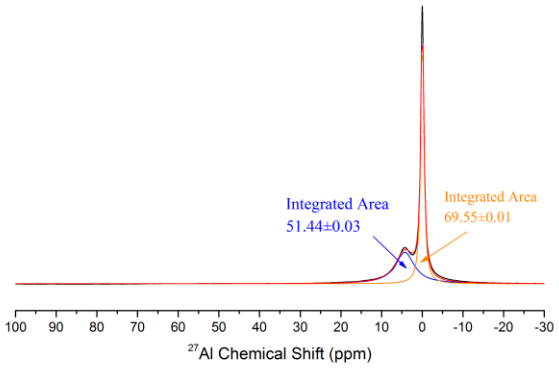

Figure AA2: ^{27}Al liquid-state NMR of the 1.3M Al_2O_3 precursor acquired at 130.25 MHz at a field of 11.8 T and referenced to 1 M $Al(NO_3)_3$ at 0 ppm.

Table AA1: Relative areas of deconvoluted ^{27}Al NMR spectra (normalized to 100%), and average coordination number (CN) for aluminum films.

T_a (˚C)	Fit Param.	$^{[4]}Al$	$^{[5]}Al$	$^{[6]}Al$
200	Amp	1.24	2.73	6.05
	δ_{ISO}, (ppm)	73.94	41.76	10.37
	δ_{CS}, (ppm)	4.62	6.92	7.46
	C_Q, (MHz)	9.27	8.29	5.55
	Em Au	500	500	500
	Integrated Area	22.12	39.03	38.85
300	Amp	2.2	4.32	8.11
	δ_{ISO}, (ppm)	73.42	41.82	9.92
	δ_{CS}, (ppm)	5.61	7.85	9.92
	C_Q, (MHz)	9.98	8.36	2.92
	Em Au	500	500	500
	Integrated Area	33.7	45.42	20.88
400	Amp	2.81	4.35	5.1
	δ_{ISO}, (ppm)	72.55	43.01	10.65
	δ_{CS}, (ppm)	1475.73	11.61	9.91
	C_Q, (MHz)	9.84	8.83	3.4
	Em Au	500	500	500
	Integrated Area	40.59	50.59	8.81
500	Amp	2.91	3.88	2.3

	δ_{ISO}, (ppm)	73.36	42.63	9.12
	δ_{CS}, (ppm)	10.43	9.62	9.12
	C_Q, (MHz)	10.92	8.74	5.78
	Em Au	500	500	500
	Integrated Area	48.04	41.67	10.29
600	Amp	2.99	3.66	2.26
	δ_{ISO}, (ppm)	72.5	42.84	13.86
	δ_{CS}, (ppm)	10.13	9.93	9.35
	C_Q, (MHz)	11.08	9.46	5.6
	Em Au	500	500	500
	Integrated Area	47.92	42.82	9.27
700	Amp	3.03	4.05	1.33
	δ_{ISO}, (ppm)	73.14	42.84	14.93
	δ_{CS}, (ppm)	9.94	11.85	9
	C_Q, (MHz)	11.13	8.85	6.84
	Em Au	500	500	500
	Integrated Area	49.64	42.1	8.26
800	Amp	3.13	3.52	2.36
	δ_{ISO}, (ppm)	73.82	42.6	14.82
	δ_{CS}, (ppm)	8.22	9.91	7.69
	C_Q, (MHz)	11.51	9.6	6.48
	Em Au	500	500	500
	Integrated Area	49.38	38.78	11.84

Table S1 Cont'd: Relative areas of deconvoluted ^{27}Al NMR spectra (normalized to 100%), and average coordination number (CN) for aluminum oxide films.

T_a (˚C)	Fit Param.	$^{[4]}$Al	$^{[5]}$Al	$^{[6]}$Al
950	Amp	1.94	0.21	5.95
	δ_{ISO}, (ppm)	75.17	42.6	15.16
	δ_{CS}, (ppm)	9.36	10	7.34
	C_Q, (MHz)	7.59	9.62	5.78
	Em Au	500	500	500

	Integrated Area	33.82	5.94	60.25
1100	Amp	1.23	-	5.71
	δ_{ISO}, (ppm)	77.74	-	16.72
	δ_{CS}, (ppm)	10.87	-	6.44
	C_Q, (MHz)	8.48	-	5.88
	Em Au	500	-	500
	Integrated Area	30.97	-	69.03

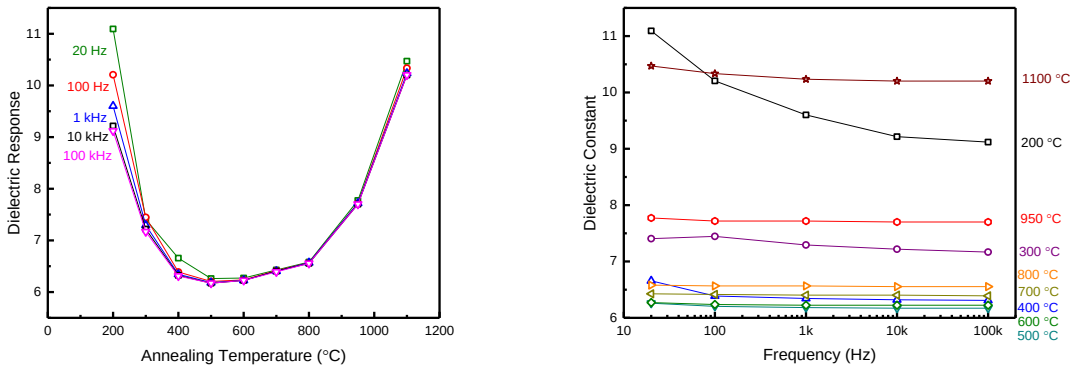

Figure AA3: Dielectric constant of the films as a function of temperature and frequency.

APPENDIX B: CHAPTER III SUPPLEMENTARY INFORMATION

Portions of this chapter were previously submitted to publish as Kast, M.G.; Cochran, E.A.; Enman, L.J.; Mitchson, G.; Ditto, J.; Siefe, C.; Plassmeyer, P.N.; Johnson, D.C.; Page, C.J.; Boettcher, S.W. Amorphous Mixed-Metal Oxide Thin Films from Aqueous Solution Precursors with Near Atomic Smoothness. The excerpt to be included was written entirely by me. D. C. Johnson, C. J. Page and S. W. Boettcher provided editorial assistance. E. A. Cochran, L. J. Enman, G. Mitchson, J. Ditto, C. Siefe and P. N. Plassmeyer provided experimental assistance.

Table AB1. Details on chemicals used

Chemical Formula	Supplier	Purity
$Al(NO_3)_3 \cdot 9H_2O$	Alfa Aesar	98%
H_3PO_4 85% w/w	Alfa Aesar	99%
VCl_3	Sigma-Aldrich	97%
$Cr(NO_3)_3 \cdot 9H_2O$	J.T. Baker	98.7%
$Mn(NO_3)_2 \cdot 6H_2O$	Sigma-Aldrich	98%
$Fe(NO_3)_3 \cdot 9H_2O$	Sigma-Aldrich	98%
$Co(NO_3)_2 \cdot 6H_2O$	Alfa Aesar	97.7%
$Ni(NO_3)_2 \cdot 6H_2O$	Alfa Aesar	98%
$Cu(NO_3)_2 \cdot 3H_2O$	Strem Chemicals	99.5%
$Zn(NO_3)_2 \cdot 6H_2O$	Sigma-Aldrich	99%

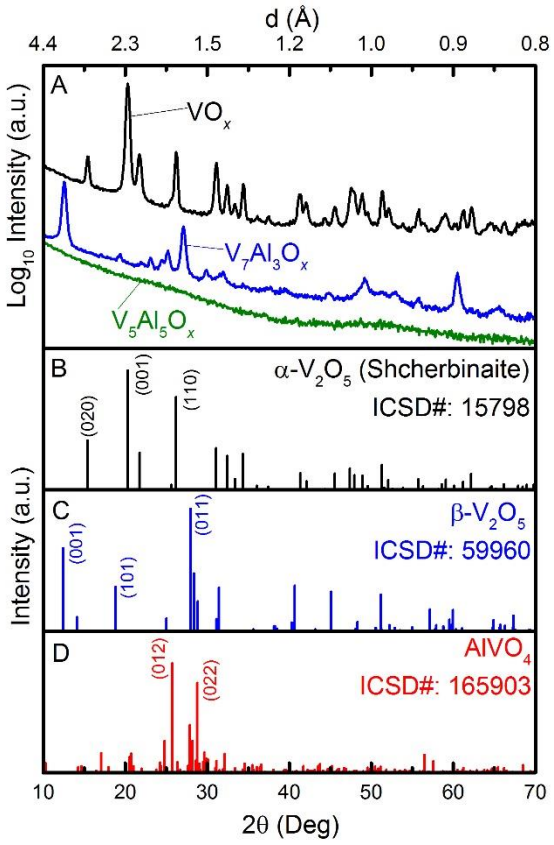

Figure AB1. (A) GIXRD of $V_yAl_{1-y}O_x$ films (from Figure 3.1), (B) reference α-V_2O_5 (Shcherbinaite)[95], (C) reference β-V_2O_5[163] and (D) reference $AlVO_4$.[164] The VO_x film crystallizes into phase pure α-V_2O_5. The $V_5Al_5O_x$ film is amorphous. The $V_7Al_3O_x$ film shows Bragg diffraction with a high intensity peak at 12.5°, corresponding to a d-spacing of 3.5 Å. This large d-spacing is likely due to a layered structure, which is not unexpected considering that V_2O_5 has a layered structure in both the α and β phase albeit with different spacing and in-sheet geometries. The observed pattern for $V_7Al_3O_x$ matches well with the (001) and (011) reference data for β-V_2O_5 with a non-ideal match across the rest of the 2θ range. It is possible Al cations intercalate between V_2O_5 sheets and stabilizes the (high pressure) β-V_2O_5 phase relative to the predominant α-V_2O_5 phase. Al^{3+} (in the form of a Keggin polycation) intercalation into hydrated-layered V_2O_5 phases

has been previously reported up to 25% Al.[165] The highly stable mixed $AlVO_4$ does not appear to be present but cannot be ruled out, the same is true for Al^{3+} substitution into the VO_x sheets and the presence of amorphous domains of Al_2O_3.

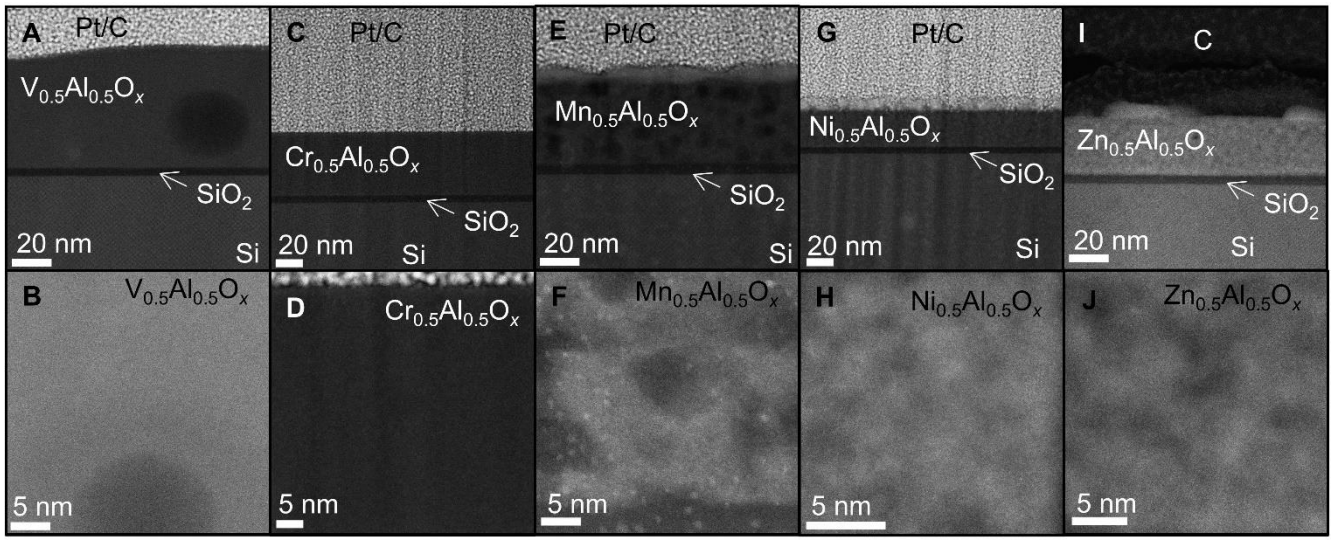

Figure AB2. High angle annular dark field scanning transmission electron microscopy (HAADF-STEM) was used to further understand the morphology of films with very large fractions (50%) of transition metal oxide. Consistent with GIXRD experiments (Figure 3.1), both $V_{0.5}Al_{0.5}O_x$ and $Cr_{0.5}Al_{0.5}O_x$ appear completely amorphous by HAADF-STEM with no ordered nanocrystalline regions present. The $Cr_{0.5}Al_{0.5}O_x$, in particular, is exceptionally smooth and uniform, similar to the Al_2O_3 and $Fe_{0.5}Al_{0.5}O_Y$ films as seen by HRTEM and consistent with XRR and AFM results (R_{rms} ~ 0.1 nm). The $V_{0.5}Al_{0.5}O_x$, while amorphous, does appear to show some density contrast as evidence by the darker region in the HAADF-STEM image and consistent with the increased average roughness obtained from XRR measurements (R_{rms} ~ 1 nm). The $Mn_{0.5}Al_{0.5}O_x$ similarly shows small density variations in the film at these high concentrations, consistent with the onset of phase segregation evident from the GIXRD analysis. $Zn_{0.5}Al_{0.5}O_y$ and $Ni_{0.5}Al_{0.5}O_y$ films

show small nanocrystalline regions present in the film with d-spacing which correspond with those seen by GIXRD, providing direct visualization of phase segregation in these mixed films. The small light spots evident particularly in E/F are related to FIB sample preparation and not the sample.

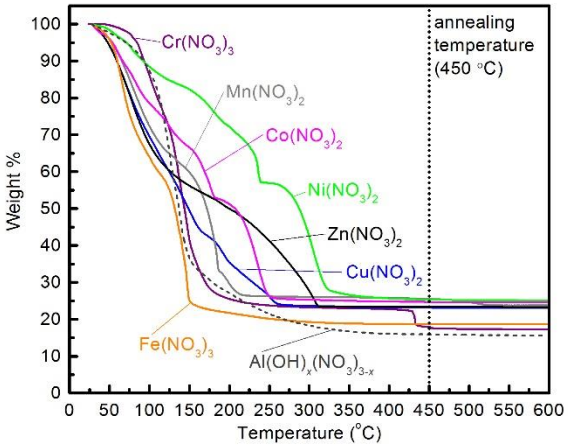

Figure AB3. Bulk thermogravimetric analysis (TGA) of the precursor components used in this study.

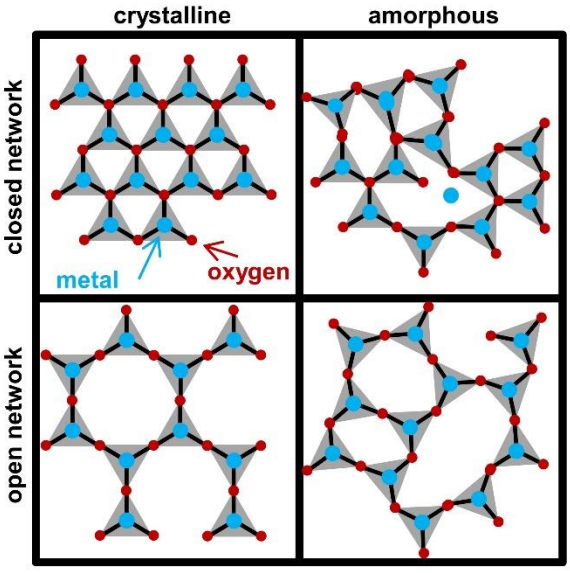

Figure AB4. Comparison between the ability of an open network and a closed network to form an amorphous network schematically shown in 2D. Blue circles represent metal

cations, red circles represent oxygen anions, black lines represent bonds and grey triangles represent cation polyhedra. Closed networks must put strain on the local order around metals and may result in over or under coordinated metals. Open networks can maintain an open network with only rotational disorder on the oxygen centers.

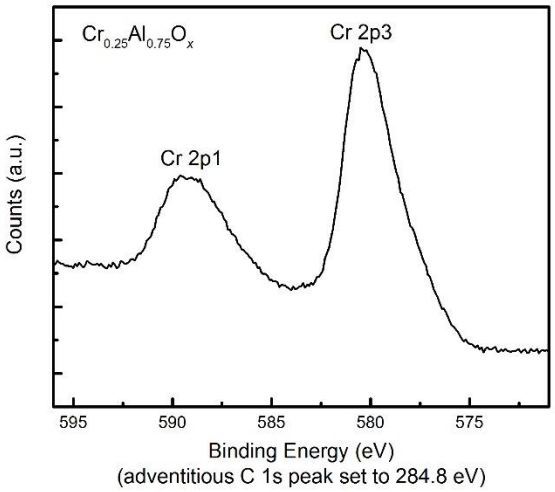

Figure AB5. X-ray Photoelectron Spectra (XPS) of a $Cr_{0.25}Al_{0.75}O_x$ film annealed at 450 °C. The spectrum was collected on a ThermoScientific ESCALAB system using a monochromated Al Kα source. In comparison to the work of Biesinger & coworkers, whose air-cleaved Cr_2O_3 samples would be most relevant, it is clear by shape and position that the Cr in the films reported here are not pure Cr^{3+}.[166] Furthermore, comparing to the work of Aroniemi, Sainio and coworkers it is clear that a substantial fraction of the Cr is in the 6+ oxidation state due to the centering of Cr 2p3 peak at a binding energy of 580 eV.[167,168]

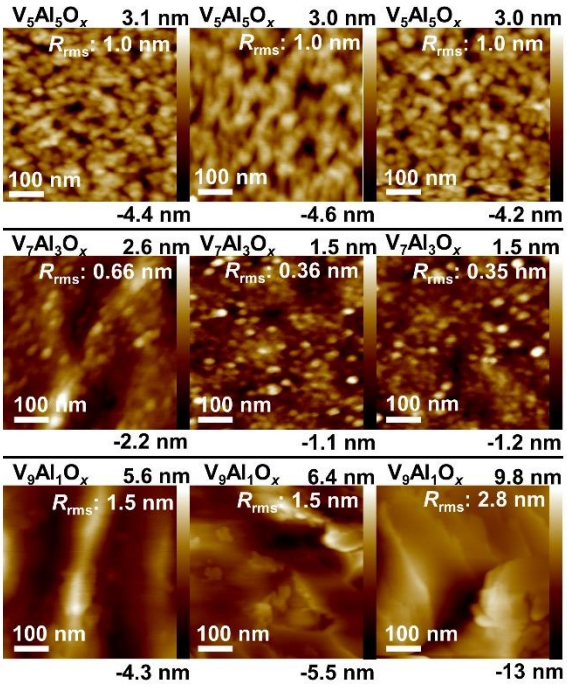

Figure AB6. AFM images of $V_yAl_{1-y}O_x$ thin films.

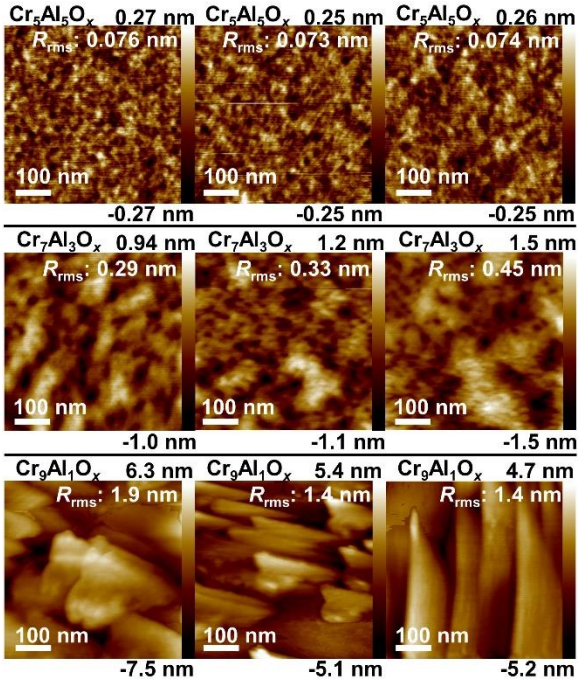

Figure AB7. AFM images of $Cr_yAl_{1-y}O_x$ thin films.

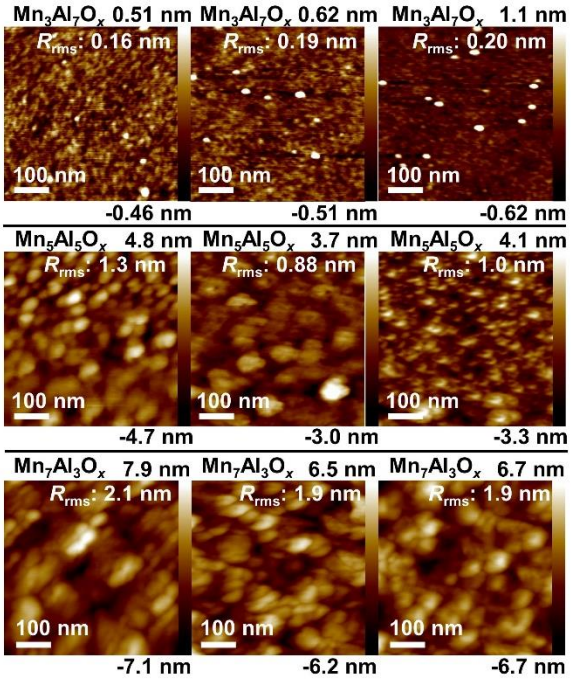

Figure AB8. AFM images of $Mn_yAl_{1-y}O_x$ thin films.

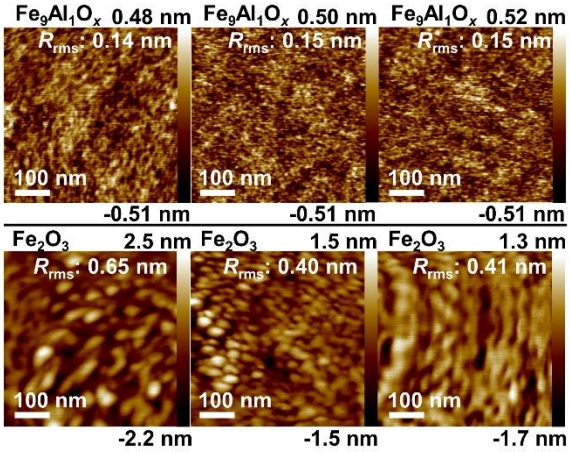

Figure AB9. AFM images of $Fe_yAl_{1-y}O_x$ thin films.

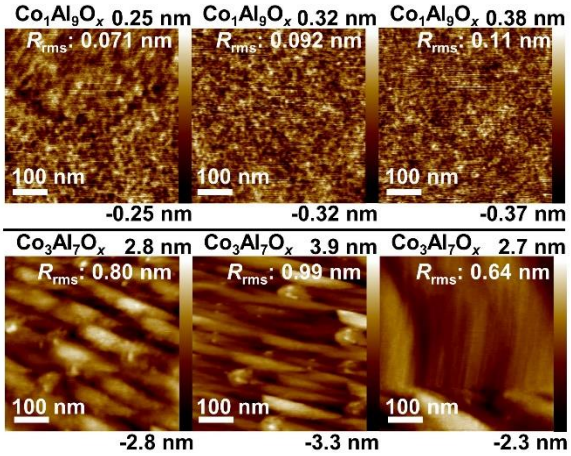

Figure AB10. AFM images of $Co_yAl_{1-y}O_x$ thin films.

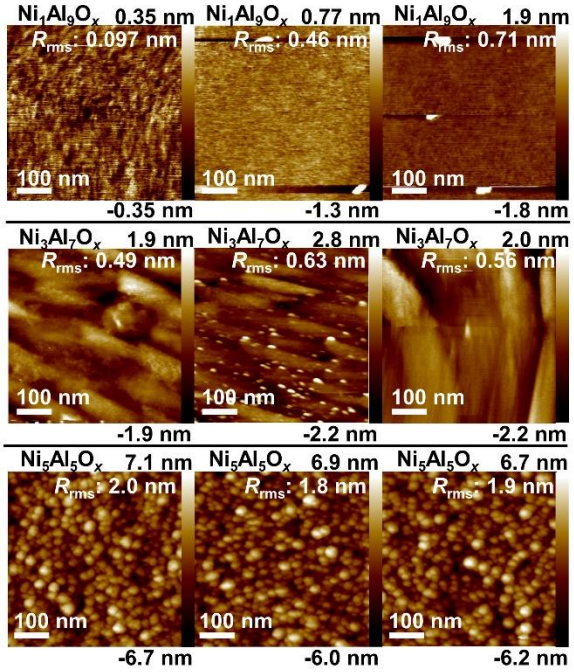

Figure AB11. AFM images of $Ni_yAl_{1-y}O_x$ thin films.

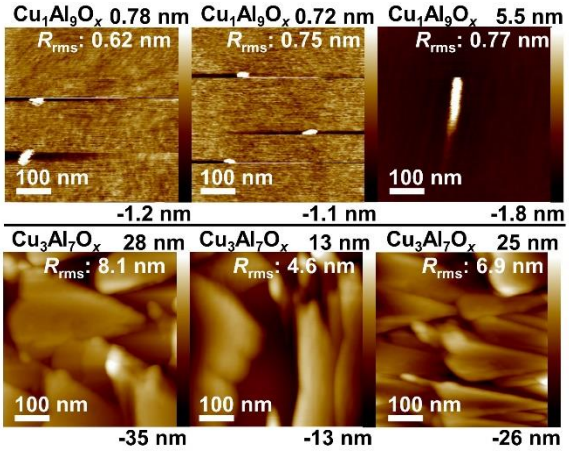

Figure AB12. AFM images of $Cu_yAl_{1-y}O_x$ thin films.

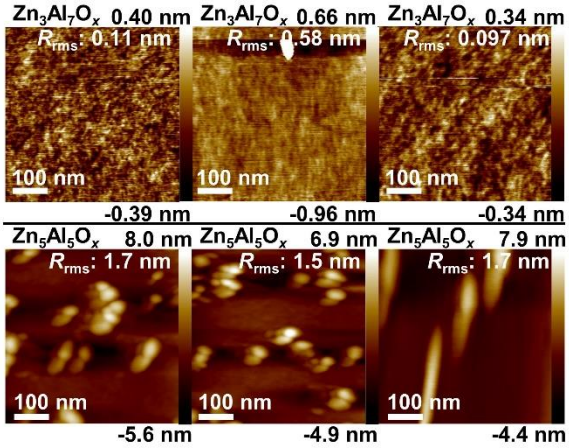

Figure AB13. AFM images of $Zn_yAl_{1-y}O_x$ thin films.

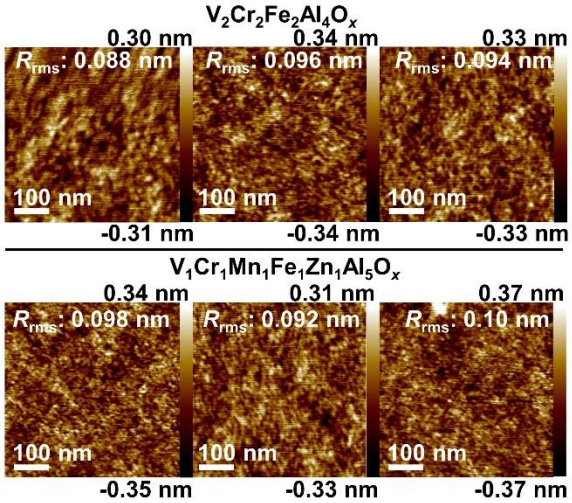

Figure AB14. AFM images of $V_1Cr_1Mn_1Fe_1Zn_1Al_5O_x$ and $V_2Cr_2Fe_2Al_4O_x$ thin films.

APPENDIX C: CHAPTER V SUPPLEMENTARY INFORMATION

Portions of this chapter were previously published as Kast, M. G.; Enman, L. J.; Gurnon, N. J.; Nadarajah, A.; Boettcher, S. W. Solution-Deposited F:SnO_2/TiO_2 as a Base-Stable Protective Layer and Antireflective Coating for Microtextured Buried-Junction H_2-evolving Si Photocathodes. *ACS Applied Materials and Interfaces* 2014, 6, 22830-22837. The experimental work was performed either by me or by L. J. Enman, N. J. Gurnon and A. Nadarajah under my and S. W. Boettcher's direction. S. W. Boettcher provided editorial assistance.

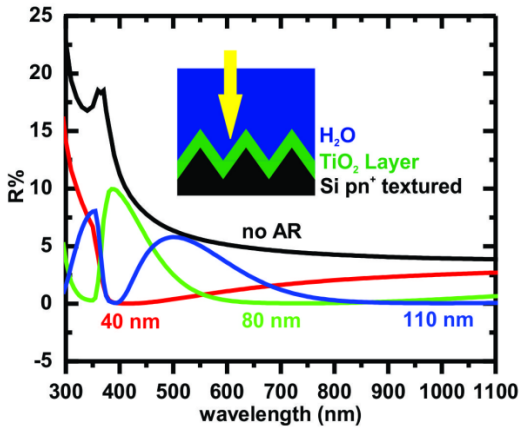

Figure AC1: Modeled reflectivity (on the left) of textured Si with 0, 40, 80 and 110 nm of TiO_2 under water showing a significant decrease in reflectivity due to the protective coating. Modeling was done with Opal 2 using random upright pyramids with an angle of 54.74° (angle between [100] and [111] planes) for texturing.[169] Literature values for the index of refraction of H_2O, TiO_2 and Si were used.[170–172]

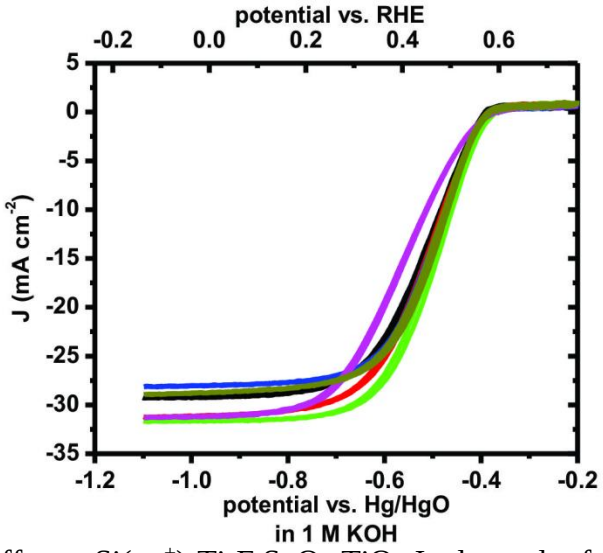

Figure AC2: Six different Si(pn^+)-Ti-F:SnO_2-TiO_2-Ir electrodes fabricated in one batch, current densities are within 5 mA cm^{-2} of each other which appears to be the limit of reproducibility, one electrode shows increased series resistance in the low voltage regime.

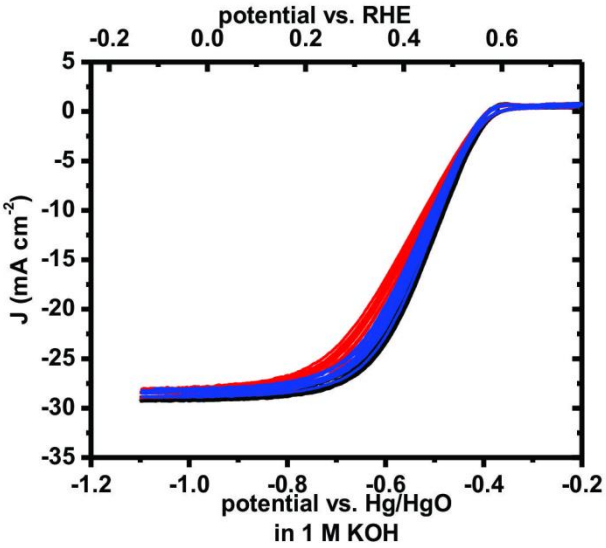

Figure AC3: Reproducibility of measured J_{SC} of single photocathode. One photocathode was placed in the cell for five cycles (black), removed from the cell, replaced and run for five more cycles (blue) and removed and replaced a second time (red). Variance in J_{SC} is less than 3 mA cm^{-2}, however J_{SC} drops with cycling time so it is possible that some of

this drop is due to contamination of the electrode and not variation in experimental conditions.

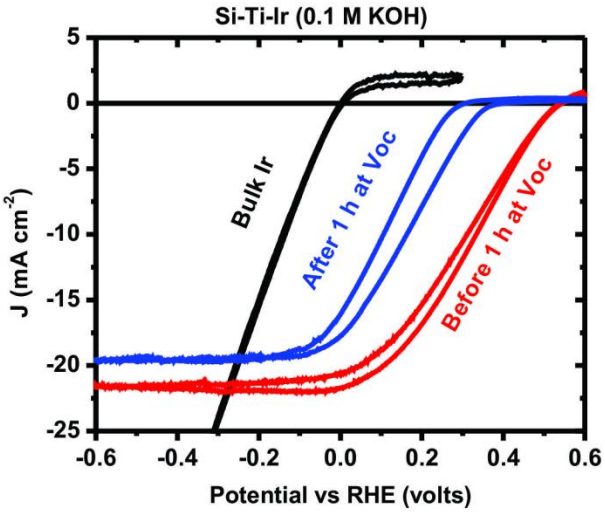

Figure AC4: Voltammograms of Ti protected silicon photocathodes under AM1.5 illumination.

The V_{OC} drops after 1 h at open circuit conditions. This is likely due to etching into the junction causing shorts across the junction. Lower J_{SC} (~ 20 mA cm^{-2} compared to ~30 mA cm^{-2} seen in oxide protected photocathodes) is likely due to the lower transmittance of metallic titanium and the lack of oxide AR coatings on the cell. The sample was under AM1.5 illumination while it was held for 1 h at V_{oc}.

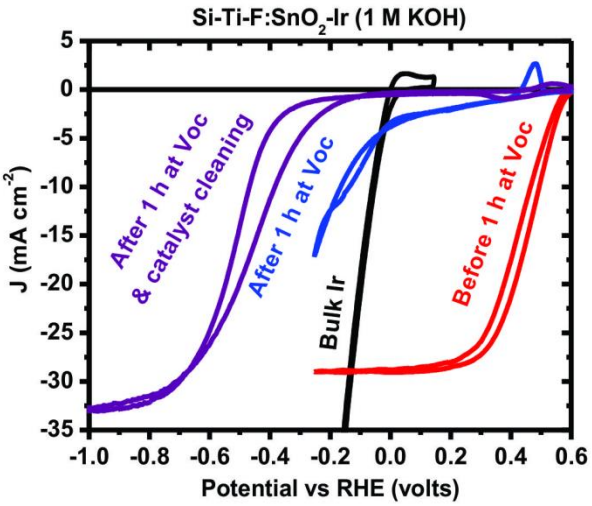

Figure AC5: Voltammograms of Si(pn^+)-Ti-F:SnO_2-Ir photocathodes under AM1.5 illumination.

Although the Voc is not reduced in the short duration scan, the activity is not recoverable. This is likely due to loss of electrical contact between the catalyst and the pn^+ junction upon dissolution of the F:SnO_2. The sample was under AM1.5 illumination while it was held for 1 h at V_{oc}.

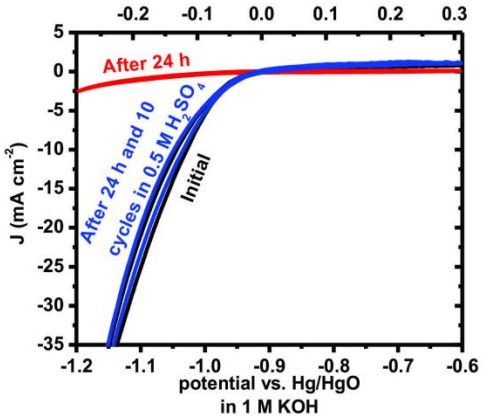

Figure AC6: Duration testing of a 2 nm Ir layer on Au, the catalyst degrades with time and is recovered by cycling in acid the same way that the full cells are. This further

supports that it is the catalyst performance and not the underlying cell that degrades with time at first and only during longer testing is it the cell that is damaged.

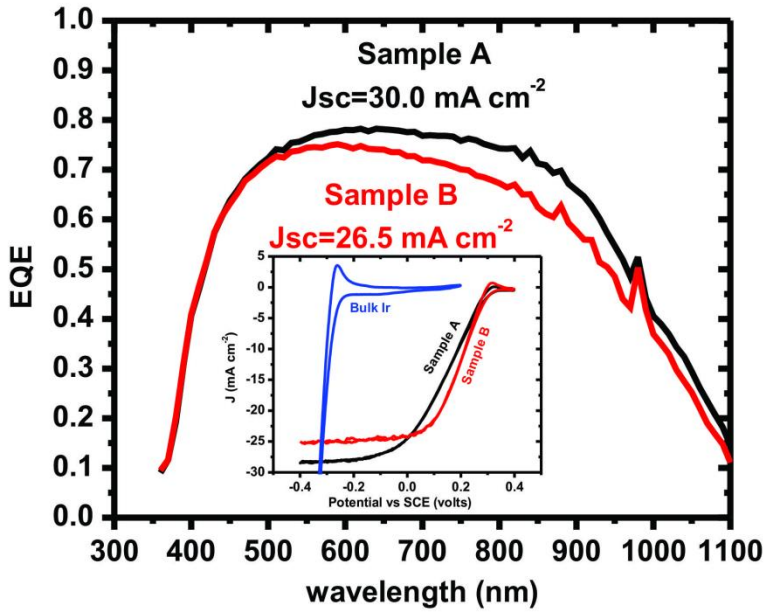

Figure AC7: External quantum efficiency data was collected on two photocathodes in 1 M KOH. EQE data were corrected for the transmittance of the plastic optical window (optical illumination was set to 1 sun inside the cell) on the high purity base cell. The external quantum efficiency data was integrated with the spectrum of the AM1.5 Solar simulator. This yielded predicted J_{SC} of 30.0 and 26.5 mA cm^{-2}. This correlates well with J_{SC} of the same photocathodes taken 10 min prior in 0.5 M H_2SO_4 acid cell.

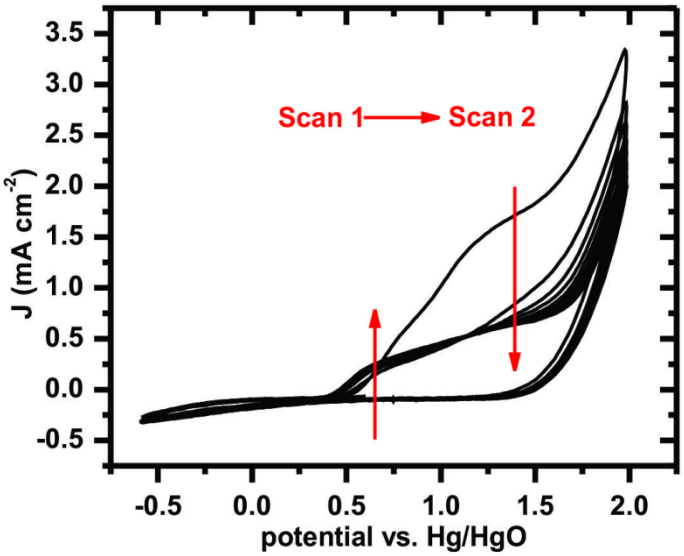

Figure AC8: Representative oxidizing voltammogram used to clean the catalyst (on a pSi-n^{+}Si-Ti-F:SnO_2-TiO_2-Ir photocathode) of contaminants in 1 M $HClO_4$. Potential vs. Hg/HgO, scan rate is 500 mV s^{-1}. The high anodic currents seen in the first cycle are likely do to anodic stripping of deposited contaminants (Fe, Cu and Pb as seen in the XPS Fig. AD12). The current not attributed to OER (i.e. anodic current at potentials greater than 1.5 vs. Hg/HgO) is likely a combination of adsorption and desorption (of protons or hydroxides) currents on Ir and non-faradic charging and discharging.

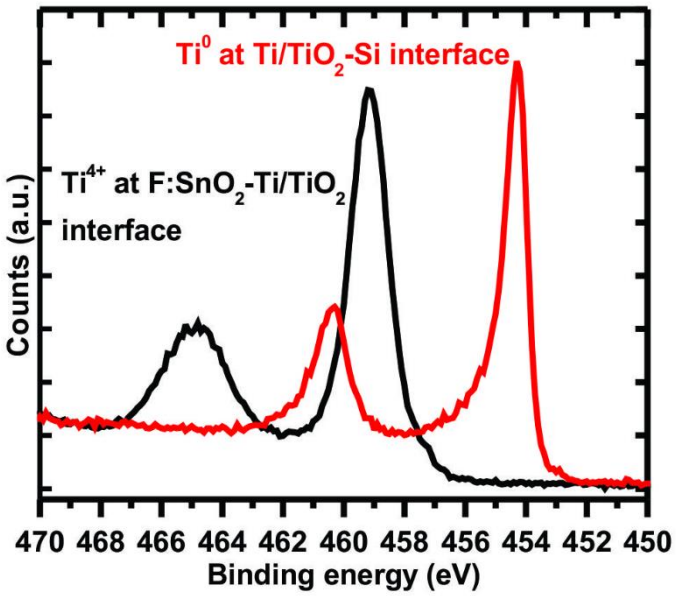

Figure AC9: XP Ti spectra from a depth-profiled experiment on a F:SnO_2-Ti-Si stack (same sample as shown in Fig. 5.6B). In black is a spectra collected at the F:SnO_2-Ti/TiO_2 interface and in red is one from the Ti the Ti-Si interface. The larger (Ti_{2p3}) peaks at ~459 and ~454 eV correspond to the expected values for Ti^{4+} (in TiO_2) and Ti^{0}

(in Ti). We note that the Ar etch beam did reduce the TiO_2 to Ti^{3+} species after sustained etching, but it is unlikely that the beam was able to reduce to TiO_2 all the way to Ti.

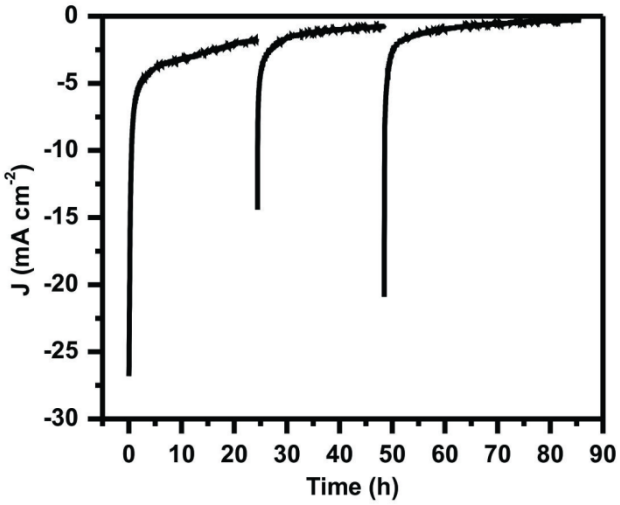

Figure AC10: Plot of current density vs. time during the duration study shown in Fig. 5.10. The photocathode was held at 300 mV positive of RHE. The cathodic peaks in current at 24 and 48 h are due to breaks in the duration study during which the cyclic voltammograms shown in Fig. 5.10 were taken and cycling in acid was carried out to determine whether catalyst or junction degradation was the primary failure mode.

Catalyst	Overpotential (mV) at 15 mA cm^{-2}
Pt	**157**
Pt + Li^+	**143**
Ir	**114**
Pt + $Ni(OH)_2$	**109**
Pt + $Ni(OH)_2$ + Li^+	**99**
IrO_x	**80**
Ir + $Ni(OH)_2$	**79**
Ir + $Ni(OH)_2$ + Li^+	**76**
Pt in 0.5 M H_2SO_4	**30**

Figure AC11: Tabulated values of the overpotential of the catalysts shown in Fig. 5.4 at 15 mA cm^{-2}.

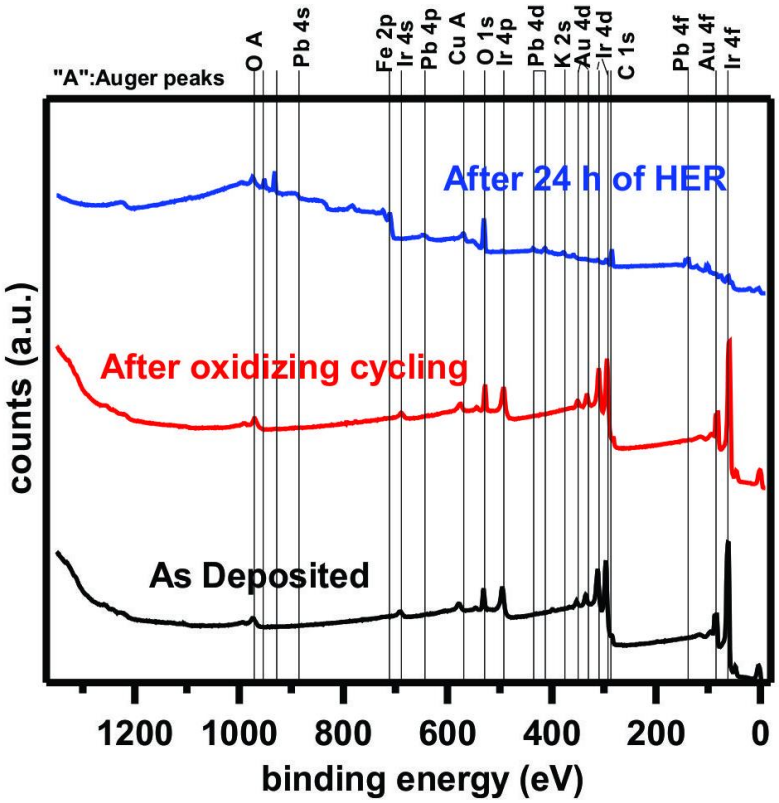

Figure AC12: Survey scans of the Ir/IrO_x catalyst on Au as deposited (Ir deposition via ebeam evaporation), after oxidative scans to increase the activity of the catalyst and after 24 h of HER. The survey scan dramatically changes after 24 h of HER, this is attributed to the presence of Fe, Pb and Cu which were not previously seen on the other two scans. The trace lot analysis of the KOH showed Fe and Cu at 0.3 and 0.4 ppm, respectively, while Pb

was not looked for. Fe, Pb and Cu have very low HER activity and therefore would be expected to poison the Ir/IrO_x surface.

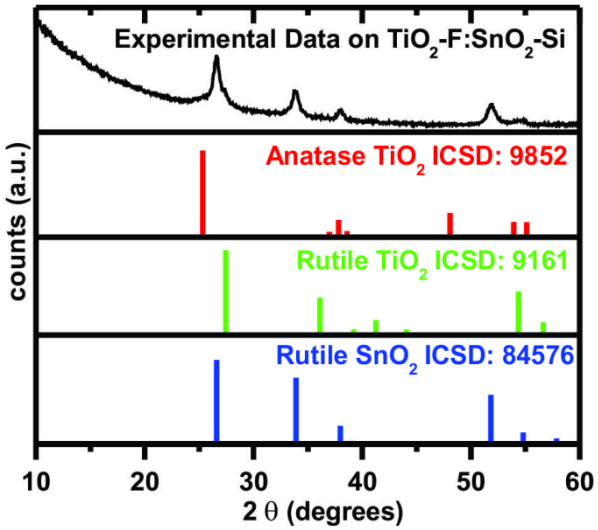

Figure AC13: Thin film X-ray diffraction data taken of a TiO_2-F:SnO_2 stack on Si. Rutile SnO_2 is clearly present along with a possible mixture of anatase and rutile TiO_2. Ellipsometry measurements collected on TiO_2 deposited on a planar substrate show the film to have an index of refraction of 2.2 which corresponds 82 % of the density of single crystal anatase (using effective medium theory).

REFERENCES CITED

(1) Filatova, E. O.; Konashuk, A. S. *J. Phys. Chem. C* **2015**, *119* (35), 20755–20761.
(2) Smith, S. W.; Wang, W.; Keszler, D. A.; Conley, J. F. *J. Vac. Sci. Technol. A Vacuum, Surfaces, Film.* **2014**, *32* (4), 1–7.
(3) DaSilva, E.M.; White, P. *J. Electrochem. Soc.* **1962**, *109* (1), 12–15.
(4) Kim, J. B.; Fuentes-Hernandez, C.; Potscavage, W. J.; Zhang, X.-H.; Kippelen, B. *Appl. Phys. Lett.* **2009**, *94* (14), 142107.
(5) Lim, S. J.; Kwon, S. J.; Kim, H.; Park, J. S. *Appl. Phys. Lett.* **2007**, *91* (18), 2014–2017.
(6) Park, J. S.; Maeng, W. J.; Kim, H. S.; Park, J. S. *Thin Solid Films* **2012**, *520* (6), 1679–1693.
(7) Fortunato, E.; Barquiha, P.; Martins, R. *Adv. Mater.* **2012**, *24* (22), 2945–2986.
(8) Hoex, B.; Heil, S. B. S.; Langereis, E.; Van De Banden, M. C. M.; Kessels, W. M. M. *Appl. Phys. Lett.* **2006**, *89* (4), 3–6.
(9) Agostinelli, G.; Delabie, A.; Vitanov, P.; Alexieva, Z.; Dekkers, H. F. W.; De Wolf, S.; Beaucarne, G. *Sol. Energy Mater. Sol. Cells* **2006**, *90* (18–19), 3438–3443.
(10) Valant, M.; Luin, U.; Fanetti, M.; Mavri, A.; Vyshniakova, K.; Siketi, Z.; Kalin, M. *Adv. Funct. Mater.* **2016**, *26* (24), 4362–4369.
(11) Sarou-Kanian, V.; Gleizes, A. N.; Florian, P.; Samélor, D.; Massiot, D.; Vahlas, C. *J. Phys. Chem. C* **2013**, *117*, 21965–21971.
(12) Stevels, J. M. *Monographs on the Progress of Research in Holland During the War*; 1948.
(13) Kim, N.; Bassiri, R.; Fejer, M. M.; Stebbins, J. F. *J. Non. Cryst. Solids* **2014**, *405*, 1–6.
(14) Paladino, A. E.; Kingery, W. D. *J. Chem. Phys.* **1962**, *37* (5), 957–962.
(15) Uematsu, M.; Kageshima, H.; Takahashi, Y.; Fukatsu, S.; Itoh, K. M.; Shiraishi, K.; Gösele, U. *Appl. Phys. Lett.* **2004**, *84* (6), 876–878.
(16) Lee, S. K.; Park, S. Y.; Yi, Y. S.; Moon, J. *J. Phys. Chem. C* **2010**, *114* (32), 13890–13894.
(17) Lee, S. K.; Park, S. B.; Park, S. Y.; Yi, Y. S.; Ahn, C. W. *Phys. Rev. Lett.* **2009**, *103* (9), 1–4.
(18) Dien Li; Bancroft, G. M.; Fleet, M. E.; Feng, X. H.; Pan, Y. *Am. Mineral.* **1995**, *80* (5–6), 432–440.
(19) Lee, S. K.; Park, S. Y.; Yi, Y. S.; Moon, J. *J. Phys. Chem. C* **2010**, *114* (32), 13890–13894.
(20) Wang, W.; Liu, W.; Chang, I.-Y.; Wills, L. A; Zakharov, L. N.; Boettcher, S. W.; Cheong, P. H.-Y.; Fang, C.; Keszler, D. a. *Proc. Natl. Acad. Sci. U. S. A.* **2013**, *110* (46), 18397–18401.
(21) Larsen, F. H.; Jakobsen, H. J.; Ellis, P. D.; Nielsen, N. C. *J. Magn. Reson.* **1998**, *131* (1), 144–147.
(22) Larsen, F. H.; Jakobsen, H. J.; Ellis, P. D.; Nielsen, N. C. *J. Phys. Chem. A* **1997**, *5639* (97), 8597–8606.
(23) Massiot, D.; Fayon, F.; Capron, M.; King, I.; Le Calvé, S.; Alonso, B.; Durand, J.-O.; Bujoli, B.; Gan, Z.; Hoatson, G. *Magn. Reson. Chem.* **2002**, *40* (1), 70–76.

(24) Czjzek, G.; Fink, J.; Götz, F.; Schmidt, H.; Coey, J. M. D.; Rebouillat, J.-P.; Liénard, A. *Phys. Rev. B* **1981**, *23* (6), 2513–2530.
(25) d'Espinose de Lacaillerie, J.-B.; Fretigny, C.; Massiot, D. *J. Magn. Reson.* **2008**, *192* (2), 244–251.
(26) Le Caër, G.; Bureau, B.; Massiot, D. *J. Phys. Condens. Matter* **2010**, *22* (6), 65402.
(27) Neuville, D. R.; Cormier, L.; Massiot, D. *Geochim. Cosmochim. Acta* **2004**, *68* (24), 5071–5079.
(28) Ishizawa, N.; Miyata, T.; Minato, I.; Marumo, F.; Iwai, S. *Acta Crystallogr. Sect. B* **1980**, *36* (2), 228–230.
(29) Repelin, Y.; Husson, E. *Mater. Res. Bull.* **1990**, *25* (5), 611–621.
(30) Wefers, K.; Misra, C. *Alcoa Tech. Pap.* **1987**, *19*, 100.
(31) O'Dell, L. A.; Savin, S. L. P.; Chadwick, A. V.; Smith, M. E. *Solid State Nucl. Magn. Reson.* **2007**, *31* (4), 169–173.
(32) Lee, M.-H.; Cheng, C.-F.; Heine, V.; Klinowski, J. *Chem. Phys. Lett.* **1997**, *265* (96), 673–676.
(33) Sabarinathan, V.; Ramasamy, S.; Ganapathy, S. *J. Phys. Chem. B* **2010**, *114* (5), 1775–1781.
(34) Wang, X.; Guo, Y.; Lu, G.; Hu, Y.; Jiang, L.; Guo, Y.; Zhang, Z. *Catalysis Today* **2007**, *126*, 369–374.
(35) Rouchon, D.; Rochat, N.; Gustavo, F.; Chabli, A.; Renault, O.; Besson, P. *Surf. Interface Anal.* **2002**, *34* (1), 445–450.
(36) Tian, R.; Seitz, O.; Li, M.; Hu, W. (Walter); Chabal, Y. J.; Gao, J. *Langmuir* **2010**, *26* (7), 4563–4566.
(37) Xu, W.; Wang, H.; Xie, F.; Chen, J.; Cao, H.; Xu, J.-B. *ACS Appl. Mater. Interfaces* **2015**, *7* (10), 5803–5810.
(38) Ozer, N.; Cronin, J. *Sol. Energy Mater.***1999**, *59*, 355–366.
(39) Shamala, K. S.; Murthy, L. C. S.; Narasimha Rao, K. *Mater. Sci. Eng. B* **2004**, *106* (3), 269–274.
(40) Damodaran, K.; Rajamohanan, P. R.; Chakrabarty, D.; Racherla, U. S.; Manohar, V.; Fernandez, C.; Amoureux, J. P.; Ganapathy, S. *J. Am. Chem. Soc.* **2002**, *124* (13), 3200–3201.
(41) Samain, L.; Jaworski, A.; Edén, M.; Ladd, D. M.; Seo, D. K.; Javier Garcia-Garcia, F.; Häussermann, U. *J. Solid State Chem.* **2014**, *217*, 1–8.
(42) Ferreira, A. R.; Kuckukbeli, E.; Leitao, A. A.; De Gironcoli, S. *Phys. Rev. B - Condens. Matter Mater. Phys.* **2011**, *84* (23), 1–10.
(43) Wallin, E.; Münger, E. P.; Chirita, V.; Helmersson, U. *J. Phys. D. Appl. Phys.* **2009**, *42* (12), 125302.
(44) Sarou-Kanian, V.; Gleizes, A. N.; Florian, P.; Samélor, D.; Massiot, D.; Vahlas, C. *J. Phys. Chem. C* **2013**, *117*, 21965–21971.
(45) Momida, H.; Hamada, T.; Takagi, Y.; Yamamoto, T.; Uda, T.; Ohno, T. *Phys. Rev. B* **2006**, *73* (5), 54108.
(46) Tanenbaum, M.; Valdes, L. B.; Buehler, E.; Hannay, N. B. *J. Appl. Phys.* **1955**, *26* (6), 686–692.
(47) Wilk, G. D.; Wallace, R. M. *Appl. Phys. Lett.* **1999**, *74* (19), 2854–2856.
(48) Kingon, A. I.; Maria, J.; Streiffer, S. K. *Nature* **2000**, *406*, 1032–1038.

(49) Cousins, P. J.; Smith, D. D.; Luan, H.-C.; Manning, J.; Dennis, T. D.; Waldhauer, A.; Wilson, K. E.; Harley, G.; Mulligan, W. P. In *35th IEEE Photovoltaic Specialists Conference*; 2010; pp 275–278.
(50) Masuko, K.; Shigematsu, M.; Hashiguchi, T.; Fujishima, D.; Kai, M.; Yoshimura, N.; Yamaguchi, T.; Ichihashi, Y.; Mishima, T.; Matsubara, N.; Yamanishi, T.; Takahama, T.; Taguchi, M.; Maruyama, E.; Okamoto, S. *IEEE J. Photovoltaics* **2014**, *4* (6), 1433–1435.
(51) Green, M. A.; Emery, K.; Hishikawa, Y.; Warta, W.; Dunlop, E. D. *Prog. Photovolt Res. Appl.* **2015**, *23*, 1–9.
(52) Nomura, K.; Ohta, H.; Takagi, A.; Kamiya, T.; Hirano, M.; Hosono, H. *Nature* **2004**, *432* (November), 488–492.
(53) Cowell, E. W. (III); Alimardani, N.; Knutson, C. C.; Conley, J. F. (Jr); Keszler, D. A.; Gibbons, B. J.; Wager, J. F. *Adv. Mater.* **2011**, *23*, 74–78.
(54) Lucovsky, G.; Wu, Y.; Niimi, H.; Misra, V.; Phillips, J. C. *Appl. Phys. Lett.* **1999**, *74* (1999), 1–3.
(55) Jiang, K.; Meyers, S. T.; Anderson, M. D.; Johnson, D. C.; Keszler, D. A. *Chem. Mater.* **2013**, *25*, 210–214.
(56) Eades, W. D.; Swanson, R. M. *J. Appl. Phys.* **1985**, *58* (11), 4267–4276.
(57) Aberle, A. G. *Prog. Photovolt Res. Appl.* **2000**, *8*, 473–487.
(58) Callegari, A.; Cartier, E.; Gribelyuk, M.; Okorn-Schmidt, H. F.; Zabel, T. *J. Appl. Phys.* **2001**, *90*, 6466–6475.
(59) Spear, W. E.; Comber, P. G. Le. *Solid State Commun.* **1975**, *17*, 1193–1196.
(60) Nadarajah, A.; Wu, M. Z. B.; Archila, K.; Kast, M. G.; Smith, A. M.; Chiang, T. H.; Keszler, D. A.; Wager, J. F.; Boettcher, S. W. *Chem. Mater.* **2015**, *27*, 5587–5596.
(61) Toroker, M. C.; Carter, E. a. *J. Mater. Chem. A* **2013**, *1*, 2474–2484.
(62) Wondraczek, L.; Mauro, J. C.; Eckert, J.; Kühn, U.; Horbach, J.; Deubener, J.; Rouxel, T. *Adv. Mater.* **2011**, *23*, 4578–4586.
(63) Rawson, H. *Inorganic Glass-Forming Systems*; Academic Press Inc.: London, 1967.
(64) Ropp, R. C. *Inorganic Polymeric Glasses*; Elsevier Science Publishers B.V.: Amsterdam, 1992.
(65) Doremus, R. H. *Glass Science*, 2nd ed.; John Wiley & Sons, Inc.: New York, 1994.
(66) Chueh, C.; Li, C.-Z.; Jen, A. K.-Y. *Energy Environ. Sci.* **2015**, *8*, 1160–1189.
(67) Battaglia, C.; Martin de Nicolás, S.; Wolf, S. De; Yin, X.; Zheng, M.; Ballif, C.; Javey, A. *Appl. Phys. Lett.* **2014**, *104*, 1–5.
(68) Wurfel, U.; Cuevas, A.; Wurfel, P. *IEEE J. Photovoltaics* **2015**, *5* (1), 461–469.
(69) Zhou, N.; Kim, M.-G.; Loser, S.; Smith, J.; Yoshida, H.; Guo, X.; Song, C.; Jin, H.; Chen, Z.; Yoon, S. M.; Freeman, A. J.; Chang, R. P. H.; Facchetti, A.; Marks, T. J. *Proc. Natl. Acad. Sci.* **2015**, *112* (26), 7897–7902.
(70) Cargnello, M.; Fornasiero, P.; Gorte, R. J. *Catal. Letters* **2012**, *142* (9), 1043–1048.
(71) Strayer, M. E.; Senftle, T. P.; Winterstein, J. P.; Vargas-Barbosa, N. M.; Sharma, R.; Rioux, R. M.; Janik, M. J.; Mallouk, T. E. *J. Am. Chem. Soc.* **2015**, *137*, 16216–16224.

(72) Smith, R. D. L.; Prévot, M.; Fagan, R. D.; Zhang, Z.; Sedach, P. A.; Siu, M. K. J.; Trudel, S.; Berlinguette, C. P. *Science.* **2013**, *340*, 60–63.
(73) Greeley, J.; Stephens, I. E. L.; Bondarenko, a S.; Johansson, T. P.; Hansen, H. a; Jaramillo, T. F.; Rossmeisl, J.; Chorkendorff, I.; Nørskov, J. K. *Nat. Chem.* **2009**, *1*, 552–556.
(74) Ha, S. D.; Ramanathan, S. *J. Appl. Phys.* **2011**, *110*, 1–20.
(75) Strukov, D. B.; Snider, G. S.; Stewart, D. R.; Williams, R. S. *Nature* **2008**, *453* (May), 80–84.
(76) Richter, P.; Plassmeyer, P. N.; Harzdorf, J.; Rüffer, T.; Lang, H.; Kalbacova, J.; Jöhrmann, N.; Schulze, S.; Hietschold, M.; Arekapudi, S. S. P. K.; Albrecht, M.; Zahn, D. R. T.; Page, C. J.; Salvan, G. *Chem. Mater.* **2016**, *28* (14), 4917–4927.
(77) Prellier, W.; Fouchet, a; Mercey, B. *J. Phys. Condens. Matter* **2003**, *15*, R1583--R1601.
(78) Kobliska, R. J.; Aboaf, J. A.; Gangulee, A.; Cuomo, J. J.; Klokholm, E. *Appl. Phys. Lett.* **1978**, *33* (5), 473–475.
(79) Wang, W. Synthesis and Characterization of Aluminum Oxide Based Materials - from Molecule to Device, 2013.
(80) Wang, W.; Liu, W.; Chang, I.-Y.; Wills, L. A.; Zakharov, L. N.; Boettcher, S. W.; Cheong, P. H.-Y.; Fang, C.; Keszler, D. A. *Proc. Natl. Acad. Sci.* **2013**, *110* (46), 18397–18401.
(81) Wang, W.; Wentz, K. M.; Hayes, S. E.; Johnson, D. W.; Keszler, D. A. *Inorg. Chem.* **2011**, *50*, 4683–4685.
(82) Schweitzer, G. K.; Lester, L. P. *The Aqueous Chemistry of the Elements*; Oxford University Press: New York, 2010.
(83) Carnes, M. E.; Knutson, C. C.; Nadarajah, A.; Jackson, M. N. J.; Oliveri, A. F.; Norelli, K. M.; Crockett, B. M.; Bauers, S. R.; Moreno-luna, H. A.; Taber, B. N.; Pacheco, D. J.; Olson, J. Z.; Brevick, K. R.; Sheehan, C. E.; Johnson, D. W.; Boettcher, S. W. *J. Mater. Chem. C* **2014**, *2*, 8492–8496.
(84) Plassmeyer, P. N.; Archila, K.; Wager, J. F.; Page, C. J. *Appl. Mater. Interfaces* **2015**, *7*, 1678–1684.
(85) Nadarajah, A.; Carnes, M. E.; Kast, M. G.; Johnson, D. W.; Boettcher, S. W. *Chem. Mater.* **2013**, *25*, 4080–4087.
(86) Meyers, S. T.; Anderson, J. T.; Hong, D.; Hung, C. M.; Wager, J. F.; Keszler, D. A. *Chem. Mater.* **2007**, *19* (16), 4023–4029.
(87) Kojima, I.; Li, B. **1999**, *16* (2).
(88) Hardeveld, R. M. Van; Gunter, P. L. J.; IJzendoorn, L. J. van; Wieldraaijer, W.; Kuipers, E. W.; Niemantsverdriet, J. W. *Appl. Surf. Sci.* **1995**, *84*, 339–346.
(89) Norelli, K. M.; Plassmeyer, P. N.; Woods, K. N.; Glassy, B. A.; Knutson, C. C.; Beekman, M.; Page, C. J. *Solid State Sci.* **2016**, *55*, 8–12.
(90) Melnikov, P.; Nascimento, V. A.; Arkhangelsky, I. V; Consolo, L. Z. Z. *J. Therm. Anal. Calorim.* **2013**, *111*, 543–548.
(91) Yuvaraj, S.; Fan-Yuan, L.; Tsong-Huei, C.; Chuin-Tih, Y. *J. Phys. Chem. B* **2003**, *107*, 1044–1047.
(92) Will, G.; Masciocchi, N.; Parrish, W.; Hart, M. *J. Appl. Crystallogr.* **1987**, *20*, 394–401.
(93) Sasaki, S.; Fujino, K.; Takéuchi, Y. *Proc. Japan Acad. Ser. B Phys. Biol. Sci.*

1979, *55* (2), 43–48.
(94) Åsbrink, S.; Norrby, L.-J. *Acta Crystallogr.* **1970**, *B26*, 8–15.
(95) Bachmann, H. G.; Ahmed, F. R.; Barnes, W. H. *Zeitschrift für Krist. - Cryst. Mater.* **1961**, *115*, 110–131.
(96) Sawada, H. *Mater. Res. Bull.* **1994**, *29* (3), 239–245.
(97) Geller, S. *Acta Crystallogr. Sect. B* **1971**, *B27* (2), 821–828.
(98) Blake, R. L.; Hessevick, R. E.; Zoltai, T.; Finger, L. W. *Am. Mineral.* **1966**, *51*, 123–129.
(99) Abrahams, S. C.; Bernstein, J. L. *Acta Crystallogr.* **1969**, *B25*, 1233–1236.
(100) Eaton, P.; West, P. *Atomic Force Microscopy*; 2010.
(101) Zhang, L.; Jiang, H. C.; Liu, C.; Dong, J. W.; Chow, P. *J. Phys. D. Appl. Phys.* **2007**, *40*, 3707–3713.
(102) Alimardani, N.; Cowell, E. W. (III); Wager, J. F.; Conley, John F, J.; Evans, D. R.; Chin, M.; Kilpatrick, S. J.; Dubey, M. *J. Vac. Sci. Technol. A Vacuum, Surfaces, Film.* **2012**, *30* (1), 1–6.
(103) Kim, J.-H.; Kim, J.-Y.; Kang, S.-W. *J. Appl. Phys.* **2005**, *97*, 1–5.
(104) Nilsen, O.; Rauwel, E.; Fjellvåg, H.; Kjekshus, A. *J. Mater. Chem.* **2007**, *17*, 1466–1475.
(105) Campbell, S. A. *The Science and Engineering of Microelectronic Fabrication*; Oxford University Press: New York, 2001.
(106) Haynes, W. M. *CRC Handbook of Chemisty and Physics*, 91st ed.; Taylor & Francis Group LLC: Boca Raton, 2016.
(107) Honda, K. *Bull. Chem. Soc. Jpn.* **1964**, *37* (5), 723–730.
(108) Zachariasen, W. H. *J. Am. Chem. Soc.* **1932**, *54* (1), 3841–3851.
(109) Pauling, L. *J. Am. Chem. Soc.* **1929**, *51*, 1010–1026.
(110) Dunitz, J. D.; Orgel, L. E. *J. Phys. Chem. Solids* **1957**, *3*, 318–323.
(111) Seevers, R.; DeNuzzio, J.; Farrington, G. C.; Dunn, B. *Off. Nav. Res.* **1983**, *N00014-81-* (2), 1–19.
(112) Wuensch, B. J.; Vasilos, T. *J. Chem. Phys.* **1962**, *36* (11), 2917–2922.
(113) Rost, C. M.; Sachet, E.; Borman, T.; Moballegh, A.; Dickey, E. C.; Hou, D.; Jones, J. L.; Curtarolo, S.; Maria, J.-P. *Nat. Commun.* **2015**, *6*, 1–8.
(114) Bruce, P. G. *Solid State Electrochemistry*; University Press: Cambridge, 1995.
(115) Buchholz, D. B.; Liu, J.; Marks, T. J.; Zhang, M.; Chang, R. P. H. *ACS Appl. Mater. Interfaces* **2009**, *1* (10), 2147–2153.
(116) Lee C.-H.; Lin, T.-S.; Mou, C.-Y. *40th Anniv. Int. Zeolite Conf. 15th Int. Zeolite Conf.* **2007**, *Volume 170*, 1438–1445.
(117) Vercamer, V.; Lelong, G.; Hijiya, H.; Kondo, Y.; Galoisy, L.; Calas, G. *J. Non. Cryst. Solids* **2015**, *428*, 138–145.
(118) Makhlouf, S. a.; Bakr, Z. H.; Aly, K. I.; Moustafa, M. S. *Superlattices Microstruct.* **2013**, *64*, 107–117.
(119) Hu, S.; Xiang, C.; Haussener, S.; Berger, A. D.; Lewis, N. S. *Energy Environ. Sci.* **2013**, *6* (10), 2984.
(120) Danilovic, N.; Subbaraman, R.; Chang, K.; Chang, S. H.; Kang, Y. J.; Snyder, J.; Paulikas, A. P.; Strmcnik, D.; Kim, Y.; Myers, D.; Stamenkovic, V. R.; Markovic, N. M. *J. Phys. Chem. Lett.* **2014**, *5*, 2474–2478.
(121) McCrory, C. C. L.; Jung, S.; Peters, J. C.; Jaramillo, T. F. *J. Am. Chem. Soc.* **2013**,

135 (45), 16977–16987.
(122) Trotochaud, L.; Ranney, J. K.; Williams, K. N.; Boettcher, S. W. *J. Am. Chem. Soc.* **2012**, *134* (41), 17253–17261.
(123) Pletcher, D.; Li, X. *Int. J. Hydrogen Energy* **2011**, *36* (23), 15089–15104.
(124) Trotochaud, L.; Young, S. L.; Ranney, J. K.; Boettcher, S. W. *J. Am. Chem. Soc.* **2014**, *136* (18), 6744–6753.
(125) Jin, J.; Walczak, K.; Singh, M. R.; Karp, C.; Lewis, N. S.; Xiang, C. *Energy Environ. Sci.* **2014**, *0*, 1–10.
(126) Sun, K.; Shen, S.; Liang, Y.; Burrows, P. E.; Mao, S. S.; Wang, D. *Chem. Rev.* **2014**, *114* (17), 8662–8719.
(127) Glembocki, O. J.; Stahlbush, R. E.; Tomkiewicz, M. *J. Electrochem. Soc. Solid-State Sci. Technol.* **1985**, *132* (1), 145–151.
(128) Boettcher, S. W.; Warren, E. L.; Putnam, M. C.; Santori, E. A.; Turner-Evans, D.; Kelzenberg, M. D.; Walter, M. G.; McKone, J. R.; Brunschwig, B. S.; Atwater, H. A.; Lewis, N. S. *J. Am. Chem. Soc.* **2011**, *133* (5), 1216–1219.
(129) Kargar, A.; Sun, K.; Jing, Y.; Choi, C.; Jeong, H.; Zhou, Y.; Madsen, K.; Naughton, P.; Jin, S.; Jung, G. Y.; Wang, D. *Nano Lett.* **2013**, *13* (7), 3017–3022.
(130) Laursen, A. B.; Pedersen, T.; Malacrida, P.; Seger, B.; Hansen, O.; Vesborg, P. C. K.; Chorkendorff, I. *Phys. Chem. Chem. Phys.* **2013**, *15* (46), 20000–20004.
(131) McKone, J. R.; Warren, E. L.; Bierman, M. J.; Boettcher, S. W.; Brunschwig, B. S.; Lewis, N. S.; Gray, H. B. *Energy Environ. Sci.* **2011**, *4* (9), 3573.
(132) Reece, S. Y.; Hamel, J. a; Sung, K.; Jarvi, T. D.; Esswein, A. J.; Pijpers, J. J. H.; Nocera, D. G. *Science* **2011**, *334* (6056), 645–648.
(133) Seger, B.; Laursen, A. B.; Vesborg, P. C. K.; Pedersen, T.; Hansen, O.; Dahl, S.; Chorkendorff, I. *Angew. Chem. Int. Ed. Engl.* **2012**, *51* (36), 9128–9131.
(134) Seger, B.; Tilley, D. S.; Pedersen, T.; Vesborg, P. C. K.; Hansen, O.; Grätzel, M.; Chorkendorff, I. *RSC Adv.* **2013**, *3* (48), 25902.
(135) Seger, B.; Tilley, S. D.; Pedersen, T.; Vesborg, P. C. K.; Hansen, O.; Grätzel, M.; Chorkendorff, I. *J. Mater. Chem. A* **2013**, *1* (47), 15089.
(136) Sun, K.; Madsen, K.; Andersen, P.; Bao, W.; Sun, Z.; Wang, D. *Nanotechnology* **2012**, *23* (19), 194013.
(137) Warren, E. L.; McKone, J. R.; Atwater, H. A.; Gray, H. B.; Lewis, N. S. *Energy Environ. Sci.* **2012**, *5* (11), 9653.
(138) Noh, S. Y.; Sun, K.; Choi, C.; Niu, M.; Yang, M.; Xu, K.; Jin, S.; Wang, D. *Nano Energy* **2013**, *2*, 351–360.
(139) Nakato, Y.; Egi, Y.; Hiramoto, M.; Tsubomura, H. *J. Phys. Chem.* **1984**, *88* (19), 4218–4222.
(140) Nakato, Y.; Iwakabe, Y.; Hiramoto, M.; Tsubomura, H. *J. Electrochem. Soc. Electrochem. Sci. Technol.* **1986**, *133* (5), 900–904.
(141) Chen, Y. W.; Prange, J. D.; Dühnen, S.; Park, Y.; Gunji, M.; Chidsey, C. E. D.; McIntyre, P. C. *Nat. Mater.* **2011**, *10* (7), 539–544.
(142) Seger, B.; Pedersen, T.; Laursen, A. B.; Vesborg, P. C. K.; Hansen, O.; Chorkendorff, I. *J. Am. Chem. Soc.* **2013**, *135* (3), 1057–1064.
(143) Lin, Y.; Battaglia, C.; Boccard, M.; Hettick, M.; Yu, Z.; Ballif, C.; Ager, J. W.; Javey, A. *Nano Lett.* **2013**.
(144) Cox, C. R.; Winkler, M. T.; Pijpers, J. J. H.; Buonassisi, T.; Nocera, D. G. *Energy*

Environ. Sci. **2013**, *6* (2), 532.
(145) Esposito, D. V; Levin, I.; Moffat, T. P.; Talin, A. A. *Nat. Mater.* **2013**, *12* (6), 562–568.
(146) Strandwitz, N. C.; Comstock, D. J.; Grimm, R. L.; Nichols-Nielander, A. C.; Elam, J.; Lewis, N. S. *J. Phys. Chem. C* **2013**, *117* (10), 4931–4936.
(147) Kenney, M. J.; Gong, M.; Li, Y.; Wu, J. Z.; Feng, J.; Lanza, M.; Dai, H. *Science* **2013**, *342* (6160), 836–840.
(148) Yang, J.; Walczak, K.; Anzenberg, E.; Toma, F. M.; Yuan, G.; Beeman, J.; Schwartzberg, A.; Lin, Y.; Hettick, M.; Javey, A.; Ager, J. W.; Yano, J.; Frei, H.; Sharp, I. D. *J. Am. Chem. Soc.* **2014**, *136* (17), 6191–6194.
(149) Mei, B.; Seger, B.; Pedersen, T.; Malizia, M.; Hansen, O.; Chorkendorff, I.; Vesborg, P. C. K. *J. Phys. Chem. Lett.* **2014**, *5*, 1948–1952.
(150) Hu, S.; Shaner, M. R.; Beardslee, J. a.; Lichterman, M.; Brunschwig, B. S.; Lewis, N. S. *Science (80-.).* **2014**, *344*, 1005–1009.
(151) Strmcnik, D.; Uchimura, M.; Wang, C.; Subbaraman, R.; Danilovic, N.; Vliet, D. Van Der; Paulikas, A. P.; Stamenkovic, V. R.; Markovic, N. M. *Nat. Chem.* **2013**, *5* (April), 300–306.
(152) Adnane, M.; Cachet, H.; Folcher, G.; Hamzaoui, S. *Thin Solid Films* **2005**, *492* (1–2), 240–247.
(153) Oja, I.; Mere, a.; Krunks, M.; Solterbeck, C.-H.; Es-Souni, M. *Solid State Phenom.* **2004**, *99–100*, 259–264.
(154) Leskelä, M.; Ritala, M. *Angew. Chem. Int. Ed. Engl.* **2003**, *42* (45), 5548–5554.
(155) Nadarajah, A.; Carnes, M. E.; Kast, M. G.; Johnson, D. W.; Boettcher, S. W. *Chem. Mater.* **2013**, *25* (20), 4080–4087.
(156) Trotochaud, L.; Mills, T. J.; Boettcher, S. W. *J. Phys. Chem. Lett.* **2013**, *4* (6), 931–935.
(157) Subbaraman, R.; Tripkovic, D.; Strmcnik, D.; Chang, K.-C.; Uchimura, M.; Paulikas, A. P.; Stamenkovic, V.; Markovic, N. M. *Science* **2011**, *334* (6060), 1256–1260.
(158) Danilovic, N.; Subbaraman, R.; Strmcnik, D.; Chang, K.-C.; Paulikas, a P.; Stamenkovic, V. R.; Markovic, N. M. *Angew. Chem. Int. Ed. Engl.* **2012**, *51* (50), 12495–12498.
(159) Burke, L. D.; Naser, N. S.; Ahern, B. M. *J. Solid State Electrochem.* **2007**, *11*, 655–666.
(160) Döscher, H.; Geisz, J. F.; Deutsch, T. G.; Turner, J. A. *Energy Environ. Sci.* **2014**, *7* (9), 2951.
(161) Subbaraman, R.; Danilovic, N.; Lopes, P. P.; Tripkovic, D.; Strmcnik, D.; Stamenkovic, V. R.; Markovic, N. M. *J. Phys. Chem. C* **2012**, *116* (42), 22231–22237.
(162) Foong, T. R. B.; Shen, Y.; Hu, X.; Sellinger, A. *Adv. Funct. Mater.* **2010**, *20* (9), 1390–1396.
(163) Filonenko, V. P.; Sundberg, M.; Werner, P.-E.; Zibrov, I. P. *Acta Crystallogr. Sect. B Struct. Sci.* **2004**, No. 4, 375–381.
(164) Dabrowska, G.; Tabero, P.; Kurzawa, M. *J. Phase Equilibria Diffus.* **2009**, *30* (3), 220–229.
(165) Mori, M.; Isobe, T.; Senna, M. *Solid State Ionics* **1995**, *81*, 157–163.

(166) Biesinger, M. C.; Brown, C.; Mycroft, J. R.; Davidson, R. D.; Mcintyre, N. S. *Surf. Interface Anal.* **2004**, *36*, 1550–1563.
(167) Aronniemi, M.; Sainio, J.; Lahtinen, J. *Surf. Sci.* **2005**, *578*, 108–123.
(168) Sainio, J.; Aronniemi, M.; Pakarinen, O.; Kauraala, K.; Airaksinen, S.; Krause, O.; Lahtinen, J. *Appl. Surf. Sci.* **2005**, *252*, 1076–1083.
(169) http://www.pvlighthouse.com.au/calculators/OPAL 2/OPAL 2.aspx.
(170) Green, M. A. *Sol. Energy Mater. Sol. Cells* **2008**, *92* (11), 1305–1310.
(171) Irvine, W. M.; Pollack, J. B. *Icarus* **1968**, *8*, 324–360.
(172) Richards, B. S. *Sol. Energy Mater. Sol. Cells* **2003**, *79*, 369–390.